Department of Mechanical Engineering

An Investigation of Flow Structure Interactions on a Finite Compliant Surface Using Computational Methods

Mark William Pitman

This thesis is presented for the Degree of
Doctor of Philosophy
of
Curtin University of Technology

March 2007

DECLARATION

To the best of my knowledge and belief this thesis contains no material previously published by any other person except where due acknowledgement has been made.

This thesis contains no material which has been accepted for the award of any other degree or diploma in any university.

All investigations presented in this thesis are my own except where specific reference has been made to the work of others. Some of the work presented in this thesis has been published in the following:

Pitman, M.W., Lucey, A.D. and Carpenter, P.W. 2004. Computational modelling of the interaction of a flexible wall with boundary-layer flow. In: *Proc. 8th International Conference on Flow-induced Vibration*, 6th-9th July 2004 (Eds. E. De Langre & F. Axisa), Vol I, pp. 101-106

Pitman, M.W. and Lucey, A.D. 2004. A deterministic viscous vortex method for grid-free CFD with moving boundary conditions. In: *Proc. (CD) WSEAS/ IASME International Conference on Fluid Mechanics*, 17th-19th August 2004, (Eds. M. Poulos, N. Mastorakis, V. Mladenov & R. Gorla), ISBN 968-8457-01-7 (6 pages)

Pitman, M.W. and Lucey, A.D. 2004. A deterministic viscous vortex method for grid-free CFD with moving boundary conditions. *IASME Transactions* **1(4)**, pp. 591-596.

Pitman, M.W. and Lucey, A.D. 2006. A deterministic viscous vortex method with moving boundary conditions for fluid-structure interaction. In: *Proc. International Conference on Computational Methods (ICCM)*, 15th-19th December 2004, CD-ROM (4 pages)

Lucey, A.D. and Pitman, M.W. 2006. A New Method for Determining the Eigenmodes of Finite Flow-Structure Systems. Paper No. PVP2006-ICPVT11-93938, In: *Proceedings of ASME-PVP 2006: 2006 ASME Pressure Vessels and Piping Division Conference*, July 23-27, 2006, CD-ROM (10 pages)

Pitman M.W. and Lucey, A.D. 2006. Optimal Swimming Modes of a Homo-Sapien Performing Butterfly-Stroke Kicks. Paper No. PVP2006-ICPVT11-93939, In: *Proceedings of ASME-PVP 2006: 2006 ASME Pressure Vessels and Piping Division Conference*, July 23-27, 2006, CD-ROM (10 pages)

Signature: ______________________

Date: ______________________

“O sábio ouviu atentamente o motivo da visita do rapaz, mas disse-lhe que naquele momento não tinha tempo de explicar-lhe o Segredo da Felicidade. Segeriu que o rapaz desse um passeio por seu palácio, e voltasse dali a duas horas.

“-Entretanto, quero lhe pedir um favor - completou o sábio, entregando ao rapaz uma colher de chá, onde pingou duas gotas de óleo. -Enquanto você estiver caminhando, carregue esta colher sem deixar que o óleo seja derramado.

“O rapaz começou a subir e descer as escadarias do palácio, mantendo sempre os olhos fixos na colher. Ao final de duas horas, retornou á presença do sábio.

“-Então - perguntou a sábio - você viu as tapeçarias da Pérsia que estão na minha sala de jantar? Viu o jardim que o Mestre dos Jardineiros demorou dez anos para criar? Reparou nos belos pergaminhos de minha biblioteca?

“O rapaz, envergonhado, confessou que não havia visto nada. Sua nica preocupação era não derramar as gotas de óleo que o sábio lhe havia confiado.

“-Pois então volte e conheça as maravilhas do meu mundo - disse o sábio. - Você não pode confiar num homem se não conhece sua casa.

“Já mais tranqilo, o rapaz pegou a colher e voltou a passear pelo palácio, desta vez reparando em todas as obras de arte que pendiam do teto e das paredes. Viu os jardins, as montanhas ao redor, a delicadeza das flores, o requinte com que cada obra de arte estava colocada em seu lugar. De volta á presença do sábio, relatou pormenorizadamente tudo que havia visto.

“-Mas onde estão as duas gotas de óleo que lhe confiei? - perguntou o sábio

“Olhando para a colher, o rapaz percebeu que as havia derramado.

“-Pois este é o único conselho que tenho para lha dar - disse o mais sábio dos sábios. O Segredo da Felicidade está em olhar todas as maravilhas do mundo, e nunca se esquecer das duas gotas de óleo na colher.”

The wise man listened attentively to the boy’s explanation of why he had come, but told him that he didn’t have time just then to explain the secret of happiness. He suggested that the boy look around the palace and return in two hours.

“Meanwhile, I want to ask you to do something,” said the wise man, handing the boy a teaspoon that held two drops of oil. “As you wander around, carry this spoon with you without allowing the oil to spill.”

The boy began climbing and descending the many stairways of the palace, keeping his eyes fixed on the spoon. After two hours, he returned to the room where the wise man was.

“Well,” asked the wise man, “did you see the Persian tapestries that are hanging in my dining hall? Did you see the garden that it took the master gardener ten years to create? Did you notice the beautiful parchments in my library?”

The boy was embarrassed, and confessed that he had observed nothing. His only concern had been not to spill the oil that the wise man had entrusted to him.

“Then go back and observe the marvels of my world,” said the wise man. “You cannot trust a man if you don’t know his house.”

Relieved, the boy picked up the spoon and returned to his exploration of the palace, this time observing all of the works of art on the ceilings and the walls. He saw the gardens, the mountains all around him, the beauty of the flowers, and the taste with which everything had been selected. Upon returning to the wise man, he related in detail everything he had seen.

“But where are the drops of oil I entrusted to you?” asked the wise man. Looking down at the spoon he held, the boy saw that the oil was gone.

“Well, there is only one piece of advice I can give you,” said the wisest of wise men. “The secret of happiness is to see all the marvels of the world, and never to forget the drops of oil on the spoon.”

O alquimista (The Alchemist) - Paulo Coelho

ACKNOWLEDGEMENTS

Of the many people that I have to thank, here are just a few:

Prof AD Lucey from Curtin University of Technology, for providing assistance and guidance on all aspects of my PhD as well as in my personal life.

Prof PW Carpenter from the University of Warwick, for providing great assistance in the preparation of academic papers throughout my PhD as well as some great discussions.

Dr. Andrew King and Dr. Richard Howell, for being excellent colleagues to share ideas with, help me with guidance throughout my time as a post-grad and being there to share a few beers with.

Professor Ramon Frederick and the Universidad National de Chile for accommodating me throughout my four month stay in Santiago.

The Fluid Dynamics Research Group at Warwick University, for accommodating me throughout the two month period of my PhD and making me feel very comfortable in my temporary position there.

Final year project students Alistair D Nixon and Ali A Al-Buenain for assisting me in compiling some of the results for this thesis.

Margaret Brown and the staff at the Department of Mechanical Engineering for tolerating my poor ability to perform routine administrative paperwork, and correcting my mistakes.

Finally, I would like to acknowledge my family. Many things happened throughout my time as a post-grad student. I travelled. I bought my first house. I made and lost money. I felt the extremes of love and pain in equal measure. Your guidance and support made all these great things possible... and bearable.

NOMENCLATURE

Some of the common variables that are utilised throughout this thesis are presented below. The variables presented below take these meanings unless otherwise stated in the text.

Wall-based variables:

K	Backing-spring stiffness (N/m^2)
ν	Poisson ratio
L	Length of compliant section (m)
h	Thickness of wall material (m)
E	Youngs Modulus N/m^2
B	Flexural rigidity (eqn. 3.2 on page 29)

Flow-based variables:

Φ	Velocity potential function
U_∞	Mean-stream velocity (m/s)
ρ	Fluid density (kg/m^3)
μ	Fluid viscosity ($N.s/m^2$)

Computational variables:

σ	Vortex element core size (m)

Plotting:

In a plot of wall positions (such as Figure 4.2) the bold line represents the *final* position of the wall. The wall positions are plotted at equal time intervals over a time equal to half of one time period of oscillation.

Abstract

A study of the interaction of one-sided flow over a compliant surface is presented. When fluid passes over a flexible surface the simultaneous interaction between the flow and structure gives rise to vibrations and instabilities on the surface as well as in the fluid. The fluid-structure interaction (FSI) has potential to be used in the control of boundary layer dynamics to achieve drag reduction through transition delay. The modelling and control of FSI systems apply to many fields of engineering beyond drag reduction, for example: the modelling and analysis of biomechanical systems; natural environmental systems; aero-elastics; and other areas where flow interacts moving or compliant boundaries.

The investigation is performed through numerical simulation. This returns more detail than could be resolved through experiments, while also permitting the study of finite compliant surfaces that are prohibitively difficult, or impossible, to study with analytical techniques. In the present work, novel numerical modelling methods are developed from linear system analysis through to non-linear disturbances and viscous effects. Two numerical modelling techniques are adopted to approach the analysis of the FSI system. A potential-flow method is used for the modelling of flows in the limit of infinite Reynolds numbers, while a grid-free Discrete Vortex Method (DVM) is used for the modelling of the rotational boundary-layer flow at moderate Reynolds numbers.

In both inviscid and viscous studies, significant contributions are made to the numerical modelling techniques. The application of these methods to the study of flow over compliant panels gives new insight to the nature of the FSI system. In the linear inviscid model, a novel hybrid computational/theoretical method is developed that evaluates the eigenvalues and eigenmodes from a discretised FSI system. The results from the non-linear inviscid model revealed that the steady-state of the non-linear wall motion is independent of initial excitation. For the viscous case, the first application of a DVM to model the interaction of a viscous, rotational flow with a compliant surface is developed. This DVM is successfully applied to model boundary-layer flow over a finite compliant surface.

Contents

List of Figures

Part I

Introduction and Literature Review

Chapter 1

Introduction

Fluid-structure interaction is observed in the day to day lives of everyone. The world abounds with interactions between the two gaseous and liquid phases and the third solid phase. From the shimmering of leaves on a tree due to the wind, to the propulsion of sea-creatures, to the very life-supporting cardio-vascular system of all mammals, the dynamics of fluid-structure interaction play a critical role. Notwithstanding the widespread occurrence and importance of these dynamics, there remains much to be understood about the underlying dynamics of such systems.

Understanding the fluid dynamics of systems has allowed the development of new technology. Researchers as early as Leonardo Da Vinci[1] in 1508 noted the development of vortical structures in the human circulatory system. These vortical structures play an important role in the mechanics of the opening and closing of arterial valves. The culmination of that pioneering research, and much later work, has played a major role in the development of common, famous, and sometimes life-saving, technology such as the artificial heart-pump. Likewise, research in the dynamics of solid structures has existed for as long as humans have been able to build such structures. Knowledge of such dynamics has played a major role in the prediction of potentially life-threatening failure, and the development of new technology that utilises these dynamical traits. However, it is only rela-

---

[1] See the review given by Gharib et al. [34]

tively recently that researchers have begun to investigate the interaction of the coupled fluid and structure dynamics, in doing so uncovering some previously unrecognised potential in the underlying dynamics of the fluid-structure system.

The work presented in this thesis is a small step in what is part of a larger movement towards understanding the secrets of fluid-structure interaction.

1.1 Research Background

Fluid-structure interaction (FSI) is a broad field of study. The research described in this thesis focuses specifically on the interaction of one-sided boundary-layer flow over a spring-damper backed compliant wall section shown in Figure 1.1. In this system, the flow of fluid over the compliant wall section forces the motion of the wall. The motion of the wall will *simultaneously* adjust the boundary conditions for the fluid flow. The corresponding exchange of energy between the wall and fluid gives rise to many interesting flow phenomena and instabilities.

Interest in the study of this fluid-structure system first arose when it was noted that dolphins could achieve anomalously high swimming speeds given their body mass. Simple hydrodynamic analysis of dolphins in the 1920's by Gray [35] found that dolphins would need have to have a strength-to-weight ratio of up to ten times any other mammal in order to achieve such high swimming speeds. This became known as Gray's paradox. Although later, more detailed, hydrodynamic studies found that this factor could be partly attributed to common factors, the original paradox remained. It was believed that the secret lay in the skin of the dolphin and its ability to reduce drag by maintaining a laminar boundary layer, which induces much less drag than turbulent boundary layers. Later theoretical studies have found strong evidence that indefinite postponement of laminar-turbulent transition is indeed possible through the application of compliant dolphin-skin-like materials at the surface. Reviews of these studies are found in Carpenter et al. [16]. However, debate still continues as to whether the high swimming speeds of dolphins are a result of other factors than the skin, as discussed by Fish and Clifford [27].

Early experimental investigations into this FSI yielded promising albeit erratic results. The complex nature of the interaction as well as the length and time scales on which the instabilities occur mean that experimental studies can be very difficult to set-up and obtain accurate and informative results. Theoretical studies became favoured in the study of these dynamical systems for this reason. Early theoretical studies used simplified fluid-models coupled with presupposed wall motion, usually within an infinite two-dimensional domain. Later studies involved more complex theoretical analysis, however all involved critical assumptions of linearity or presupposed modal features that could have masked some of the critical dynamics of the system.

With the advent of modern high-powered computing equipment, numerical experiments were able to be conceived that did not rely upon any *ad-hoc* assumptions of wall nor fluid dynamics. Utilising a variety of techniques numerical simulations have been used to delve further into the dynamics of the ‘real’ system.

1.1.1 Drag-Reduction Methods

Compliant coatings of the type discussed in Section 1.1 do not represent the only method of reducing drag. The field of drag-reduction is vast and is based on three major methods of boundary-layer manipulation, these being: active, passive and static.

The compliant wall shown in Figure 1.1, and studied herein, falls within the category of passive boundary layer manipulation. In this system, no mechanical nor electrical system is implemented to facilitate energy transfer to/from the system. The energy transfer (that ultimately manipulates/controls the boundary layer) is effected by the natural dynamics of the fluid-structure interaction between the solid boundary and the fluid. Correct design of the compliant panel could give an ideal energy transfer that enables the boundary layer to remain laminar indefinitely. The advantages of this method is that it is very simple to implement and requires little maintenance. A problem is that the dynamics of the fluid-structure interaction must be well understood before accurate and robust design methodologies can be developed.

Active manipulation involves using sensors to measure perturbations within the boundary layer and actuators (eg. a zero-net-flux wall jet) to positively influence the boundary layer to achieve a drag reduction. The control systems used and the implementation of these systems are required to be small-scale, compact and low-latency. With the recent and ongoing advancements in Micro-Electro-Mechanical Systems (MEMS) this method of drag reduction is becoming a feasible option for reducing drag. The advantage of this method is that it allows a much more robust control of the fluid dynamics, as the control system can be 'programmed' towards a larger variety of arbitrary objectives than passive or static control. However, these systems will always remain technologically more complicated and expensive to implement than passive or static systems.

Static manipulation involves using carefully designed surface contours or bumps to influence the dynamics of the near-wall boundary layer dynamics. This method is very simple and easy to implement, however it lacks in the ability to effect energy transfer to/from the fluid. Without an energy transfer mechanism then postponement of the boundary layer from laminar to turbulent is inevitable. Therefore, this system is limited in that it only reduces the drag intensity of an already turbulent boundary layer.

As a corollary to this, it is important to note that drag reduction does not always imply laminar-turbulent transition delay. It is possible that passive as well as active means of control can be used to mediate the intensity of near wall turbulence induced drag. Indeed a great deal of work with active control focuses specifically on this objective (see Tsao et al. [79]), although the majority of research with compliant coatings focuses on transition delay.

1.2 Overview of Research

The work in this thesis focuses on the passive control mechanisms of the compliant wall shown in Figure 1.1. The investigation looks at instabilities and flow-phenomena that occur around transitional Reynolds numbers with the objective of investigating transition delay.

The investigation of FSI system instabilities can further be reduced to the classification groups of wall-based instabilities and fluid-based instabilities. This research therefore approaches the investigation of instabilities from two directions, with the objective of unifying the various methods of investigation. The two major parts of this research are therefore: the study of wall-based instabilities by inviscid (potential) flow modelling and; the study of the complete system (wall and flow based instabilities) using near-DNS type techniques.

In order to effect these investigations a combination of new as well as 'tried-and-tested' techniques will be adopted. Therefore, a separate objective, further to the investigation of physical instabilities, will be the invention of new computational techniques for studying FSI.

The overview of research presented here is as follows:

Research Problem - the two approaches to the investigation are each assigned problem statements within a defined research problem.

Methodology - a brief overview of the methods that are used to approach the research problems are defined.

Scope and Assumptions - the limitations and boundaries of the current work are defined and discussed.

Summary of Contributions - the outcomes and their contributions to the field of Fluid-Structure Interaction Theory are discussed.

1.2.1 Research Problem

The research problem can be stated as:

> "To perform a thorough investigation of hydro-elastic instabilities of finite compliant panels through the application of linear and non-linear models and the drag reduction potential of finite compliant panels through near Direct Numerical Simulation (DNS) techniques."

The research problem involves using various computational techniques in order to obtain a holistic view of compliant panels and their potential for drag-reduction. Previously researchers have focused attention on specific parts of the whole system such as linear stability, spatial disturbance evolution or non-linear wall transience. In this research the focus will be on the development and application of two numerical methods to approach and unify the problem. The two models are used because they each answer two critical subsets of the research question.

Problem Statement One: How does the flow-structure system evolve from a transient response to reach a steady-state response? Particularly with the consideration of non-linear effects, what is the steady-characteristics of the fluid-structure system and how do finite-panel edge effects play a role in the response?

Problem Statement Two: By adopting a near-DNS approach to simulating the full spatial and temporal evolution of disturbances to a compliant wall section subject to boundary-layer flow, is it possible to directly measure a drag reduction under certain conditions? What is the characteristic of the drag reduction mechanism? Can critical aspects be isolated for design of practical coatings?

1.2.2 Methodology

In order to tackle fully two main problem statements of the research two different computational methods will be developed, validated and applied. The results from each will be used to examine the various features of the full flow-structure system at various states of development.

Problem Statement One: The non-linear potential-flow solver coupled with a finite-difference structural algorithm, originally developed by Lucey et al. [56], will be redeveloped under MATLAB with some improvements made to the method. Improved computational power of the present day allows a more thorough investigation of non-linear wall dynamics at long time development. Particularly, investigations of non-linear steady-state responses of the system, something not thoroughly investigated before, will be examined. Of particular interest is the influence of finite-length panel-edges on the steady-state response of both the wall and fluid based instabilities.

Problem Statement Two: A near-DNS Discrete Vortex Method (DVM) coupled to the same finite difference wall algorithm will be used to investigate the full spatio-temporal evolution of fluid disturbances and the influence of compliant panels on these disturbances. Particularly, being able to directly measure a drag reduction from the simulation will allow the direct observation of drag-reduction mechanisms.

By approaching the two subsets of the overall research problem with these methodologies a more thorough understanding of the full hydro-elastic dynamics throughout transience as well as steady-state and its application to drag reduction will be achieved.

1.2.3 Scope and Assumptions

The work presented in this thesis will use a variety of computational as well as theoretical techniques to analyse various aspects of the flow-structure system that is the focus of this research. Each of these various techniques present pieces of a larger puzzle that can be pieced together.

All of the flow systems analysed in this thesis are assumed two-dimensional. However the majority of the flow systems studied will be at Reynolds numbers below which three dimensional effects become significant. Also as demonstrated in Gad-el Hak [29] and can be seen in Figure 1.2, the hydroelastic instabilities tend to be largely two-dimensional in nature even up to the non-linear regime. This is particularly important for the development of the DVM boundary layer model where the model will be used only within regions where two-dimensional

Tollmien-Schlichting instabilities occur in the flow domain. It is important to note that easy extension of the presented methods to three dimensionality was a consideration in the selection of such methods. For the ideal-flow model presented in Part 2 there have already been three-dimensional investigations though various work of Lucey et al. [56]. However, the work presented here continues to focus on two-dimensional modelling and aims to perform a more thorough investigation of divergence and post-divergence hydroelastic instability.

The absence of the boundary layer in the ideal-flow model means that various instabilities may not be captured in the analysis. However, this assumption is mitigated by the consideration that many of the instability studies with the ideal-flow model will consist of wall curvatures that are large with respect to the mean flow speed and boundary layer thickness. The potential flows also give an 'infinite Reynolds number' approximation of the flow, therefore the results obtained by the potential flow model remain valid for some real flow situations.

1.2.4 Summary of Contributions

The development of new simulation capabilities will result in new analysis tools. These new tools will find application in many areas of fluid-structure interaction such as modelling and analysis of biomechanical systems. However, in the proposed research, application will be restricted to the analysis of plane single-sided flow over a compliant surface. Greater understanding and modelling ability of the mechanics of flow-structure interaction is crucial in many applications. The new computational methods have potential for application either directly to the modelling and prediction of fluid-structure interaction systems or the generic analysis of fluid-structure interaction.

In the present consideration of a one-sided flow over a compliant surface, the application of these new tools will be used to derive a greater understanding of the FSI mechanisms. Particularly, the nature of linear disturbance growth, the transition from linear disturbances through to a non-linear regime, and the influence of a rotational boundary layer on these results. These results have application directly to the design of practical compliant panels for drag-reduction, and also more general application to the field of hydrodynamic stability.

Despite the work highlighted in the background section above, there still remain many unresolved issues concerning the effect of wall compliance on turbulent flows. Notwithstanding the wealth of experimental information, a firm theoretical basis for the understanding of hydrodynamic and hydroelastic stability is lacking. Many apparent paradoxes still remain, due largely to the analysis techniques that have been adopted thus far. Inadequate computational models that simplify the domain have restricted previous work. However, with the development of pioneering computational analysis tools throughout the course of the proposed research, a further step is taken to understanding the theory behind the complexities of FS interaction.

As the ability to model and analyse more complex systems develops, the application of this technology moves further outside the realm of classical applications to drag reduction and collapsible tube analysis. The borderlines between analysis of the various fluid-structure interaction fields such as collapsible tubes and compliant walls are becoming intertwined. Current work has moved away from focusing merely upon these areas and extended towards the modelling of natural system for biomedical and environmental purposes. The benefits of greater understanding of compliant wall interaction are being identified in many other areas, some far outside the realm of classical fluid mechanics application.

1.3 Layout of thesis

This thesis consists four parts containing seven chapters. Part 1 and Part 4 correspond to the introduction/background and conclusion parts of the thesis respectively. While the Parts 2 and 3 that make up the body of the thesis detail the investigations using potential flow and DVM methods respectively.

The outline of the thesis, with relevant parts and chapters, is presented below with a brief description of each:

Part One - Introduction and Literature Review gives a broad introduction to the research field as well as a specific review of relevant work performed.

Chapter 1 gives a broad overview and background to the research problem, contribution, approach and layout of the investigation in this thesis.

Chapter 2 reviews the more specific literature and work done in the field of this research problem. This literature review is designed to complement other detailed reviews of fluid-structure research. The review is subdivided into subject areas and developments are presented in a roughly chronological order.

Part Two - The ideal-flow model describes the model and methods used to analyse Problem Statement One as well as results obtained. This problem statement deals with wall-based instabilities, particularly the divergence instability.

Chapter 3 Gives a description of the potential-flow model used and the governing equations as well as some techniques used to further breakdown and analyse the system. Some improvements are made to existing techniques and some new techniques are developed for studying the steady-state behaviour of the system.

Chapter 4 Contains the results achieved through the application of the methods developed in Chapter Three. Results are further subdivided into results from linear analysis, investigation of transience mechanisms, and the investigation of steady-state responses for non-linear deformations of a compliant wall.

Part Three - DVM Boundary Layer model describes the computational model used to perform DNS-like simulations of a boundary layer interacting with a compliant surface.

Chapter 5 Describes the development of the Lagrangian vortex model and its full coupling with the flow system. Some results are given to validate the flow model at various points of its development.

Chapter 6 Results achieved through the application of the methods developed in chapter five. Due to the complexity of the DVM model, the investigations at this point are limited to transience. Information is extracted from transient results that indicate the drag-reduction correlations.

Part Four - Conclusions unifies the knowledge obtained from parts two and three and draws conclusions as to the development of fluid-structure systems.

Chapter 7 Conclusions are drawn from the investigations performed through the literature review, potential flow model and the near-DNS results and the potential for further work is discussed.

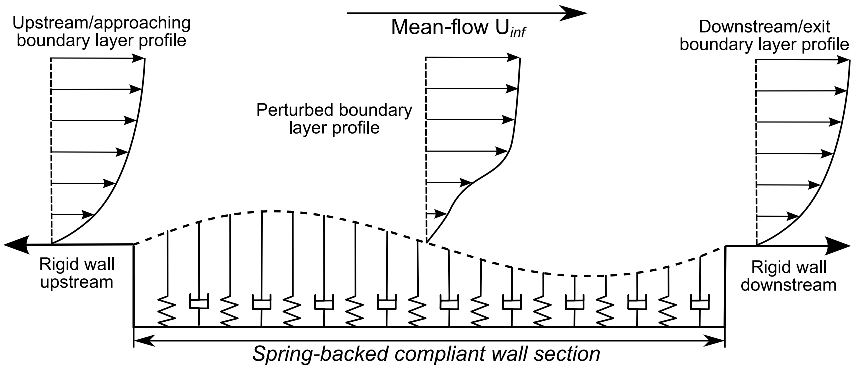

Figure 1.1: One-sided boundary layer flow over a finite compliant wall set in an otherwise rigid domain

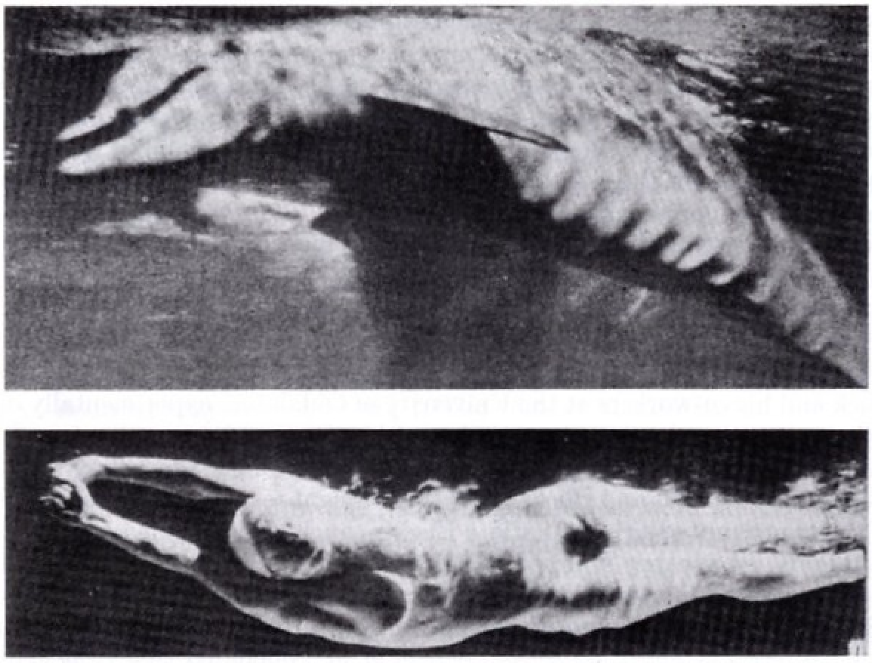

Figure 1.2: Photographs displaying wavelike folds and local buckling in compliant skin appearing during rapid swimming of a *delphinidae* (top photograph) and a *Homo sapiens* (bottom photograph). From Aleyev [4]

Chapter 2

Literature Review

2.1 Introduction

Presented in this section is a review of past studies of compliant coatings, a form of passive boundary layer control. The review focuses on compliant coatings for drag reduction by laminar-turbulent transition postponement involving studies of two-dimensional mechanisms as this is the primary focus of this thesis. However attention is also paid to work in non-linear and three-dimensional studies and studies of turbulent boundary layer drag reduction, as this is also important for understanding the mechanisms of fluid-structure energy transfer.

2.2 Compliant Coatings

There has been a great deal of attention paid to the study of compliant coatings for drag reduction. The range of techniques used to investigate this system are equally vast. Studies range from experimental to theoretical, linear to non-linear, numerical to analytical and ideal-flow to rotational (boundary layer) flow investigations. Many of these studies were taking place concurrently and, like the pieces of a jigsaw, yielding various insights into the overall system.

Chronologically, it can be stated that early investigations were based on experimental and two-dimensional theoretical analysis. It is only more recently

(1990 onwards) that numerical models, originally based on two-dimensional, linear and ideal-flow assumptions, have been used considerably for analysis of this system. Presently, with the availability of modern computing equipment, non-linear and three-dimensional studies have been performed using Direct Numerical Simulation (DNS) techniques.

This study focuses primarily on two-dimensional, linear mechanisms. Therefore, the review focuses on the experimental and theoretical work of two-dimensional studies. The review follows a roughly chronological order, leading up to a brief review of more recent non-linear and three-dimensional studies.

Thorough reviews of the use of compliant walls for drag-reduction and flow control are given by Carpenter [13], [14] and Gad-el Hak [30], [31], [32]. To avoid repetition, the review presented in this thesis is aimed at complementing these reviews with a focus on the objectives of this thesis and recent advances.

Generally speaking, the first studies in fluid-structure interaction were based on experimental investigations. A review of experimental work is presented by Gad-el Hak [29] and Klinge et al. [44]. Since the 1980's, with the pioneering theoretical work of Carpenter and Garrad [17], [18], interest in transition delay by theoretical studies was re-ignited. Since the 1990's, with the numerical work of Lucey and Carpenter [55], and the advent of modern computing equipment, contemporary studies in fluid-structure interaction have centred mostly on numerical studies.

Interest first arose in the study of compliant coatings for drag reduction when, in 1936, Gray [35] performed a rudimentary analysis of the physiological power of a dolphin and the required power to swim at observed speeds. He concluded that the power of a dolphin was insufficient to achieve the speeds that had been observed by mariners. This became known as Gray's paradox and it was hypothesised that dolphins (and other marine creatures) have some drag-reducing properties in their skin.

These observations led to the first modern experimental study of compliant coatings was by Kramer [45], who based his compliant coating on the structure of dolphin epidermis, as seen in Figure 2.1. These early experiments involved the measurement of drag coefficients of bodies of revolution towed through seawater (Long Beach Harbour, California) with varying properties of compliant coatings. Under certain conditions, drag reductions of up to 60% were a achieved, which led to the claim that the compliant coatings were delaying the laminar-turbulent transition of the boundary layer[1]. However, these studies returned little information of surface deformation and boundary-layer disturbance and the results achieved erratic instances of drag reduction. None the less, this pioneering work provided a major stimulus for interest towards further understanding the mechanisms of flow over a compliant coating.

The first experimental observations of surface deformation in fluid-structure interaction are attributable to Puryear [68]. Further experimental work throughout the 60's and 70's by Benjamin [11], Ritter and Porteous [69], Smith and Blick [75] and Landahl [47] attempted to reproduce the work of Kramer. A lack of understanding of the role of compliant surfaces in the context of transition delay was a major cause of the experiments often being poorly set-up. This resulted in transition being encountered much sooner than the rigid wall case. However, great progress was made, particularly by Benjamin [11] and Dugundji et al. [25], in the identification and classification of hydroelastic instabilities through theoretical work. Theoretical analysis by Landahl [47] confirmed the existence of a rich variety of instabilities present in the fluid-structure system. None the less, given the unfavourable results in transition delay, attention was turned to the use of compliant walls for drag reduction in turbulent boundary layers as opposed to postponing transition to a turbulent boundary layer. The experiments by Fisher et al. [28] and Smith and Blick [75] demonstrate this.

As stated in Gad-el Hak [30], three major classification schemes have been popularly adopted for the fluid-structure waves. The first classification scheme was developed by Benjamin [11]. He developed three classes of waves for the fluid-

---

[1] Drag reduction can be achieved by reducing the intensity of turbulent boundary layers or delaying the transition of a boundary layer from laminar to turbulent, as discussed in Section 1.1.1

structure system, labelled class A, B and C waves. Class A and B waves refer to fluid and solid based oscillations respectively that involve conservative energy transfer between the fluid and wall, but their stability is affected by irreversible processes such as dissipation. Class C waves refer to instabilities created by conservative hydrodynamic forces causing a uni-directional energy transfer to the solid. The second classification scheme is by Carpenter and Garrad [17], [18]. This scheme divides the waves into fluid-based and solid-based instabilities. In the early stages of transition, the primary fluid-based oscillations are the Tollmien-Schlichting instabilities (TSI). The solid-based oscillations are referred to as flow-induced surface instabilities (FISI). The third classification system is by Huerre and Monkewitz [39] and divides waves into absolute and convective instabilities.

Interest in the use of compliant coatings for transition delay arose again through the careful theoretical investigation of instabilities present in flow over a Kramer-type compliant surface by Carpenter and Garrad [17], [18]. This work showed, for the first time, that Kramer's coatings were capable of transition delay. It confirmed that the flexibility of the wall increases Tollmien-Schlichting (TS) wave stabilisation, which are the waves responsible for the transition of the boundary layer to turbulence. However, it also identified that wall damping tended to destabilise the TS wave while improving the suppression of hydroelastic instabilities. The design of a compliant wall then became one of a balance between wall flexibility to prevent transition and added wall damping to maintain hydroelastic stability.

With the knowledge gained from studies into fluid-structure interaction, much of the work throughout the 90's focused on the optimisation of compliant walls for drag reduction. The experimental and numerical works of Babenko [6], Carpenter and Davies [15], Colley et al. [23] highlight this. However, theoretical and numerical studies continued to investigate the mechanisms by which drag reduction was achieved, and debate still continued as to whether drag reduction could be achieved in any practical environment outside of theory or controlled experimental situations.

The numerical investigations during the late 1990's and into the present decade made use of the improved computing technology. Developments were also made during this time in computing algorithms, which allowed researchers to study a wider variety of systems. Wang et al. [81], Wiplier and Ehrenstein [84, 85], Visbal and Gordnier [80] and Aleksyev [3] give examples where complex DNS requiring intense computing power is used to simulate the development of boundary layer flow over a compliant surface.

The work of Marquillie and Ehrenstein [58] and Ehrenstein and Gallaire [26] use a combination of modern computing algorithms coupled with a theoretical eigenanalysis to extract the eigenmodes of two-dimensional transitional boundary layers. This was not possible before without making an assumption regarding the form of the two-dimensional disturbance such as is done in the development of the Orr-Sommerfeld equation. The modern computational methods used in these studies for extracting the eigenmodes from a discretised system make no assumption regarding the form of the disturbance, allowing stability information to be extracted from the discretised system of a wider range of problems, including finite systems.

Along with the development of improved and more accessible computing power and the development of more detailed two-dimensional numerical studies, there was also a flurry of studies that employed three-dimensional and DNS studies of boundary layer flow with a compliant wall. The more recent study of Wang et al. [82] is possibly the most detailed numerical study of the three-dimensional system to date.

2.3 Discrete Vortex Methods (DVM)

Discrete vortex methods fall under the broader category of particle methods and are a means of solving certain equations using radial basis functions. Generally, each vortex is a Lagrangian element that, mathematically speaking, is a radially based impulse function. The governing equations, written in Lagrangian reference frame, are solved so that numerical integration (or summation) of these elements satisfies the equations. These methods, taken in their pure form, are computationally expensive because all particle-particle interactions are generally required to be computed at each time-step. This results in an n-body problem that scales as the square of the number of particles. This is in opposition to grid-based methods where only neighboring elements interact, generally resulting in sparse-diagonal matrices that are efficiently solved by linear-algebra techniques.

The first use of particle methods for solving n-body problems can be dated as far back as 1687 when Newton [59] developed his universal law of gravitation. The universal law of gravitation states the attraction between bodies as being a radial basis function where the force of attraction $F \ \alpha \ 1/r$. Newton solved the two-body problem completely. The complexity of the problem grows considerably for $n = 3$ and is the famous three-body problem, and is as yet unsolved exactly in general form. Numerical solution to the n-body problem became the only practical solution method. Since that time, the interaction of thousands to millions of particles have been determined numerically, many more equations have been developed that benefit from solution using particle methods.

Although DVMs are a computationally intensive method of solving problems, the first use of a particle method in application to a fluid system was before the advent of automated computing equipment. In 1931, Rosenhead [71] used manual methods to calculate the interaction of twelve vortex elements using the Euler equations over four time-steps. He obtain reasonable agreement to experimental observations of Kelvin-Helmholtz instability in an inviscid shear layer. Early solutions to fluid mechanics problems were solutions to the inviscid Euler equations and solved two-dimensional problems of shear-layers, such as the Kelvin-Helmholtz instability, or two-dimensional mixing layers.

The pioneering work of Chorin [21] involved the first major use of the DVM to simulate slightly viscous fluid flow around complex geometries (a circular cylinder). In this study, the maximum number of particles by the end of each simulation was approximately three hundred. Considering the coarse discretisation, excellent agreement was achieved with experiment for drag measurements. However, the importance of this work was that it was the first implementation of a diffusion model into the DVM. Using a random walk method (RWM) that relates practically to Brownian motion the position of the vortex particles were randomly adjusted to stochastically solve the diffusive term of the Navier-Stokes equation.

Before the first use of a diffusive vortex method to simulate flow with a random-walk diffusive model by Chorin [21], earlier models studied simply the inviscid flow development with the DVM. Since that time, there have been many methods developed to model the diffusive term with the DVM. A review and comparison of modern methods for implementing viscous effects into vortex methods is presented in Takeda et al. [78] and Liu et al. [52].

2.3.1 Fast Algorithms

An inherent problem with DVMs is that, taken in its pure form, the interactions of each vortex with every other is required to be calculated. Straightforward evaluation of the problem requires a computational load of $O(n^2)$, where n is the number of vortex elements in the computational domain. However, due to the nature of the radial basis function that define each element, two or more elements that are ‘close’ together and far from an evaluation point may be considered to be a single element from the point of view of the evaluation point, given that a certain amount of error is accepted. Combining these elements introduces a quantifiable error, meaning that accuracy can be defined *a priori*. This is the principal upon which fast summation algorithms are based.

There are many methods for increasing the efficiency of evaluating these sums. Most rely upon a detailed analysis of the pairwise interaction and permit rigorous *a priori* error bounds. Some of these methods include; the particle-in-cell (PIC) methods adopted by Chung and Doorly [22]. Multigrid solvers and multipole expansion methods adopted by Greengard and Rokhlin [37], [38] and Rokhlin [70]. Also, heirarchal solvers by and various adaptations of fast methods (usually FMMs) for arbitrary kernel functions, such as Draghicescu and Draghicescu [24] have been developed.

A popular method, defined by Sullivan and Dongarra [77] as one of the top ten algorithms of the 20th century, is the Fast Multipole Method (FMM). The FMM was developed in 1987 by Greengard and Rokhlin [37]. Further development work was carried out by Carrier et al. [19]. An excellent review of the mathematics governing the FMM is given in Beatson and Greengard [10]. In the present work we are concerned primarily with the FMM for the Laplace equation (which corresponds to inviscid fluid flow). However, FMMs exist for other equations such as the Gauss equations, see Greengard and Strain [38], and the Helmholtz equations, see Rokhlin [70].

Fast multipole methods rely upon multipole expansion techniques to group elements that are far from an evaluation point and treat them as a single element. Grouping elements that are far from an evaluation point is a reasonable assumption when one considers that the influence of these elements is typically very small compared to near elements. For a distribution of n radial basis functions, the computation required to calculate all particle-particle interactions will be of the order $O(n^2)$. Using FMM's, this computation is typically reduced to $O(n \log(n))$ (and in some cases lower to $O(n)$), thereby greatly improving computational efficiency. Using multipole expansions allows the error to be precisely quantified.

2.4 Discussion

The use of DNS to study the development of boundary layer disturbances yields direct flow patterns and pressure measurements as would be achieved in a perfectly measured experiment. That is to say, in the process of directly solving the equations, much of the useful information contained within the equations regarding stability must be retrieved through post-processing. DNS methods require enormous amounts of post-processing *after* the already computationally intensive simulation has been performed in order to acquire useful system information. In this regard, DNS analysis is not an elegant means by which to analyse a system as it relies upon consideration of the *results* from the governing equations rather than consideration of the actual system equations and characteristics.

The eigenanalysis methods of Ehrenstein and Gallaire [26] retain this information by using theoretical stability analysis across a discretised computational grid. Adopting this method was not possible until the late 1990's because the solution requires extracting the eigenvalues (and eigenmodes) from massive systems of linear equations; Ehrenstein and Gallaire [26] mention 25,000 or more linear equations for a finite section of boundary layer. Using computational algorithms such Arnoldi algorithms based on Krylov subspace projection techniques, the extraction of eigenvalues from this large set of equations can be made simpler. However, the fact remains that enormous computing power will always be required to perform the iterative processes that these algorithms demand. This method of obtaining the eigenvalues of fluid systems shows great promise for extracting information from systems where eigenanalysis was previously unattainable, such as that required for finite-length compliant walls. However, by its very nature these methods will always be restricted to the study of linear systems, as eigenvalues cannot be attained for non-linear systems. There also remains an issue of studying three-dimensional systems for two reasons: firstly, the number of linear equations increases dramatically for three-dimensional systems becoming once again prohibitively large; and secondly, some of the fundamental variables used to represent the two-dimensional fluid system in these studies and make the solution possible (such as streamfunction) have no relevance when considering the three-dimensional system.

Both grid and particle methods have many advantages and disadvantages associated with them. However, for the particular problem of investigating the compliant wall problem in the current work, DVM's have two distinct advantages over other methods. Firstly, DVM's taken in their purest form do not require any artificially created grid or meshing of the computation domain. The vortex particles, which are the computational elements, tend to convect towards and give greater resolution at places where the most 'action' is happening. In this sense, the DVM is a 'naturally adaptive' mesh technique. This is beneficial for compliant wall (and flow-structure interaction problems in general) because it eliminates the need for complex calculation of grid adaptation and variation of grid resolution depending upon the moving coupled boundary condition. Secondly, the velocity-vorticity formulation of the governing fluid-transport equations, the Navier-Stokes equations, make no assumption regarding the nature of the flow. Therefore, the numerical DVM solution method captures the flow instabilities and large-scale vortical structures without the need for turbulence models as with Reynolds-averaged (RANS) grid-based solution techniques, while still being computationally cheap compared to most Direct Numerical Simulation (DNS) techniques. This makes the DVM suitable for high Reynolds number flows without the need for resorting to *ad-hoc* turbulence models, such as RANS models, or computationally expensive DNS techniques. This is beneficial for efficient and accurate solution of the flow field over a compliant wall at transitional Reynolds numbers.

As stated in Carpenter [14], most experimental studies into compliant panels use an artificial driver to excite the boundary layer and create the two-dimensional TS waves. As such, most theoretical studies implicitly address this artificial situation. The work presented in this thesis differs slightly from this practice. In this work, an inherently noisy DVM is used that will 'naturally' affect boundary layer instability. While the nature of the resulting boundary layer instabilities will not be as 'clean' as those artificially created, it presents a much truer representation of natural transition mechanisms brought about by freestream turbulence, vibration and/or roughness. As a result, it is hypothesised that natural transition might be observed through the DVM. As a result, some new insights into the receptivity of the boundary layer might be found through the work with the DVM in this thesis.

2.5 Conclusion

With regards to Gray's paradox and the swimming of dolphins, the results of Fish and Clifford [27] suggest that skin compliance plays little to no role in any drag reduction. Actually, the evidence shows that there are no special drag-reduction properties of dolphin-skin aside from the streamlined shape of the creatures' body. While this disputes the seed from which the idea of wall compliance for boundary-layer control was born, this does not indicate that wall compliance cannot be a valid engineered means of obtaining boundary layer control. On top of this, when one considers the photos of the experiments shown in Figure 1.2 some flow-induced vibration may be seen on the skin surfaces. However, considering the likely high swimming speed of the dolphin, along with the observable wavelength and amplitude of disturbances on the skin, it is likely that in these cases non-linear effects are occuring which would actually destabilise the boundary layer and increase skin-friction drag.

The early results of Kramer [45] as well as later experimental work by Gaster [33] give indisputable evidence that wall compliance does achieve significant drag reduction given the correct conditions. However, there is still debate over the nature of this reduction, if this is a result of boundary layer transition delay or reduction in turbulence. The theoretical and numerical investigations of Carpenter and Garrad [17] and Carpenter and Davies [15] indicate that, at least theoretically, boundary layer transition can be delayed by means of wall compliance.

The primary difference between experimental and theoretical investigations is that theoretical investigations operate in an idealised environment. For example, two-dimensional boundary layer stability problems based on Orr-Sommerfeld type equations coupled with wall compliance could show that wall compliance can reduce skin friction drag. However, this investigation would ignore factors such as non-linear and/or random forces outside the boundary layer that could excite the compliant wall, 'triggering' a non-linear response in the fluid/flexible wall system from the outset and perhaps *increasing* drag on the system. In this sense, when drag-reduction is a possibility the *stability* of this balance point that the FSI system is sitting where drag-reduction is possible remains uncertain. The result of analysing the FSI system in an idealised environment is that certain studies may show isolated instances where drag-reduction is possible, but these reductions may not be possible in reality due to other factors that are ignored in the idealised experimental lab and theoretical studies.

This is just one example of the inherent noise and non-linearities that would be present in a 'real' operating environment (in an engineering sense). For a compliant wall to be practical, it must operate in a broad range of environments. In any real implementation there would be many factors influencing the fluid/wall system, some of which are external to an idealised theoretical/numerical (even well controlled experimental environments) and are therefore not considered in these investigations.

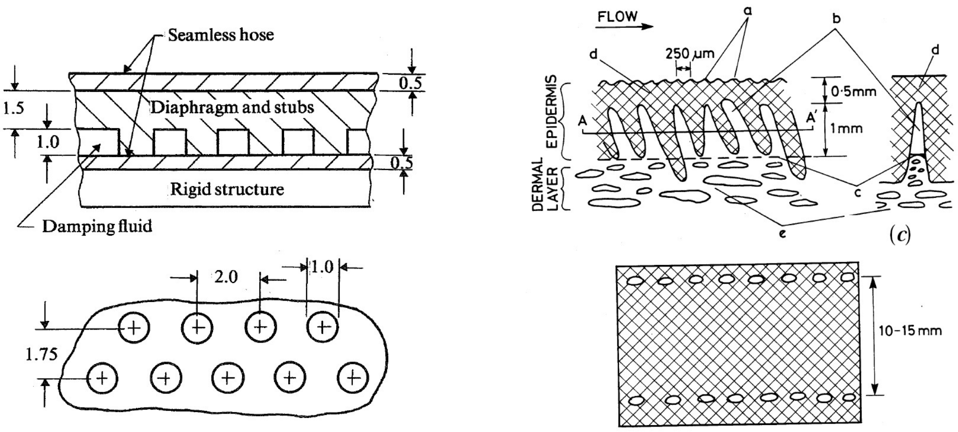

(a) (b)

Figure 2.1: Schematic diagrams showing profile (top) and plan (bottom) view of: (a) The Kramer-type artificial dolphin skin and (b) an actual dolphin epidermis. Taken from Carpenter et al. [16], originally from Carpenter and Garrad [17].

Part II

The ideal-flow model

Chapter 3

Unsteady Ideal-flow Model

3.1 Introduction

The analysis of the fluid-structure system using ideal flow models is less computationally expensive than boundary layer DNS-type simulations. It also allows a variety of traditional analytical techniques to be applied to the governing equations, which can be reduced to second-order linear systems. In order to achieve a fuller understanding of the wall dynamics, frequencies and mode-shapes at steady-state times a non-linear potential-flow model will be developed. However, the ideal flow model does not consider fluid dynamics within the boundary layer. Later in Chapter 5 a Discrete Vortex Method (DVM) is developed to model these fluid dynamics. This DVM model is robust and efficient as compared to other similar boundary layer analysis techniques. However there are certain system characteristics, such as steady-state wall-response dynamics where it remains more efficient to investigate with the ideal-flow model. By using a combination of the ideal-flow model along with the DVM model, compliant coatings may be analysed holistically.

Coupling the information achieved through the application of the ideal-flow method with the results from the DNS-like results of the boundary layer model will give significant insight into the stability and drag-reduction potential of compliant panels.

3.2 Full non-linear model development

The non-linear ideal flow model developed is based on the model of Lucey et al. [56] with some small improvements made to the core solution methodology (particularly for the non-linear fluid mechanics). Therefore, for brevity only the pertinent features of the model development will be discussed here, the reader is directed to the above reference for further details. The development of the model can be broken into three main sections that are presented below. Firstly an overview of the wall mechanics is presented, then the ideal-flow solution methodology and pressure determination. Finally, the method for fully coupling the flow-structure system is presented.

3.2.1 Wall mechanics

The representation of the wall that is used in this research approximates a spring-backed flexible plate with damping. The wall motion is governed by the standard one-dimensional beam equation with consideration for backing-springs and damping and non-linear effects being introduced through an induced-tension term

$$\rho_W h\ddot{w} + d\dot{w} - T_I\left(w_{,x}\right)w_{,xx} + Bw_{,xxxx} + Kw = -\Delta p\left(\ddot{w},\dot{w},w\right) \qquad (3.1)$$

where B is the flexural rigidity of the plate and T_I is the induced tension coefficient given by

$$B = \frac{Eh^3}{12\left(1-v^2\right)} \quad , \quad T_I = \frac{Eh}{L\left(1-v^2\right)}\int_0^L [(1-w_{,x}^2)^{\frac{1}{2}}-1]dx \qquad (3.2\text{a, b})$$

Following the method of Lucey et al. [56] the wall is discretised into a finite number of panels and the wall mechanics given by 3.1 are solved using a standard finite difference representation. This allows a natural unison with the boundary element method of the fluid solver.

3.2.2 Flow Solution and Pressure evaluation

The flow solution is formed by using potential-flow singularities to enforce the no-velocity flux condition in the normal direction at the wall. Figure 3.1 shows a schematic of the potential-flow elements highlighting the difference between the linear and non-linear calculation.

For a linear fluid model the flow elements lie on the x-axis while the wall oscillates with small amplitude/curvature. In the non-linear case the fluid boundary-elements move with the wall. This is a more intuitive way of dealing with the problem and results in better modelling at large wall amplitudes/curvatures. At small amplitudes it is shown later that the two methods converge to the same result. In both cases, the strength of the elements are determined by solving the set of equations that ensure no normal velocity flux through the deformed wall. The linear fluid model has the advantages of reducing the equations to a linear form (to allow for linear analysis techniques), and reducing computational load by removing the need to recalculate influence coefficient matrices (and invert them) at each timestep of the simulation.

The choice of potential-flow element is arbitrary. However it is most common in the case of studies of single-sided compliant panels, such as Lucey [53], Lucey and Carpenter [55], Lucey et al. [56] to use source/sink elements because of their independence on normal velocity influence when they lie in the horizontal plane. Therefore, using source/sink elements all panels are independent of the others in a linear-fluid calculation. Using other elements such as vortices or doublets is possible, and has been done for validation in this work. However these elements have inter-dependence on the normal velocity flux. This not only means that matrix inversion will be more computationally expensive but upstream and downstream 'splitter plates' are required in order to prevent flux passing through the upstream and downstream solid boundary. The length of these splitter plates introduces a new arbitrariness into the calculation that must be checked.

The development of the governing equations and solution methodology that is presented below focuses primarily upon the non-linear fluid model. It will then be shown that the governing equations of the linear system can be easily extracted from the full non-linear system.

The unsteady Bernoulli equation dictates the pressure distribution along the wall at control points i. By applying Bernoulli's equation to an unsteady streamline from a point far from the wall to a point on the wall and neglecting height differences we get

$$\Delta p_i = p_i - p_\infty = \frac{1}{2}\rho(U_\infty^2 - v_i^2) - \rho\dot{\phi}_i \ . \tag{3.3}$$

The tangential velocity at the wall v_i is determined by considering the normal and tangential velocity at the panel control point

$$v_i = \sqrt{(U_\infty \cos\alpha_i + u_{Ti})^2 + U_{Ni}^2} \ . \tag{3.4}$$

By substituting Equation 3.4 into 3.3 an expression for the wall pressure relative to the mean-flow pressure is

$$\Delta p_i = p_i - p_\infty = \frac{1}{2}\rho(U_\infty^2 - (U_\infty \cos\alpha_i + u_{Ti})^2 - U_{Ni}^2) - \rho\dot{\phi}_i \ . \tag{3.5}$$

For an array of potential-flow elements as shown in Figure 3.1 the strength of each element may be calculated by enforcing the zero normal velocity flux condition at the wall. Thus, the strength of each panel-element i must satisfy the linear system of equations that govern the wall-normal velocity at all other elements m. This can be expressed as the matrix equation

$$[N_{im}]\sigma_m = U_\infty \sin(\alpha_i) + U_{Ni} \ . \tag{3.6}$$

From Equation 3.5 the rate of change of velocity potential $\dot{\phi}_i$ is the unsteady component of the pressure determination. The velocity potential is both a function of geometrical position and element strengths, both of which are a function of time. Therefore, the full time-derivative of the velocity potential consists of the addition of two parts

$$\dot{\phi}_i = \Phi_{im}\dot{\sigma}_m + \dot{\Phi}_{im}\sigma_m \ . \tag{3.7}$$

By taking the time derivative of Equation 3.6 and solving for σ by pre-multiplying both sides by N_{im}^{-1} gives an expression for the rate of change of element strengths

$$\dot{\sigma}_i = N_{im}^{-1}(U_\infty\dot{\alpha}_i \cos\alpha_i + \dot{U}_{Ni}) - N_{im}^{-1}\dot{N}_{nm}\sigma_m \tag{3.8}$$

Substituting 3.8 into 3.7 gives an expression for the rate of change of velocity potential at the wall

$$\begin{aligned}\dot{\phi}_i =& \Phi_{im}N_{nm}^{-1}\left[\left\{\frac{\cos(\alpha)}{2}\right\}_n \times \left(\{\ddot{w}\}_n + \{\ddot{w}\}_{n-1}\right)\right] \\ &+ \Phi_{im}N_{nm}^{-1}\{U_\infty\dot{\alpha}\cos(\alpha)\}_n \\ &- \Phi_{im}N_{nm}^{-1}\left[\left\{\frac{\dot{\alpha}\sin(\alpha)}{2}\right\}_n \times \left(\{\dot{w}\}_n + \{\dot{w}\}_{n-1}\right)\right] \\ &+ \left[\dot{\Phi}_{in} - \Phi_{im}N_{nm}^{-1}\dot{N}_{jn}\right]\sigma_n\end{aligned} \tag{3.9}$$

For a linear flow solution the rate of change of the spatial influence matrices is zero. If source elements are used then $N_{nm}^{-1} = 2$. Therefore, the above Equations 3.9 and 3.5 reduce to

$$\Delta p_i = \rho U_\infty u_{Ti} - \rho\dot{\phi}_i \tag{3.10}$$

$$\dot{\phi}_i = \Phi_{im}\left(\{\ddot{w}+\}_n\{\ddot{w}\}_{n-1}\right) + \Phi_{in}2U_\infty\dot{\alpha}_n \tag{3.11}$$

For the linear method, the influence coefficients only need to be calculated once in a linear simulation as the influence coefficients do not change. Therefore also the matrix of influence coefficients only needs to be inverted once for a linear calculation. This demonstrates the efficiency of the linear as opposed to non-linear calculations.

3.2.3 Coupling the system

The solution of the fully coupled system may be achieved by grouping the node-acceleration terms on one side of the equation. By substituting the governing equations for fluid pressure in Equations 3.7 and 3.5 into the wall Equation 3.1, a unified equation for the spacio-temporal motion of the wall is obtained that has the form

$$B_{im}\left\{\ddot{w}\right\} = F_i\left(w,\dot{w}\right) \tag{3.12}$$

where for the case of non-linear fluid modelling

$$\begin{aligned}
B_{im} &= \rho_W h - \Phi_{im} N^{-1}_{nm} \left\{ \frac{\cos\left(\alpha\right)}{2} \right\}_n \\
F_i\left(w,\dot{w}\right) &= T_I\left(w_{,x}\right) w_{,xx} - d\dot{w} - Bw_{,xxxx} - Kw - p_{s1} - p_{u1} - p_{u2} \\
p_{s1} &= \frac{1}{2}\rho(U_\infty^2 - \left(U_\infty \cos\alpha_i + u_{Ti}\right)^2 - U_{Ni}^2) \\
p_{u1} &= \rho\Phi_{im} N^{-1}_{mn}\left[\left\{\dot{\alpha}\frac{\sin\left(\alpha\right)}{2}\right\}_n \times \left(\left\{\dot{w}\right\}_n + \left\{\dot{w}\right\}_{n-1}\right)\right] \\
&\quad - \rho\Phi_{im} N^{-1}_{mn}\{U_\infty \dot{\alpha}\cos\left(\alpha\right)\}_n \\
p_{u2} &= \rho\left[\dot{\Phi}_{in} - \Phi_{im} N^{-1}_{mj}\dot{N}_{jn}\right]\sigma_n
\end{aligned}$$

and for the case of linear fluid modelling

$$\begin{aligned}
B_{im} &= \rho_W h - \Phi_{im} \\
F_i\left(w,\dot{w}\right) &= T_I\left(w_{,x}\right) w_{,xx} - d\dot{w} - Bw_{,xxxx} - Kw - p_{s1} - p_{u1} \\
p_{s1} &= \rho U_\infty u_{Ti} \\
p_{u1} &= \rho\Phi_{im}\left(\left\{\dot{w}\right\}_n + \left\{\dot{w}\right\}_{n-1}\right) + \rho\Phi_{im} 2U_\infty \dot{\alpha}_n
\end{aligned}$$

The resulting Equation 3.12 may be solved for the wall acceleration $\ddot{w}_i$ and therefore the wall position w_i by a suitable time-integration technique.

3.3 Analytical Methods

The numerical simulation model developed above may be solved explicitly through time from some initial condition. This is useful for investigating transience or investigating ‘real’ (ie. arbitrary or no presupposed form of the solution) panel motion. However, for investigating the nature of the motion at steady state it would require that the simulation be run for very long times at a great deal of computational effort. Perhaps a greater problem is that the simulation would not readily produce (without a great deal of post-processing) information regarding the make-up of the steady state response such as mode shape and oscillation frequency. In this regard, using the method in an explicit time-stepping simulation suffers from the same problems of extracting useful information as DNS-type techniques.

Adopting some well established techniques to study these features will allow a more thorough investigation of the steady-state response of such flow-structure interaction. The techniques adopted below involve reducing the system of equations presented in 3.12 down to a set of tempo-spatial second-order differential equations. Eigen-analysis techniques can then be used on these systems of first-order differential equations to yield information regarding the steady-state response of the linear system.

Two methods of solving the linear steady-state system are presented below. The first is a new technique that involves extracting the system eigenvalues directly from the discretised system. The second is the Galerkin method, first utilised by Weaver and Unny [83] in FSI analysis, which is popularly adopted for the solution of such linear FSI problems. The Galerkin method regards the solution as a summation of orthogonal modes (a perfectly correct assumption for a linear system). These orthogonal modes are typically the natural modes of the *in vacuo* wall system. This representation by a summation of modes reduces the number of unknowns to the number to orthogonal modes that were chosen. The first method is more computationally intensive, but has the advantage of making no arbitrary assumptions regarding the number and form of the superposed orthogonal modes that make up the system solution.

3.3.1 Direct Eigen-analysis of the discretised system

In the development of the numerical simulation, Equation 3.12 was solved. Using the linear form of the equations that are in Equations 3.10 and 3.11, in fully-expanded form, this Equation 3.12 becomes

$$\ddot{\eta} = [M]^{-1}\{-q\dot{\eta} - [C]\eta + \rho U_\infty[T_{nm}]\sigma + 2\rho U_\infty[\Phi_{im}]\dot{\alpha}\} \tag{3.13}$$

where

$$\begin{aligned}
[C] &= B[I] + K[I] \\
[M] &= \rho_w h[I] - [I_\Phi][I_N]^{-1} \\
[I] &= Identity \quad Matrix
\end{aligned}$$

where σ may be determined from Equation 3.6 as

$$\sigma_m = U_\infty[N_{im}]^{-1}\sin(\alpha_i) + [N_{im}]^{-1}U_{Ni}\ . \tag{3.14}$$

For linear wall motion it is known that the sine of the panel angle and the rate of change of the panel angle can be expressed in terms of η respectively as

$$\sin(\alpha_i) = \frac{d}{dx}\eta \tag{3.15}$$

$$\dot{\alpha} = \frac{d}{dx}\dot{\eta} \tag{3.16}$$

substituting Equations 3.16,3.15 and 3.14 into Equation 3.13 gives a matrix equation for the motion of the wall with the only variables being $\ddot{\eta}$, $\dot{\eta}$ and η

$$\begin{aligned}
\ddot{\eta} = [M]^{-1}\{ &- q\dot{\eta} - [C]\eta + \rho U_\infty[T_{nm}][N_{nm}]^{-1}[\frac{d}{dx}]\eta \\
&+ \rho U_\infty[T_{nm}][N_{nm}]^{-1}\dot{\eta} + 2\rho U_\infty[\Phi_{im}][\frac{d}{dx}]\dot{\eta}\}
\end{aligned} \tag{3.17}$$

By continuing to spatially discretise the system, the linear second-order matrix equation given in 3.17 for the motion of the wall node points may be simplified to give set of coupled linear second-order ordinary differential equations through time for the node-point displacements

$$\ddot{\eta} = [A]\dot{\eta} - [D]\eta \tag{3.18}$$

following the procedure of state-space analysis, this second-order linear differential equation may be reduce to a set of $2N$ coupled linear first-order differential equations. By stating that $x_{2i-1} = \eta_i$ and $x_{2i} = \dot{\eta_i}$ and applying this to the set of equations given by 3.18 then the second-order system may be reduce to a first-order system that is

$$\{\dot{x_i}\} = [H]\{x_i\} \tag{3.19}$$

where

$$[H]\{x_i\} = \begin{bmatrix} 0 & I \\ -D & A \end{bmatrix} \begin{Bmatrix} \eta \\ \dot{\eta} \end{Bmatrix}$$

following the normal procedure for solution of a first-order differential equation and assuming that the solution takes the form of $x_i = X_i e^{st}$ and substituting this into 3.19 gives the set of coupled linear equations

$$\left[s[I] - [H]\right]\{X_i\} = 0 \tag{3.20}$$

for which non-trivial solutions exist when $|s[I] - [H]| = 0$. This is a typical eigenvalue problem required to search for eigenvalues in s.

The only problem with the solution of this linear system is that the number of linear equations makes extraction of the eigenvalues difficult and computationally expensive. For the typical flexible walls that are considered in this study, the wall will be discretised into 400 panels. This will yield a set of 800 first-order linear equations for which the eigenvalues must be found. Without the use of special computational algorithms the solution of this system of equations would not be possible, or would be very computationally expensive. It is interesting to note that this type of eigen-analysis of large sets of linear equations is not unheard of. Ehrenstein and Gallaire [26] and Marquillie and Ehrenstein [58] use a similar approach for the analysis of boundary layer instabilities over rigid surfaces. In these cases the number of equations reaches up to 25,000 or more.

Fortunately, a computational algorithm for the solution of these large systems of equations does exist. Actually, there are several algorithms by which to extract eigenvalues from large-scale systems of equations. However, most of these algorithms rely upon the theory of Krylov subspace projection which implies that the user will not get *all* of the eigenvalues of the system. This is possibly a good thing because N sets of equations will yield N eigenvalues. In the case of 800 or more equations, the number of eigenvalues returned will be prohibitively large and for the most part useless. Rather, eigenvalues which exist close to a certain point of interest are generally the only eigenvalues required. This is what the Krylov subspace projection methods allow for, a user-defined set of eigenvalues, say n, that are the closest eigenvalues to a point of interest. Further discussion on the algorithms are outside the scope of this work, but for further information the reader is referred to Baglama et al. [7], Lehoucq and Scott [49], Lehoucq et al. [50], Lanczos [46], Paige [61] and Saad [74].

In this study, a black-box solver adopted through the MATLAB computer package. MATLAB in turn uses the ARPACK[1] solver through the EIGS command which iteratively solves for the eigenvalues. The ARPACK routine allows the n eigenvalues closest to some complex point value to be determined.

Extracting the eigenvalues with the lowest absolute value gives the lowest n eigenvalues. Substitution of these eigenvalues back into 3.20 gives a set of N homogeneous equations, meaning that the amplitudes of all nodes may be solved relative to one[2]. This returns the eigenmodes for the corresponding eigenvalues of s.

---

[1] ARPACK is an acronym for ARnoldi PACKage. It is a FORTRAN77 subroutine for the solution of large-scale, non-symmetric eigenvalue problems. For further information refer to Lehoucq et al. [50]

[2] this stage of substitution is not required in reality because the ARPACK routine can also return the n eigenvectors associated with the n eigenvalues

Significance of Complex Terms

Substitution of the eigenvalues (s) returned from the solution of Equation 3.20 can be substituted back into Equation 3.19 to give the frequency of the wall motion. Given that the eigenvalue s is a complex number of the form $s = F + Gi$ then the motion of each node on the wall takes the form

$$x_i = X_i e^{(F+Gi)t} = X_i e^{Ft} \left(\cos(Gt) + i \sin(Gt)\right) \tag{3.21}$$

As expected, this indicates that the frequency of wall oscillation is dictated by the imaginary part of the eigenvalue and the growth or decay of the wall amplitude is dictated by the real part of the eigenvalue. The wall oscillates with a period of oscillation of $T = 2\pi/G$.

The complex eigenvalues no *not* give an indication to any travelling wave type motion of the wall. They only give an indication to the growth and oscillation frequency of the wall motion, not the *form* of the motion. In order to investigate the form of the wall motion, the spatial variation of the amplitude X_i must be considered. The value of X_i may also be complex and the value varies spatially along the wall so that $X = D(x) + iE(x)$. Given this complex form of the wall amplitude, Equation 3.21 becomes

$$\begin{aligned} x_i &= e^{Ft} \left[D(x) + iE(x)\right] \left[\cos(Gt) + i \sin(Gt)\right] \\ &= e^{Ft} \{ [D(x)\cos(Gt) - E(x)\sin(Gt)] \\ &\quad + i\,[E(x)\cos(Gt) + D(x)\sin(Gt)] \} \end{aligned} \tag{3.22}$$

Equation 3.22 indicates that the overall growth or decay of the wall motion is dictated by the real part of the eigenvalue. However, the actual form of disturbance evolution is governed by the complex part of the eigenvalue and the spatial variation of the real and complex parts of the corresponding eigenvector (mode shape). A simple analysis of the significance of the spatial phase difference between $D(x)$ and $E(x)$ may be done by considering the case where both parts are sinusoidal in form. In this case, if both parts have the same amplitude and are in phase (ie. $D(x) = E(x) = \cos(\omega t)$) then the resulting form of the wall oscillation will be that of a standing wave given by

$$x_i = e^{Ft} \cos(\omega t) \left\{ [\cos(Gt) - \sin(Gt)] \right\} \tag{3.23}$$

Note that the complex part of the final wall motion x_i was ignored here. However, if the parts are out of phase (ie. $D(x) = cos(\omega t)$ and $E(x) = sin(\omega t)$) then by applying trigonometric identities it can be shown that the resulting form of the wall motion will be that of a travelling wave by

$$x_i = e^{Ft} \cos(\omega x + Gt) \tag{3.24}$$

3.3.2 Galerkin analysis with in-vacuo modes

Traditionally Galerkin methods, based upon a superposition of *in-vacuo* mode shapes, have been used to investigate the stability and mode shapes of the full system. A review of Galerkin methods and weighted residual methods is given in Appendix C. In order to gain a comparison of these Galerkin methods against the eigenmode search method used above a semi-numerical Galerkin method is developed.

The Galerkin method assumes that the solution consists of some linear combination of orthogonal modes. These can be any orthogonal modes that fit the boundary condition of the system. However, normally in FSI problems such as this the orthogonal modes selected are the natural *in-vacuo* modes of the wall. In this method, the same 'base code' will be used as the state space model presented in Section 3.3.1. Therefore, the method starts from the state-space form of the governing equations that is presented in Equation 3.18.

In the eigenvalue problem of Section 3.3.1 where the only constraint imposed was that of harmonic motion of the wall nodes. The Galerkin method adopted here will further state that the motion of the wall is a linear combination of *in-vacuo* orthogonal modes, so that a particular solution to the fluid-structure system is

$$x_i = [X_m]\{C_m\}e^{st} \tag{3.25}$$

where $[X_m]$ is an $n \times m$ matrix of known orthogonal mode shapes that satisfy the boundary conditions of Equation 3.12, where n is the number of elements used to discretise the wall and m is the number of orthogonal modes selected solve the system. Substitution of this trial solution into Equation 3.18 gives

$$s^2[X_m]\{C_m\} = s[A][X_m]\{C_m\} - [D][X_m]\{C_m\} \tag{3.26}$$

At this point one can solve for s in Equation 3.26 using the companion matrix method that was used to solve for Equation 3.18. The primary differences between the direct eigenanalysis presented in Section 3.3.1 and the Galerkin method presented here are:

- The size of the coefficient matrices in Equation 3.26 are smaller than the coefficient matrices in Equation 3.18;
- The Galerkin method, as shown in Appendix C is a weighted residual method. This implies that an exact solution will not be achieved, as the method relies upon minimising the residual error. The direct eigen-analysis of Section 3.3.1 does not make this assumption.

3.4 Model Validation Results

Three experiments are performed to validate the ideal-flow numerical model. Firstly, the wall in-vacuo oscillation for various mode-shapes will be investigated and compared to theory. Secondly, comparison of results achieved by independently developed codes using various potential-flow elements (vortex, doublet and source/sink) for flow-structure simulations are investigated. Finally, using the source/sink model, the results for both linear and non-linear dynamic simulations will be compared against the work of Lucey et al. [56].

Unless otherwise stated, all of the results achieved below will use the wall and flow parameters used by Lucey et al. [56]. These correspond to wall material properties of an aluminium plate with hinged-hinged end conditions and material properties: $E = 78GPa$, length $L = 1m$, and thickness $h = 0.01m$. The fluid density is $\rho = 1000kg/m^3$, and the mean-flow speed is $U_\infty = 10m/s$. For the computational parameters a timestep size of $dt = 1 \times 10^{-5}s$ was used, with 100 panels used to discretise the compliant wall section.

The eigenmode decomposition code is the same base as the numerical simulation model. Therefore, it is sufficient to validate only the numerical simulation model. Results obtained through the eigenmode decomposition will correlate directly to results obtained through the numerical simulation. Later inspection of these results will be adequate validation of the eigenmode decomposition method alone.

The results obtained for validation of the fluid code presented in Section 3.4.3 are based on the use of source/sink potential-flow elements. Section 3.4.4 compares the use of various potential flow elements (vortex, doublet and sources) for the fluid solver. The results of this section show that all elements give the same result; however, the use of the source elements is a more desirable selection for linear calculations.

3.4.1 In-vacuo wall mechanics

The first step to validating the numerical model is the validation of the wall mechanics for which analytical solutions are well-established. In this case, the fluid density was reduced to near-zero. The wall was then deformed to some initial eigenmode and thereafter allowed to move of its own accord. Oscillation frequency, damping ratio and stability could be measured directly and compared to theoretical solutions of the one-dimensional beam equation.

The theoretical solution to the beam equation to obtain the oscillation frequency for a given eigenmode (M_e) is known as

$$\omega_{theory} = (M_e\pi)^2\sqrt{\frac{EI}{\rho_w A{L_w}^4}} \tag{3.27}$$

Tests were run for the validation of the *in-vacuo* wall mechanics to produce a large validation matrix. The results were non-dimensionalised to facilitate presentation of the results. The spatial discretisation was non-linearised against the modal wavelength. The temporal discretisation was non-dimensionalised against the theoretical period of oscillation obtained from Equation 3.27 as $T = \frac{2\pi}{\omega}$. The results of these experiments are plotted in Figure 3.2.

Note that the results obtained here for in-vacuo wall dynamics are independent of the fluid solver. For this reason the accuracy and/or validity of the ideal-flow solver was not considered here.

3.4.2 State-space model

The state-space model that is used to find eigenvalues and eigenmodes for the steady-state response of the linear wall motion; it uses the same set of equations and 'core' code as the potential-flow simulations. Therefore, the state-space model will suffer from all the same limitations as the potential-flow simulation in terms of *spatial* discretisation. However, the state-space model does not rely upon temporal discretisation and therefore will not suffer from this component of discretisation.

Due to the fact that identical code is used for the wall mechanics, validation of the in-vacuo wall mechanics with the state-space model is not necessary as this is covered in Section 3.4.1.

As a test of the black-box ARPACK solver implemented through MATLAB. Figure 3.3 shows the first four modes shapes that are obtained through the state space model when the fluid density is set to nearly zero ($1 \times 10^{-9} kg/m^3$).

The complex parts of the eigenvalues associated with these eigenmodes give very good agreement with the theoretical frequency of oscillation of an invacuo plate given by Equation 3.27. A plot of the varying error against this theoretical value for various spatial discretisations is presented in Figure 3.2.

3.4.3 Linear/non-linear model validation

For validation of the non-linear model certain results will be compared directly against the results of Lucey et al. [56].

Figure 3.4 shows the results of Lucey et al. [56] along with the results from the model developed in this thesis. The non-dimensional parameters used in this experiment are defined in Lucey et al. [56] as[3]

$$\Lambda^F = \frac{\rho U_\infty^2 L^3}{B},\ w' = \frac{w}{h},\ t' = \frac{\sqrt{E^*/\rho_W}}{L}t,\ E^* = \frac{E}{(1-v^2)} \qquad (3.28\text{a, b, c, d})$$

The model developed in this work is a re-implementation of the code of Lucey et al. [56]. It therefore suffers from the same discretisation errors and limitations as the Lucey model. The results shown in Figure 3.4 demonstrate that the two models give similar results, indicating that no errors were introduced in the re-generation of the Lucey code. Further to this, the additions to the Lucey code were minor and served only to reduce the dependence on temporal disretisation in some terms. Based upon these points, a thorough re-validation of the code is not necessary here and one may refer to Lucey et al. [56] for a thorough validation of the numerical method.

In Lucey et al. [56], the structural damping is defined non-dimensionally as a percentage value (n%) that equates to the percentage reduction in amplitude per cycle of a linear oscillation for the *in-vacuo* case. However, this does not allow for over-damped cases as there would be no second oscillation by which to measure the percentage reduction in amplitude. Therefore, in the present work the damping is defined non-dimensionally through the damping ratio of the first

---

[3] These non-dimensional parameters correspond to the following dimensional parameters that are used in these experiments: $E^* = 78 \times 10^9 Pa$, $h = 0.01m$, $L = 1m$, $\rho = 1000kg/m^3$, $\rho_W = 2600kg/m^3$, $U_\infty = 20m/s$, $K = 0N/m$, $d = 0Ns/m$ (for undamped case) and $d = 900Ns/m$ (for 50% damping)

mode of the *in-vacuo* system as

$$\zeta = \frac{d\left(L^2\right)}{2\sqrt{\rho A\left(EI\pi^4 + K\left(L^4\right)\right)}} \tag{3.29}$$

3.4.4 Comparison with different flow elements

The choice of potential-flow element (vortex, source/sink or doublet) should not influence the final results. The only difference should be that the source/sink elements do not show streamwise inter-dependence for linear-amplitudes. Therefore, identical results should be achieved regardless of the flow elements used. In this experiment, the results of 3.4 are replicated using different computational elements for the BEM. Namely, first-order vortex and zero-order doublet elements.

The simulation used for this numerical experiment is identical to that of Lucey et al. [56] and that of 3.4. The setup for the three simulation models are identical. However, due to the stream-wise inter-panel relationship of the vortex and doublet methods, an extra parameter was varied for these models only. This parameter is the upstream/downstream splitter plate length. These upstream/downstream splitter plates were not required for the source/sink boundary elements because the source/sink elements do not have a streamwise interdependence in the linear regime. And only a slight interdependence in the non-linear regime of wall deflections.

Three totally separate codes were written that used vortex, source/sink and doublet elements respectively. As a form of validation it should be expected that identical results are achieved for each of these elements. The results of the simulation are presented in Figures 3.5 and 3.6 for the linear vortex and constant doublet sheet elements respectively. Rigid upstream and downstream splitter plates were added of various lengths in order to model the rigid upstream/downstream walls. The length of the upstream/downstream splitter plates are represented as a percentage of the compliant wall length. The results for the linear vortex and constant doublet sheets are in close agreement for all splitter plate lengths. For relatively short splitter plate lengths of 10% of the compliant wall length, there is poor agreement with the results of Lucey et al. [56]. With increasing splitter plate lengths, there is closer agreement with the results from the source/sink model of Lucey et al. [56]. Splitter plate lengths of 100% or more give very good agreement with results from the source/sink model.

3.5 Discussion

The results for the in-vacuo wall mechanics show that the mathematical model for the wall model agrees well with theoretical solutions to the beam equation. Figure 3.3 shows that for a relatively coarse discretisation of $N = 20$ nodes along the compliant wall the *in-vacuo* wall mode shape is accurately determined up to the fourth mode. Figure 3.2 shows that the correlation between the non-dimensional spatial discretisation, non-dimensional temporal discretisation and percentage error produced a linear correlation on a log-log plot. It can be seen from the plot that the temporal discretisation does not play as large a role in determining the error as the spatial discretisation. Therefore, in setting up the numerical parameters, special care will be taken with consideration of the spatial discretisation in order to accurately capture the dynamics of the higher modes. The error fluctuates slightly with the change in temporal discretisation because of the rounding to the nearest timestep that occurred in determining the time-period of oscillation.

Figures 3.5 and 3.6 show that with sufficient upstream/downstream splitter plate lengths the the doublet and vortex methods converged to give the same results as the source/sink model. The source/sink method does not have a dependence upon upstream/downstream splitter plate lengths because the source/sink elements do not have a streamwise normal velocity influence interdependence as the vortex and doublet elements do. This is strictly true for only the case of the linear fluid model, where the boundary elements lie on the x-axis. However for the case of non-linear fluid model, where elements are free to move vertically out of this plane the influence remains very small. This is indicated in Figure 3.4a where the linear results are almost identical to the non-linear results. The doublet method slightly differs from the first-order vortex method due to the fact that the constant strength doublet is mathematically similar to two point vortices at the nodes. Therefore, the doublet is a lower-order model and would require higher spatial discretisation of the wall-section to achieve the same convergence the vortex method. The experiment of using different flow elements successfully validated and confirmed the choice of the source elements for the ideal flow numerical simulation in the case of a single sided compliant wall section as is studied in this work. The results also show that for the modelling of other flow situations (such as a two sided flag-like compliant surface) where vortex or doublet methods must be used, then care must be taken to ensure that there is a sufficiently long upstream splitter plate length coupled with an appropriate unsteady kutta boundary condition on the trailing edge.

The eigenvalue decomposition method outlined in Section 3.3.1 returns the eigenvalues and corresponding eigenmodes for a given flow-structure situation. The critical difference between this method and the Galerkin-type methods (based on a superposition of normal-modes) is that no abitrariness is introduced in the form of selecting an appropriate number of orthogonal modes to represent the solution. Therefore, one can be assured of obtaining the correct eigenvalues of the system with no prior knowledge of the form of the solution. For simpler FSI problems such as the ideal flow over a single sided compliant panel studied here, the results from the Galerkin method and the eigenvalue decomposition method should be similar. However, the strength of the eigenvalue decomposition method lies in its ability to be applied efficiently to larger, more complicated systems. The studies shown here are the first cases of such a method being used to extract the eigenvalues directly from an FSI system, however the real potential for the method lies in its application to problems of greater complexity. An example would be a case where orthogonal modes that fit the boundary conditions (as required in a Galerkin method) are difficult to obtain and/or where the substitution of these modes into the weighted residual scheme might prove difficult.

Some minor improvements were made to the non-linear code of Lucey et al.

[56] to give more efficient numerical solution and decreased discretisation dependence. Specifically, Lucey et al. [56] use a time-differencing method to calculate the rate of change of velocity potential whereas this differencing method has been replaced by a method that considers velocities and gradients to calculate the rate of change of the flow velocity potential exactly at any time. This adjustment removes the dependence of parts of the code on the temporal discretisation, thereby increasing the accuracy of the code used in this work.

3.6 Conclusion

A new method, fusing computational modelling and theoretical techniques, for the direct determination of the eigenmodes of finite flow-structure systems has been developed. The method is based upon the direct extraction of the eigenvalues and eigenmodes from the large set of discretised system equations. This method of extracting eigenvalues from large systems of discretised equations has been used before by Ehrenstein and Gallaire [26] for the extraction of eigenvalues and eigenmodes of complex fluid-mechanics systems. The work presented here is the first case where such a technique has been applied to a FSI system. This paves the way for further work into the analysis of more complex FSI systems by this method.

Using the same base code from which the eigenvalues are extracted, a full non-linear model has been developed in the same manner as that of Lucey et al. [56], however with some minor adjustments made to improve efficiency and accuracy.

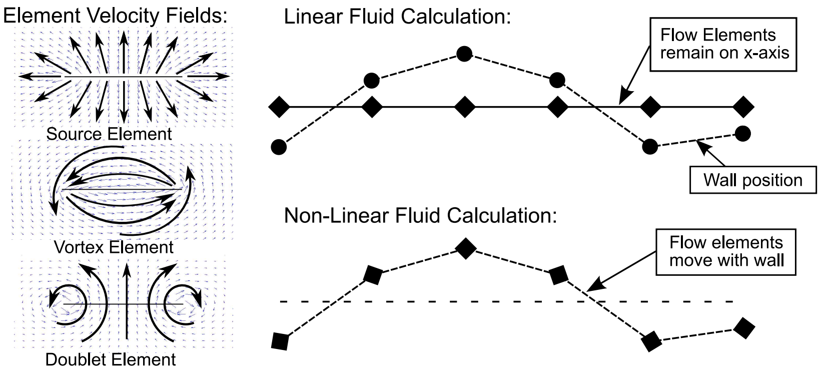

Figure 3.1: Velocity fields for the various flow elements and the position of the elements for linear and non-linear fluid calculation

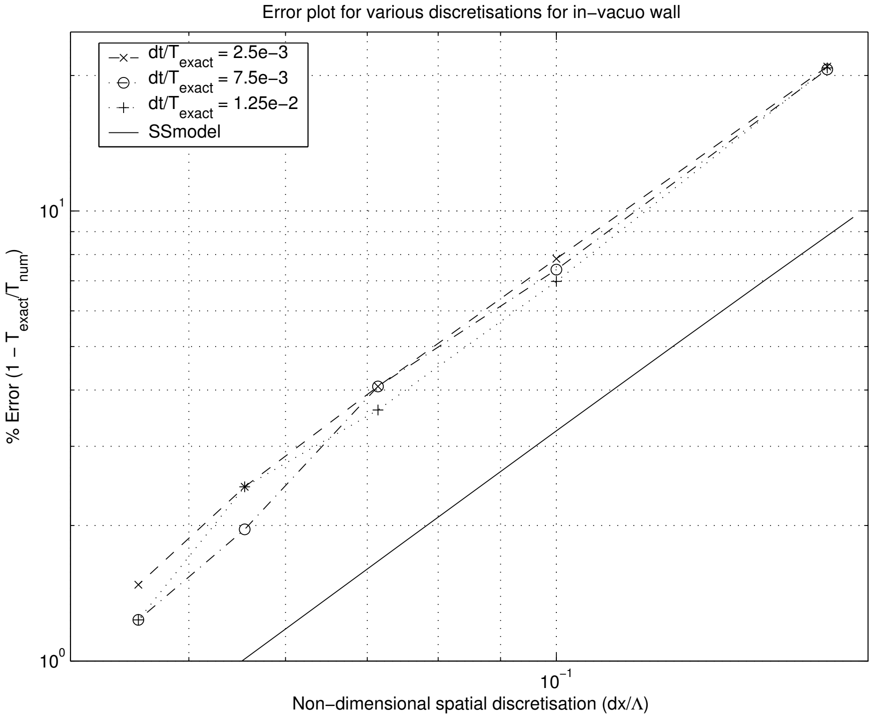

Figure 3.2: Log-Log plot of percentage error against various non-dimensionalised spatial and temporal discretisations for the wall *in-vacuo*

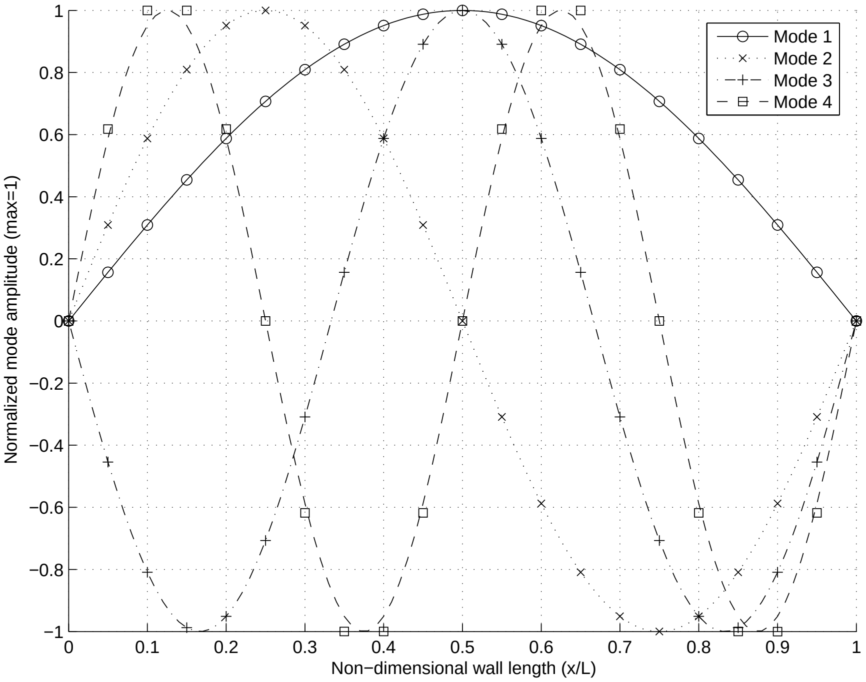

Figure 3.3: Invacuo mode shapes (1-4) obtained from the state-space model

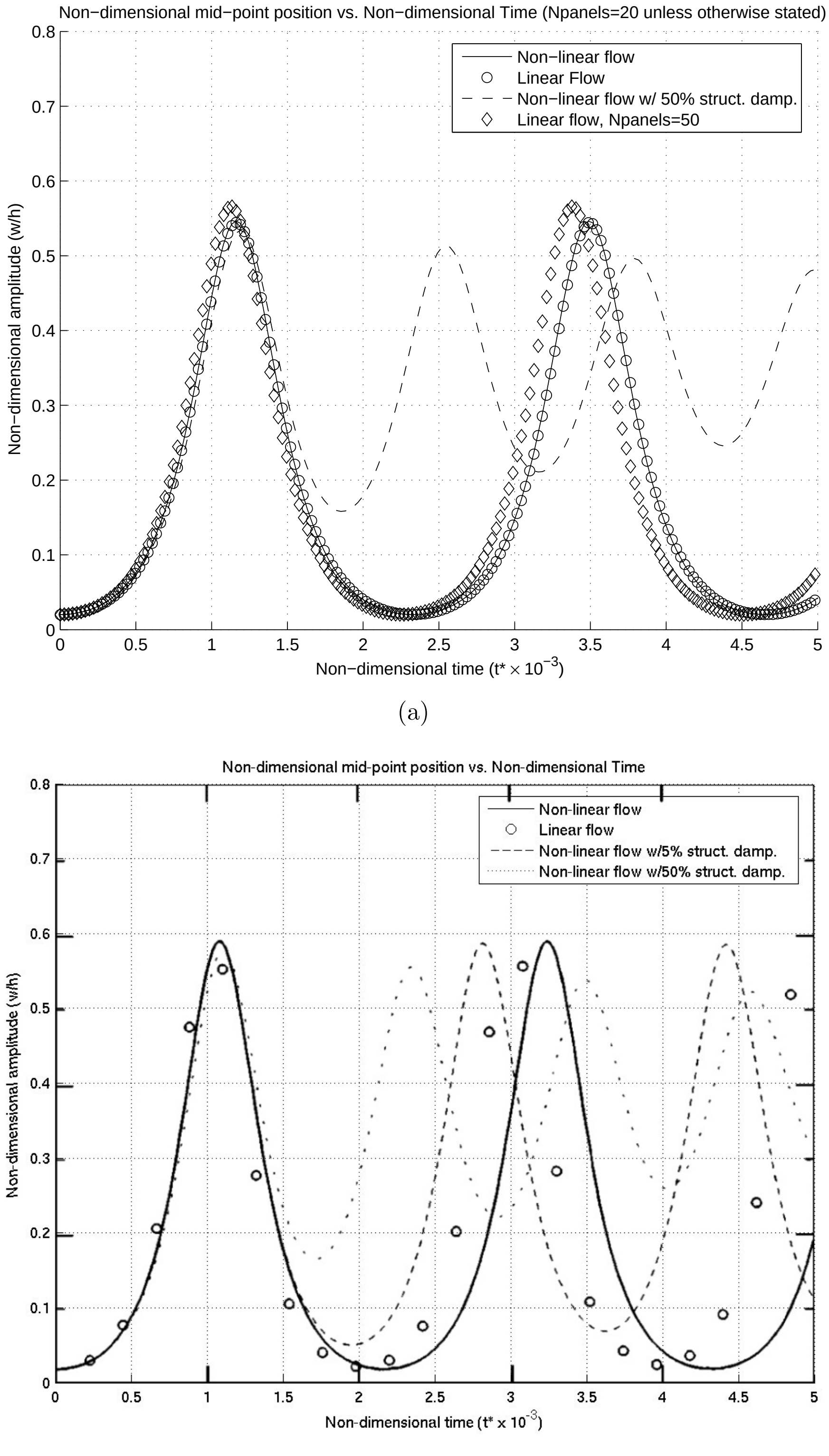

(a)

(b)

Figure 3.4: Mid-point panel position for a) the non-linear potential-flow model developed in this study and b) the non-linear wall model of Lucey et al. [56]

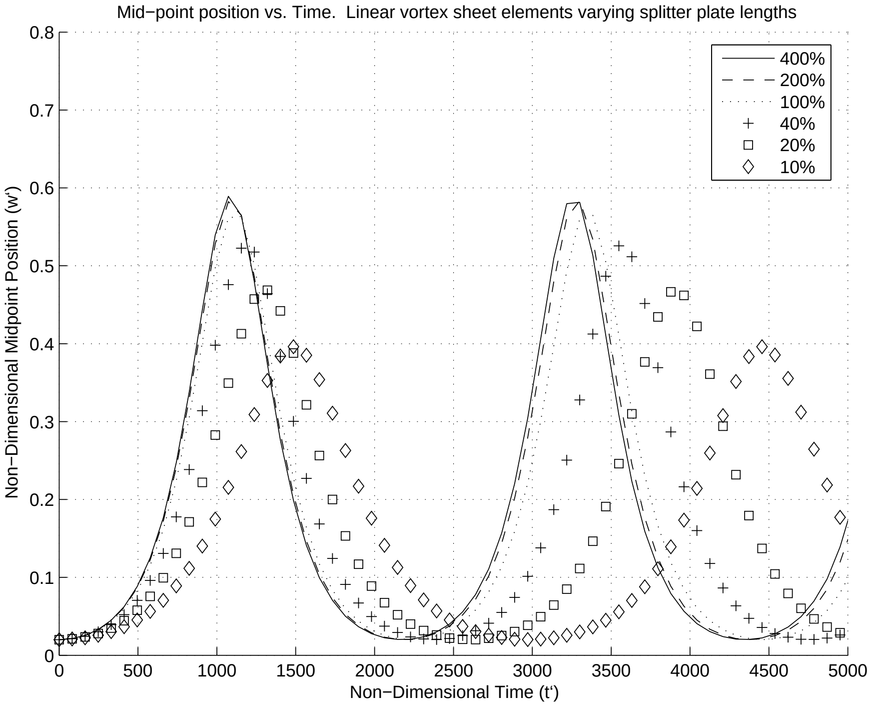

Figure 3.5: Non-linear divergence oscillation ‘bounce’ using linear vortex sheet elements with varying upstream and downstream splitter plate lengths

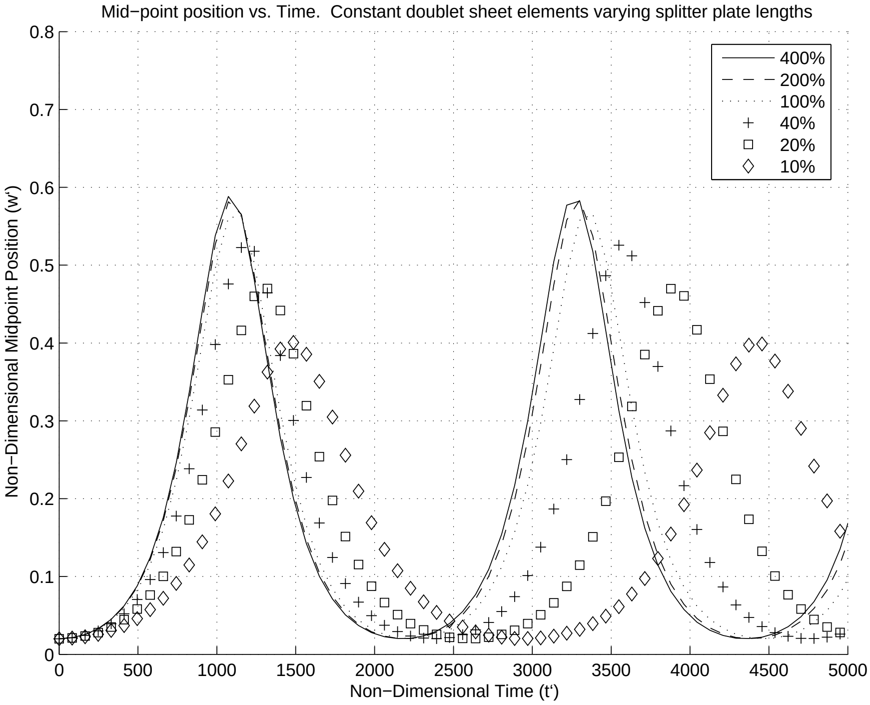

Figure 3.6: Non-linear divergence oscillation ‘bounce’ using constant doublet sheet elements with varying upstream and downstream splitter plate lengths

Chapter 4

Numerical experiments with the ideal-flow model

4.1 Introduction

In this chapter various numerical experiments are reported using the unsteady ideal-flow model that was developed in Chapter 3. The experiments are focused on achieving the objectives stated in the research problem in Section 1.2.2. There are four points of interest that will be investigated with the ideal flow model. These are: linear eigenanalysis, transient disturbance growth, steady-state non-linear responses, and panel edge-effects. Each of these points of interest is aimed at giving information of various aspects of the coupled wall/flow dynamics.

The linear eigenmode analysis gives information detailing the steady-state dynamics of the linear system. Previous work has focused on the linear disturbance evolution because most disturbances that occur in a real system will begin in the linear regime, having a small amplitude with respect to wavelength. Using some of the new techniques adopted in this thesis a more detailed knowledge of the characteristics of wall disturbances can be attained. The eigenmode analysis also has the distinct advantage over the numerical simulation in that it has no temporal discretisation and returns definite information regarding the stability of the system in terms of a modal decomposition.

The investigation of transient mechanisms gives information relating to the growth of an initial disturbance through to steady-state. This is particularly important for comparison between results obtained from the ideal-flow and DVM models. Because the DVM model is very computationally expensive, simulations can not be run until steady-state. Therefore, the comparison of the evolution of disturbances through a transient period will form the basis for most of the comparison between the DVM and the ideal-flow model. An investigation will be performed where the growth of three types of initial disturbances will be observed until they progress through to the long-time response.

The steady-state non-linear response of a compliant panel has not been thoroughly studied before. The investigation of Lucey et al. [56] evaluated the disturbance until large amplitude, however the results indicated that the solution had not settled into a steady state by the end of these simulations. Using the greater computational hardware available at the present time, numerical experiments could be run for much longer times. Investigating several initial condition situations, it will be shown that the final state of the non-linear system is independent of the initial (linear) state.

The effect of panel edge effects is of interest because a great deal of previous work has been focused on the fluid-structure interaction dynamics over infinite domains. Also, due to the computational effort required with the DVM, the majority of investigation will focus on transient disturbance growth where the panel edges may have little or no effect. Therefore, to be able to gain more insight into the full dynamics of the real system, information pertaining to the panel edge-effects for the ideal-flow model may be translated to the effects for the full system, provided that sufficient basis for comparison is achieved through the investigation of transient mechanisms.

4.2 Linear eigenmode analysis

Using the method outlined in Section 3.3.1 the eigenvalues of the steady-state linear system were found along with the corresponding eigenmodes. The integrity and accuracy of the linear code has already been established in Section 3.4 through the comparison of the results with established theory for in-vacuo wall mechanics as well as fluid-loaded cases. The results from this section determined that all results lie within 0.5% of the theoretical values.

4.2.1 Simply supported flexible plate

Using the same parameters as Lucey et al. [56] for the simulation the eigenvalues and corresponding eigenmodes for various mean-flow speeds were investigated. These flow speeds correspond to a variation in the non-dimensional parameter Λ^F, specified in Equation 3.28a, from a value of 0 to 350[1]. For simplicity here, it is best to consider that all wall and flow parameters remaining static *except* for the flow speed which ultimately drives the variation in non-dimensional parameter Λ^F. Therefore, while in this work 'flow speed' refers to the actual variation in flow speed to vary the non-dimensional parameter Λ^F, it could also signify the variation in any combination of dimensional parameters to achieve the same value of Λ^F.

Figure 4.1 shows the variation of the first two eigenvalues with Λ^F for an *undamped* wall with *no backing springs*. The upper and lower diagrams respectively depict its oscillatory, s_I, and growth/decay, s_R, parts. It is important to note here that some higher frequency modes were captured in the solution (as the closest 10 modes to $0 + 0i$ were found through the ARPACK routine); however it was chosen here to present just the lower-frequency modes that are the first to be destabilised by increasing the applied flow speed.

Four zones of responses are noted in Figure 4.1. These are the pre-divergence, divergence, divergence-recovery, and modal coalescence zones. At low flow speeds (pre-divergence) neutrally-stable oscillatory motion prevails. In the divergence range of flow speeds Mode 1 bifurcates to give non-oscillatory complex-conjugate

---

[1] These values of the non-dimensional parameter Λ^F, could correspond to a compliant wall in water of fluid density $\rho = 1000kg/m^3$ and wall properties of: $h = 0.0025m$, $\rho_w = 2600kg/m^3$, $L = 0.6m$, $E^* = 58.85 \times 10^9 Pa$, $B = 76.62Nm$. While the fluid velocity is varied from from $U_\infty = 0$ to $11.1m/s$

solutions while Mode 2 continues to be neutrally stable. Just after the divergence range of flow speed there exists a small range of flow speeds at which Mode 1 becomes oscillatory and total neutral stability exists once again. This range is termed the ‘divergence recovery’. Finally after divergence recovery, Modes 1 and 2 coalesce to give a pair of complex conjugate solutions with a non-zero oscillatory part. In this region, both Modes 1 and 2 are growing while undergoing oscillatory motion at the same time. The instability behaviour in this region is commonly known as flutter.

The panel motions (represented by the eigenmodes) in the four different zones of responses are illustrated in Figures 4.2 to 4.7. Figure 4.2 shows the first three eigenmodes when $\Lambda^F = 0$. In this case, the first and second mode shapes closely resemble the first and second mode shapes of the *in-vacuo* system. The frequency of oscillation is greatly reduced however due to the fluid inertia that acts on the plate and this is observed in the decreased value of the imaginary part when compared to the solution of the *in-vacuo* case. Interestingly, the third mode shape does not represent the *in-vacuo* third mode shape as much as Modes 1 and 2. This indicates that there are hydrodynamic effects aside from hydrodynamic inertia being introduced even in this case of zero flow-speed.

Figure 4.3 shows the first three wall mode shapes at a flow speed of $\Lambda^F = 44$. This is still in the pre-divergence zone, although only slightly before divergence onset occurs. The plots show that symmetry about the mid-point is broken in all three modes. Animations reveal that this gives the visual effect of wave travel superimposed upon the oscillatory standing-wave. As the amplitude decreases through the cycle upstream travel is perceived and the opposite is the case for increasing amplitude. This effect is very small however and indicates that the mode shape characteristics do not vary much throughout the pre-divergence range of flow speeds.

Figures 4.4 and 4.5 deal with the panel motion throughout the divergence range of flow speeds where as can be seen in Figure 4.1 the Mode 1 eigenvalue becomes purely real and through the bifurcation two real values exist for the eigenvalue. These two eigenvalues can be thought of as complex conjugate solutions to the Mode 1 although they are purely real. One of the real values corresponds to an amplifying solution, and the other corresponds to a decaying solution. Figure 4.4 shows the unstable amplifying solution for a series of increasing flow speeds when $\Lambda^F = 70.5, 138$ and 228, all lying within the divergence zone. Figure 4.5 shows the companion decaying solution for the same values of Λ^F. It is noted that the mode shape is strongly dependent upon flow speed, being very close to the fundamental mode exactly at the divergence-onset speed but increasingly evolving towards a Mode 2 shape as the flow speed is increased. The same is noted for the decaying mode, although its apparent distortion is in the opposite, upstream direction.

Figure 4.6 shows the first and second mode shapes at the mid-point of the divergence recovery zone when $\Lambda^F = 254$. The key feature here is the similarity of these first and second mode shapes prior to their coalescence. Both modes take on the form of the second *in-vacuo* mode, with a quasi-node at the midpoint of the panel.

The final zone of behaviour is that of modal-coalescence between the first and second modes. The first and second modes coalesce into an unstable mode that undergoes oscillatory growth. Animations reveal that the visual perception of this instability is principally a downstream-amplifying travelling wave. The unstable mode is shown in Figure 4.7 with the growth suppressed, while the third mode (which is still stable and oscillatory in behaviour) is shown in also. This third mode still resembles the *in-vacuo* third mode with quasi-nodes at the third-chords of the panel.

Suppressed hydrodynamic damping term

Figure 4.8 shows the results for the exact situations as presented in Figure 4.4 except that the hydrodynamic damping term (p_{U1}) has been suppressed in the calculation of the pressures along the wall.

The results show that without the hydrodynamic damping term there is no downstream deformation of the wall mode shape as was seen in Figure 4.4. Rather, the wall amplifies symmetrically with a similar most shape regardless of flow speed. Only the rate of growth is influences by the varying flow speed, however this could be expected as the flow speed has a linear relation to the hydrostatic pressure (p_{S1}).

Added structural damping

The effect of energy dissipation within the flexible plate is now investigated. The results from this section continue to use the parameters specified to generate the results of the preceding sub-section. However, we now use a non-zero damping ratio[2] of $\zeta = 6.13$.

Figure 4.9 is akin to Figure 4.1 and shows the variation of the system eigenvalues with the mean-flow speed. Comparing the results of the damped and undamped case, it can be seen that for the damped case there exists a low-speed zone where all modes undergo *damped* oscillatory behaviour. However, there exists a new zone of non-oscillatory damped behaviour of the first mode, resulting from the bifurcation of the first modes before the divergence onset flow speed is reached. It should be noted that the actual divergence-onset flow speed (noted by the point where the real part of the eigenvalues become greater than zero) is unchanged by the addition of damping. The mode shapes in this new zone of behaviour are plotted in Figure 4.10. As the first mode is a decaying non-oscillatory behaviour, it is evident that any transient motion in a real system could only feature oscillations of the second and higher modes.

Within the divergence zone of flow speeds, the plate behaviour is qualitatively the same as for the undamped plate except that the instability growth rate is reduced by the damping.

The second key difference between the damped and undamped plate dynamics occurs in the post divergence zone. Figure 4.9 shows that with increasing flow speed, the divergence instability merges into flutter instability. There is now

---

[2] This corresponds to 50% damping as defined in Lucey et al. [56], which also gives a damping coefficient value of $d = 7500 Ns/m^2$.

neither a divergence-recovery zone nor an explosive onset of flutter through exact modal coalescence. The disappearance of the divergence recovery zone is explored more closely in Figure 4.11 which displays the eigenvalues in this range of flow speed for different levels of *small amounts* of damping. It is clear that even for an incremental level of damping unstable behaviour exists for all flow speeds above that at which divergence first occurs.

4.2.2 Spring-backed flexible plate

For drag reducing properties to be effective the panel must have a lower flexural rigidity that is supplemented by backing-springs. These surfaces approximate that of a Kramer [45] surface which is based on the natural form of dolphin epidermis.

To illustrate the power of the new method for the determination of eigenvalues in FSI systems, some illustrative results for a flexible panel possessing a combination of flexural rigidity as well as foundation-spring stiffness. This ultimately means that hydro-elastic instability will be governed by higher order modes.

For the study of the eigenmodes of this system the flow-structure system properties will again be based on that of Lucey et al. [56]. In this study, the following dimensionless parameter for spring backed flexible plates is defined as,

$$\Lambda^I = \frac{3\pi^3 \rho {U_\infty}^2}{(3BK^3)^{\frac{1}{4}}} \tag{4.1}$$

The parameters used for the numerical experiments are the same as the settings defined in Lucey et al. [56], which correspond to a rubber-type compliant coating. As with the previous numerical experiments with the unsupported wall, all wall parameters are maintained except for the mean-flow velocity. In this case, the parameters of Lucey et al. [56] correspond to a non-dimensional[3] wall

---

[3] This non-dimensional parameter can correspond to a compliant wall with dimensional parameters of thickness of $h = 0.01m$, density of $\rho_w = 852kg/m^3$, Youngs modulus of $E^* = 53.31 \times 10^4 N/m^2$, flexural rigidity of $B = 4.44 \times 10^{-2} Nm$ and a length of $L = 0.6m$. The backing springs have a stiffness of $K = 3.68 \times 10^7 N/m^3$. The fluid is modelled as water with a density of $\rho = 1000kg/m^3$.

parameter of $\Lambda^I = 5.48 \times 10^{-1} U_\infty^2$. For the generation of eigenvalues and eigenmodes here a heavy structural damping, giving a damping ratio[4] of $\zeta = 0.56$, was applied to the wall.

Figure 4.12 displays the variation of the first 40 eigenmodes closest to the origin $(0 + 0i)$ for a variation in the non-dimensional parameter from $\Lambda^I = 0$ to 250. It can be seen, from the plot of the real part, that the lowest speed at which a growing response appears is at approximately $\Lambda^I = 130$ where one branch of s_R first crosses into the positive quadrant. This critical mode marks the edge of an envelope that is dense with unstable modes. Thus, the flexible wall's response throughout the flow-speed range is characterised by complex modes and combinations thereof that are very different from the *in-vacuo* sinusoidal modes.

Figure 4.13 shows the three modes closest to the null eigenvalue at pre-divergence where $\Lambda^I = 123$. Clearly, the motion of the flexible wall is dominated, particularly in the centre sections of the panel, by (upstream) travelling waves as opposed to oscillatory standing waves.

Figure 4.14, shows the most unstable mode for three flow speeds slightly after divergence onset has occurred, corresponding to $\Lambda^I = 130, 136$ and 140 respectively from top to bottom. At almost precisely divergence onset when $\Lambda^I = 130$, the motion of the wall is dominated by growing (downstream) travelling waves in the centre section while the growth is stationary near the panel edges. At slightly higher flow speeds the growing waves become more complicated as other modes begin to coalesce into the instability.

4.3 Investigation with the Galerkin Method

Using the Galerkin method outlined in Section 3.3.2 a basis for comparison with the above results could be achieved. A presentation of some results obtained through the Galerkin method and their comparison with results using the ARPACK method of Section 3.3.1 follows here.

---

[4] In this case, a damping ratio of $\zeta = 0.56$ corresponds to a damping coefficient value of $d = 20000 Ns/m^3$

4.3.1 Simply supported flexible plate

Figure 4.15 shows a comparison of the eigenvalues obtained using the ARPACK routine and the Galerkin method. In this case the Galerkin method used the first three *in-vacuo* modes for the required orthogonal mode set.

Figure 4.15 shows that, for the case of a simply supported flexible plate, the use of only three *in-vacuo* modes still allows an accurate determination of the divergence onset. However at higher flow speeds of approximately $\Lambda^F = 800$ or more, the Galerkin method fails to accurately determine post-divergence dynamics if an insufficient number of orthogonal modes are chosen.

4.3.2 Spring-backed Flexible plate

Figure 4.16 shows the results of using the Galerkin method with $N = 30$ to generate the same results as shown in Figure 4.12.

Comparing Figure 4.16 and 4.12, both methods give the same result for the divergence onset flow speed which in this case occurs at approximately $\Lambda^I = 130$. In the pre-divergence range of flow speeds the lower mode numbers have similar eigenvalue loci. However, even in the pre-divergence range of flow speeds, the Galerkin method fails to accurately capture the loci of the higher mode numbers. Around the divergence and post-divergence range of flow speeds, the eigenvalue loci for almost all modes except the most unstable show increased variance to the results obtained from the ARPACK solution. The adoption of more orthogonal modes would be required to resolve these eigenvalues at the higher flow speeds. None the less, the eigenvalue locus for the most unstable mode remains similar between both methods.

4.4 Transience leading to steady-state non-linear wall dynamics

We now turn our attention to the use of the non-linear potential flow model developed in Section 3.2. Of particular interest is the nature of the transient disturbance growth and the final steady state of the non-linear system. The growth of the non-linear wall and fluid model throughout transience and onto a relatively steady-state is investigated for three types of initial conditions in order to demonstrate that the final non-linear steady state is independent of the initial linear disturbance. The initial conditions adopted are:

a) a small wave-length sinusoidal disturbance at the panel centre;

b) a longer wave-length sinusoidal disturbance at the panel centre and;

c) a sinusoidal wavy disturbance that spans the entire panel (as used in Lucey et al. [56])

In all cases, a spring-backed flexible panel like that of Lucey et al. [56] is used, with a damping ratio of $\zeta = 0.12$ and the non-dimensional[5] stiffness parameter $\Lambda^I = 170$. This gives a similar parameter set as was used in Section 4.2.2, but with a flow speed of approximately $22.5 m/s$ and different damping and backing spring stiffness.

The sinusoidal disturbance at the panel centre is represented by a piecewise continuous function in order to smooth high curvatures at the edges of the disturbed section. The shape of the disturbance is based of the work of Cafolla [12].

---

[5] These wall properties correspond to: a thickness of $h = 0.01m$, density $\rho_w = 852kg/m^3$, Youngs modulus of $E^* = 53.31 \times 10^4 Pa$, flexural rigidity of $B = 4.44 \times 10^{-2} Nm$ and a length of $L = 0.6m$. The backing springs have a stiffness of $K = 18.4 \times 10^6 N/m^2$ and the 50% structural damping corresponds to a damping coefficient of $d = 3000 Ns/m^2$. The fluid is modelled as water with a density of $\rho = 1000kg/m^3$

This piecewise function is described as

$$\eta = \begin{cases} \left(\frac{A}{2}\right)\cos\left[\frac{(x^*)2\pi}{\left(\frac{3L_D}{4}\right)}\right] - \frac{A}{2} & \text{if } 0 \leq x^* \leq \frac{L_D}{4}, \\ \left(\frac{A}{2}\right)\cos\left[\frac{(x^*)2\pi}{\left(\frac{3L_D}{4}\right)}\right] - \left(\frac{A}{2}\right)\cos\left[\frac{\left(x^* - \frac{L_D}{4}\right)2\pi}{\left(\frac{3L_D}{4}\right)}\right] & \text{if } \frac{L_d}{4} \leq x^* \leq \frac{3L_D}{4}, \\ \left(\frac{-A}{2}\right)\cos\left[\frac{\left(x^* - \frac{L_D}{4}\right)2\pi}{\left(\frac{3L_D}{4}\right)}\right] + \frac{A}{2} & \text{if } \frac{3L_D}{4} \leq x^* \leq L_D, \\ 0 & \text{otherwise.} \end{cases} \tag{4.2}$$

where η is the displacement of the wall in the normal direction, A is the amplitude of the disturbance, and L_D is the disturbance length. x^* is the distance along the x-coordinate from the starting point of the disturbance.

Figures 4.17, 4.18 and 4.19 show the growth of the small wave-length sinusoidal disturbance at the panel centre. The wavelength for this small sinusoidal disturbance was selected to be approximately similar to the critical divergence wavelength for this wall from Babenko [6]. The initial development of the disturbance is marked by a rapid growth in both upstream and downstream directions. The disturbance rapidly grows to cover the entire span of the wall. After this period of rapid initial growth, the sinusoidal disturbance continues to grow in amplitude while travelling downstream. At longer times, the growth as well as the travelling speed of the wave peaks slows as non-linear effects (a result of the induced tension in the wall) become significant. At this point, the wave peaks become sharper and a complex interference interaction occurs between the wall waves. The final 'steady state' response is characterised by several dominant slowly-moving wave peaks along the panel, the spacing between these wave packets becomes more random as the complex interference between the waves continues.

Figures 4.20, 4.21 and 4.22 show the growth of the longer wave-length initial sinusoidal disturbance. In this case, the initial sinusoidal disturbance wave-length is four times the wavelength of the initial disturbance used in Figures 4.17-4.19. The initial disturbance is actually observed to decay slightly throughout the early stages of transience. During this decay of the initial disturbance, wave packets of shorter wavelength can be seen to be propagating out of the initial disturbance in both the upsteam and downstream directions. These emerging wave packets grow rapidly (as in the previous case) to fill the entire span of the finite panel, while the initial disturbance wavelength decays due to the structural damping. After this point, the development of the wave into long-time response is similar to that of the short-wavelength disturbance of the previous case in Figures 4.21 and 4.22.

Figures 4.23, 4.24 and 4.25 show the growth from an initial state where the entire span of the wall is perturbed to the 20th mode shape. As the critical divergence wavelength for this particular panel is close to the wavelength of the 20th mode, the development of the wall is similar to that of the short wave-length initial disturbance once it has grown to span the entire length of the wall.

4.5 Discussion

4.5.1 Linear results

Figure 4.1 presents the results for the development of the first two eigenvalues as the flow speed is increased. It was pointed out that there are four regions of responses, these being the: ‘pre-divergence’, ‘divergence’, ‘divergence recovery’ and ‘modal coalescence flutter’. The pre-divergence and divergence recovery zones consist of total neutral stability and oscillatory behaviour across all modes. Divergence involves bifurcation and non-oscillatory growth of Mode 1 while Mode 2 (and higher modes) continue oscillatory behaviour. The flutter region is associated with Modes 1 and 2 coalescing and growing the wall motion becomes unstable, growing in amplitude while also oscillating. This sequence of changes is well known and have been documented by Weaver and Unny [83], Carpenter and Garrad [18] and Lucey et al. [56]. However, it is emphasised that the present results are almost exact and have not relied upon an arbitrarily selected number of modes for the Galerkin solution. In this regard, it can be confidently stated that these are the actual system solutions.

The results from the trials with the Galerkin method indicate that the two lowest-frequency system eigenvalues (that are observed in Figure 4.1) can be reproduced accurately using the first three *in-vacuo* modes in the Galerkin solver. While this gives confidence in the results obtained for the case of a simple elastic plate, caution must be exercised when dealing with a spring-backed elastic plate. In this case the disturbance wave-length, particularly near divergence onset, is much higher than the simple plate. This can be seen in Figure 4.13. Correspondingly, the number of *in-vacuo* modes that must be selected must be higher also.

Figure 4.2 shows the first three eigenmodes when $\Lambda^F = 0$. As was observed the first and second mode shapes are in close agreement with the *in-vacuo* mode shapes, but it was noted that the third mode differs from the corresponding *in-vacuo* shape quite markedly. This difference indicates that even for the case of 'hydro-static' loading ($U_\infty = 0$) there must be a streamwise fluid motion that results in the influence along the wall. This could be expected as the influence of tangential velocity at each panel is *not* independent of the other panels on the wall. In reality, this would be observed by lateral fluid motion away from the peak as a part of the wall is moving upwards and vice-versa for the 'troughs'. Although small, this effect becomes more noticeable at higher modes because the 'peaks' and 'troughs' become sharper, resulting in the more distorted mode shapes that are seen at higher modes.

The results of Figure 4.5 illustrate the first mode shape decaying throughout a range of flow speeds within the divergence zone. This seems to present a paradox. As divergence is an absolute instability then it seems like a decaying solution is meaningless. Clearly, in an unbounded system then it is the amplifying mode that will dominate, causing the wall amplitude to grow indefinitely. However, the decaying solution still has meaning in the case where the maximum wall amplitude is bounded and then the growing instability is reflected back down into a decaying state. This behaviour is observed and documented in Lucey et al. [56]

and also in the results for the non-linear simply supported plate in this thesis. This illustrates the power of the eigenanalysis solution. In the eigenanalysis every possible solution is considered and under the correct conditions then these solutions can be observed.

In Figure 4.1 a third zone where there was a small region of neutral stability at flow speeds higher than the divergence flowspeed was identified. In separate numerical simulations, setting the flow speed within this range and starting from an initial condition the wall was observed to initially grow and finally settle into a neutrally stable state. Although these theoretical results indicate that this band of neutral stability might exist, in reality this is not a possibility. This is explained through examination of Figure 4.11. The results in Figure 4.11 show that even when a slight amount of structural damping is added to the wall, the balance is destroyed and the first and second mode do not perfectly coalesce. Perhaps more importantly, it can be seen that with the addition of small amounts of damping the real part does not return to zero. This indicates that with even a small amount of structural damping (that will *always* exist in a real system) neutral stability of the system will not exist. Rather, the system will experience growing oscillatory instability. Combined with other factors that would be present in real systems such as external forcing due to background and/or turbulent noise, there seems little possibility that this neutral stability zone could ever be observed experimentally. It is likely that an experimental observation of this range would appear as a zone of *reduced instability*, where growth in the energy of the wall slows, but does not neutralise.

The deterioration of the eigenvalue plots near the extremities of Figure 4.12 is due to the ARPACK program selecting the nearest forty eigenvalues. When there is very little difference between these values (as there is at the extremities) then the results will tend to jump between various eigenvalues.

The results shown in Figure 4.12 also indicate that the fundamental *in-vacuo* mode is not always the most unstable wall mode at divergence onset. Furthermore, it can be seen how post-divergence wall motion is a complex interaction of the various modes and could be interpreted as a type of modal-coalescence. The intricate lattice shape that is seen in Figure 4.12 is a result of this same effect, the cancellation and re-introduction of the eigenvalues of various modes as they approach and depart from the origin.

In the study of hydroelastic instabilities there has been some debate over the exact nature of divergence instability. Early work by Paidoussis and Guo [60] using Galerkin-type analytical methods identified divergence to be a stationary growing wave. However, travelling-wave analysis on infinite walls by Carpenter and Garrad [17] found divergence to be a downstream-travelling wave. The later work of Lucey and Carpenter [55] using numerical simulation also identified divergence to be a slow-downstream travelling wave. The results obtained from the linear eigenanalysis indicates the reason for this discrepancy. It was seen in Figures 4.4 and 4.5 that the critical mode in a divergence instability has a stationary shape. In this regard, the divergence mode is a stationary growing wave. However, the mode shape is distorted in the downstream direction for the growing wave, and in the upstream direction for the attenuating wave.

Another explanation for the above paradox lies in the finiteness of the panel, hence this is related to panel edge effects. In all cases of a wave that is growing under divergence instability, the wave will have a tendency to travel downstream at a rate that is proportional to its rate of growth. The reason for this is because the hydrodynamic damping term of the unsteady pressure (p_U1) is dependent on the vertical velocity of the wall, and creates a pressure that is 90°out of phase to the wave shape. For this reason, in the results of Lucey et al. [56] as well as the results for the transient response of the wall obtained in this work, the transient wave for a high mode-number is observed to be a downstream travelling wave. For a rigid flexible plate, this downstream tendency is quickly hindered by the downstream edge of the finite panel. The wave can not travel downstream due to the finiteness of the wall, and cannot oscillate due to the nature of the divergence instability. Therefore, the divergence instability on a simple flexible plate takes the form of a stationary growing wave. However, transience will rightly be observed as a downstream travelling wave, as the wave will grow from its initial position until it is hindered by the trailing edge. In the case of an infinite wall, there is no downstream edge to the growing waves to encounter and waves will continue to grow downstream unhindered. In this regard, infinite walls can be considered to always be in a state of transience, as a wave on an infinite wall does not have an edge to encounter. This explains the apparent discrepancy between the theoretical results that indicate that infinite walls having a downstream travelling divergence wave and finite walls having a stationary growing divergence wave. Both theoretical results are correct in their context. However, obviously in any practical application, a compliant wall will always be finite.

A striking feature of the divergence mode shapes in Figure 4.4 is that the first mode appears to be ‘transforming’ into the second mode as the flow speed is increased, to the point where in Figure 4.6 the first and second mode shapes are almost identical. If there is no structural damping, these modes will coalesce and become identical at slightly higher flow speeds. This behaviour can also be explained using the fact mentioned above that growing divergence waves have a tendency to travel downstream. In this case, in the first half of the divergence zone, as the flow speed is increased, the diverging first mode will have a greater real part indicating that it is growing faster with increased flow speed. This is not surprising and could be expected through consideration of the mechanisms involved. However, associated with this increased growth is an increased tendency for the hydrodynamic damping term to force the wave downstream. This forcing of the wave downstream (by the hydrodynamic damping term) is hindered by the downstream edge. None the less, with higher flow speeds the peak of the wave will be pushed closer to the downstream edge as the forcing from the hydrodynamic damping succeeds over the resistance by flexural rigidity. As the peak is pushed closer to the trailing edge, a trough will naturally begin to fill at the upstream edge as a natural minimum energy state is sought. This behaviour begins to cause the first mode to become more similar (in shape) to the second mode. If the flow speed is increased further, a point will be reached where the first mode shape no longer exists as a possible solution due to this mechanism. At this point, the first mode shape 'locks in' to the second mode shape, and as the second mode has not yet become unstable, the solution gives a region of neutrally stability.

The importance of the hydrodynamic damping term and its competition with the panel edge to change the mode shape is indicated in Figure 4.8. In this figure the hydrodynamic damping term has been eliminated from the calculation of the forces. The fundamental mode shape no longer deforms throughout the divergence range of flow speeds. Instead the mode grows statically with no upstream nor downstream tendency. This result, along with the considerations above indicate the importance of the hydrodynamic damping term, and its interaction with panel edges, on the dynamics of a finite compliant wall. Removal of either of these competing factors drastically changes the observed dynamics. For this reason, studies on infinite walls (which have no edge to compete with the downstream hydrodynamic damping forcing) can be expected to yield different and sometimes irrelevant results when compared to studies of finite wall dynamics.

It is interesting to note that in the case of a wall with added structural damping, as in Figure 4.9, the first and second modes do not coalesce exactly. This behaviour can also be described through the mechanisms mentioned above where the first mode 'transforms' into the second mode through the forcing of the hydrodynamic damping term. In the case of a wall with added structural damping, the growth rate of the divergence instability will be slowed as a result of the added damping. As mentioned above, it is the rate of growth of the wall brings about the mechanisms by which the hydrodynamic damping term forces the wave downstream in ultimately, in the case of a finite panel, into the second mode shape. With added structural damping, this mechanism will be retarded. Hence one could expect that with sufficient damping, downstream forcing will be retarded sufficiently that the first mode will not transform to the second mode.

4.5.2 Non-linear transient results

Figures 4.17 to 4.25 show the development of the non-linear wall response from some initially linear disturbance. The long-time response of the ideal flow model never achieved a perfectly steady-state, although a clear final state was reached using the non-linear wall model. A steady-state was not achieved because the ideal flow model did not account for flow separation that would naturally occur over the sharp crests of the large-amplitude waves that occurred at later times in the simulation. Instead, the ideal flow model allows flow to remain attached over large amplitude and high curvatures of the wall. This attachment gives high values of hydrodynamic pressure which work to further deform the wall into sharper peaks which further increase the hydrodynamic pressures and so the process continues. In a real situation, this deformation would continue until a limit where flow separation would occur and reduce the hydrodynamic pressure hence stopping any further growth of the wave peak. None the less, the results from the ideal flow model are valid to the point where amplitudes and curvatures have not become unreasonably large. This point is referred to as the ‘final state’.

The results from the non-linear transient simulations show that a similar final state was achieved by all three linear initial conditions; the small wavelength isolated disturbance, the long wavelength isolated disturbance, and the small wavelength disturbance across the entire wall. From this it is logical to deduce that in a real system, where separation would prevent further wave peak growth and curvature, the system will achieve the same steady-state condition. As in the study of Lucey et al. [56], the long-time response of the non-linear system is marked by sharp wave peaks and separated by long flat troughs. The length between the troughs becomes more randomly distributed as non-linear effects play a greater role at longer times. The exact distribution of sharp peaks at the final state were not identical due to some dependence upon the initial conditions and the resulting development through transience. However, the overall qualitative characteristics of the final state were independent of the initial conditions.

While the final state was independent of the initial conditions, the time required to reach this final state was dependent upon the initial conditions. An explanation for this can be seen through comparison of Figures 4.17 and 4.20. In this case the disturbance in Figure 4.17 shows more rapid growth because the initial disturbance is of similar magnitude wavelength as the most unstable wavelength. The initial disturbance in Figure 4.20 experiences an initial decaying because the disturbance wavelength is initially stable. It then takes some time before the unstable wavelengths similar to those seen in Figure 4.17 begin to emerge.

Measurement of the wave speeds during the linear and non-linear range of growth found that the (downstream) travelling wave speed was much higher during the linear range of growth than the non-linear. During the linear range of growth of the wave packet shown in Figure 4.17, the wave speed was measured to be downstream at approximately $150.3 m^*/s^*$ units of non-dimensional velocity[6]. Throughout the non-linear range the wave speed varied amongst wave peaks but was found to lie mostly between the values of 17.1 and $36.9 m^*/s^*$. This could be anticipated through consideration of the discussion above regarding wave-travel and its relation to growth rate through the hydrodynamic damping term. It was shown above that the hydrodynamic damping term (of the pressure determination) is responsible for the downstream travelling tendency of a growing wave. This means that, in the linear range, downstream wave travel speed is directly proportional to growth rate. This correlation holds into the non-linear range of growth where the induced tension in the wall slows the growth rate and hence slows the downstream travelling tendency of the waves. Conversely, the growth rate of a wave will be highest during the linear range of motion when the wall is for the most part unhindered by the induced tension, thereby giving higher growth rates and ultimately higher wave speeds.

Figure 4.17 shows the growth of an initial linear sinusoidal disturbance which is marked by a rapid growth in both upstream and downstream directions until the disturbance rapidly grows to cover the entire span of the wall. Lucey [54] notes

---

[6] m^*/s^* is the non-dimensional velocity. m^* corresponds to the non-dimensional length (x/L) and s^* corresponds to units of non-dimensional time defined in Equation 3.28c

that two different types of wave must be present to account for this upstream and downstream growth. All wave-like disturbances on the wall are of a downstream-travelling nature, but one with upstream energy transfer and the other with a downstream energy transfer.

4.6 Conclusion

The new method for direct determination of the eigenmodes of finite flow structure systems, developed in 3.3.1, has been applied to the classical problem of a flexible panel help at both its end with hinged connections interacting with a uniform flow. The exact eigenmodes extracted suggest that for realistic panels, modal coalescence flutter is a continuous extension of the divergence instability that precedes it at lower flow speeds.

By using this method to investigate both development of eigenvalues and eigenmodes throughout a range of flow speeds, a physical explanation was achieved to explain the discrepancy between divergence being theoretically determined as a travelling wave on infinite panels, and static waves on a finite panel. The reason for this discrepancy lies in the competing forces of the downstream-forcing hydrodynamic damping and resistance of this downstream tendency by the trailing edge of the panel through the flexural rigidity.

It was shown in Figure 4.15 that if a sufficient number of orthogonal modes are used then the Galerkin method accurately gives the same results. However, it is emphasised that the eigenanalysis presented in Section 3.3.1 could be equally easily applied to find the eigenmodes of flow-structure systems containing, for example, any type of surface-based homogeneous flexible wall, complex and/or free-end conditions, spatially varying wall properties and, indeed, nearly any form of localised inhomogeneity. Perhaps the greatest potential for this method of eigenanalysis is in the extraction of eigenmodes from FSI systems involving more complex fluid models, such as linear boundary layer theory. In theory, the extraction of the eigenvalues from *any* linear system, or combination of linear systems should be equally straightforward.

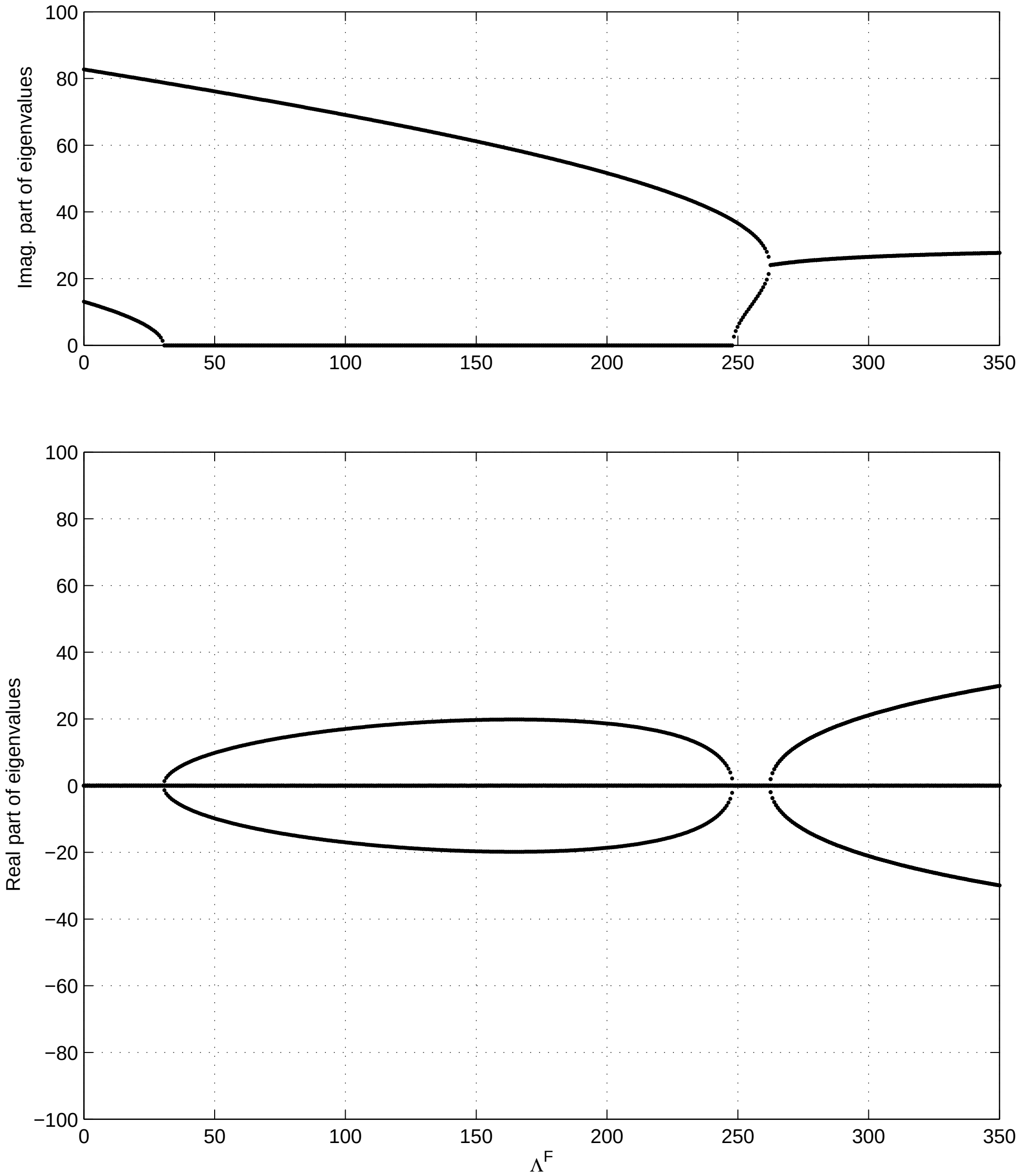

Figure 4.1: Imaginary (top) and Real (bottom) parts of the 10 eigenvalues nearest to $0 + 0i$. The variation in non-dimensional parameter Λ^F could correspond to variation in the mean flow velocity from $U_\infty = 0$ to $11.1m/s$ in $0.025m/s$ increments. For a compliant wall with *no wall damping* and *no backing springs* and properties: $h = 0.0025m$, $\rho_w = 2600kg/m^3$, $E^* = 58.85 \times 10^9 Pa$, $B = 76.62N.m$

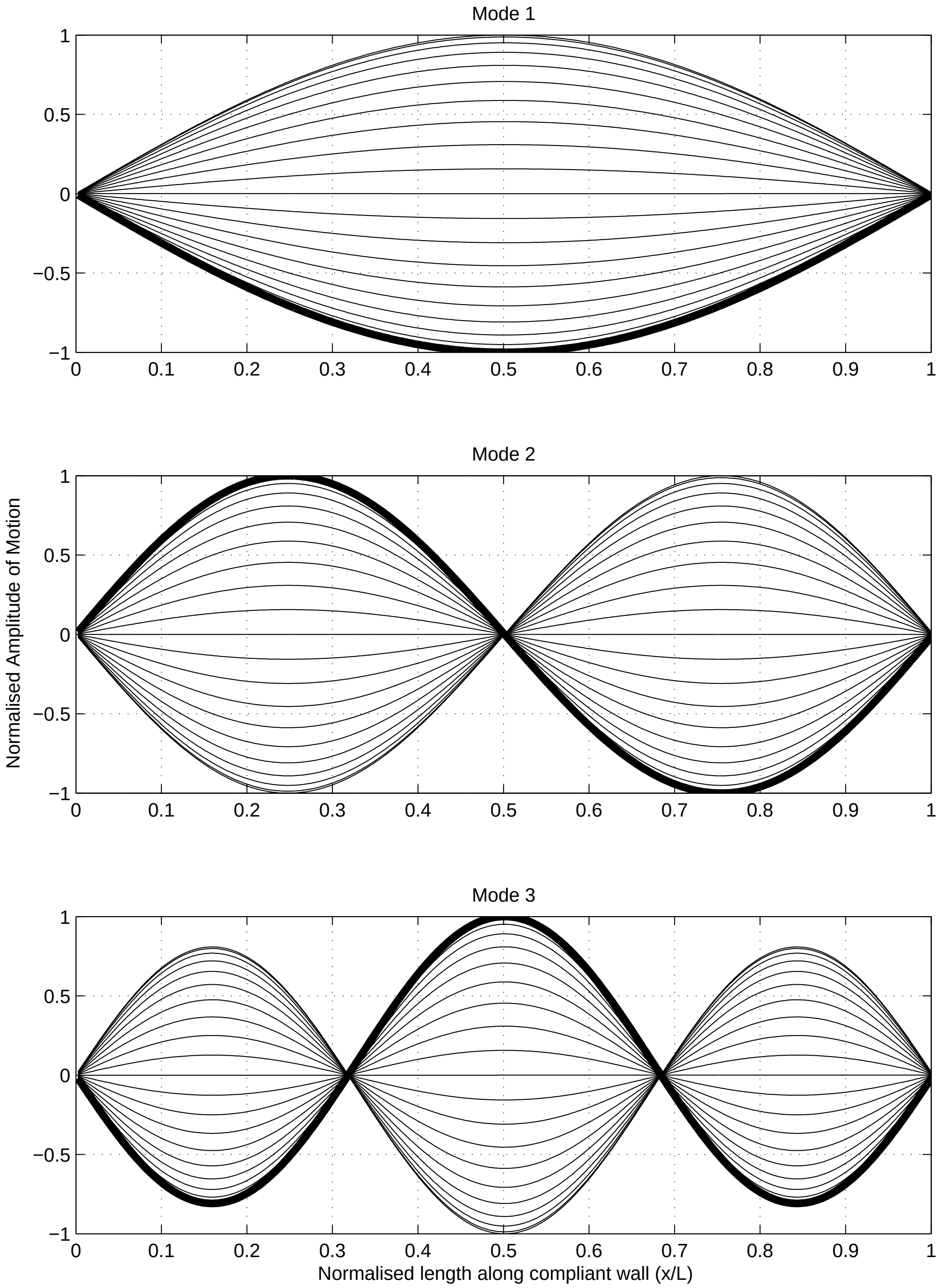

Figure 4.2: Wall motion for the the first second and third eigenmode when $\Lambda^F = 0$ (pre-divergence). Wall properties as in Figure 4.1

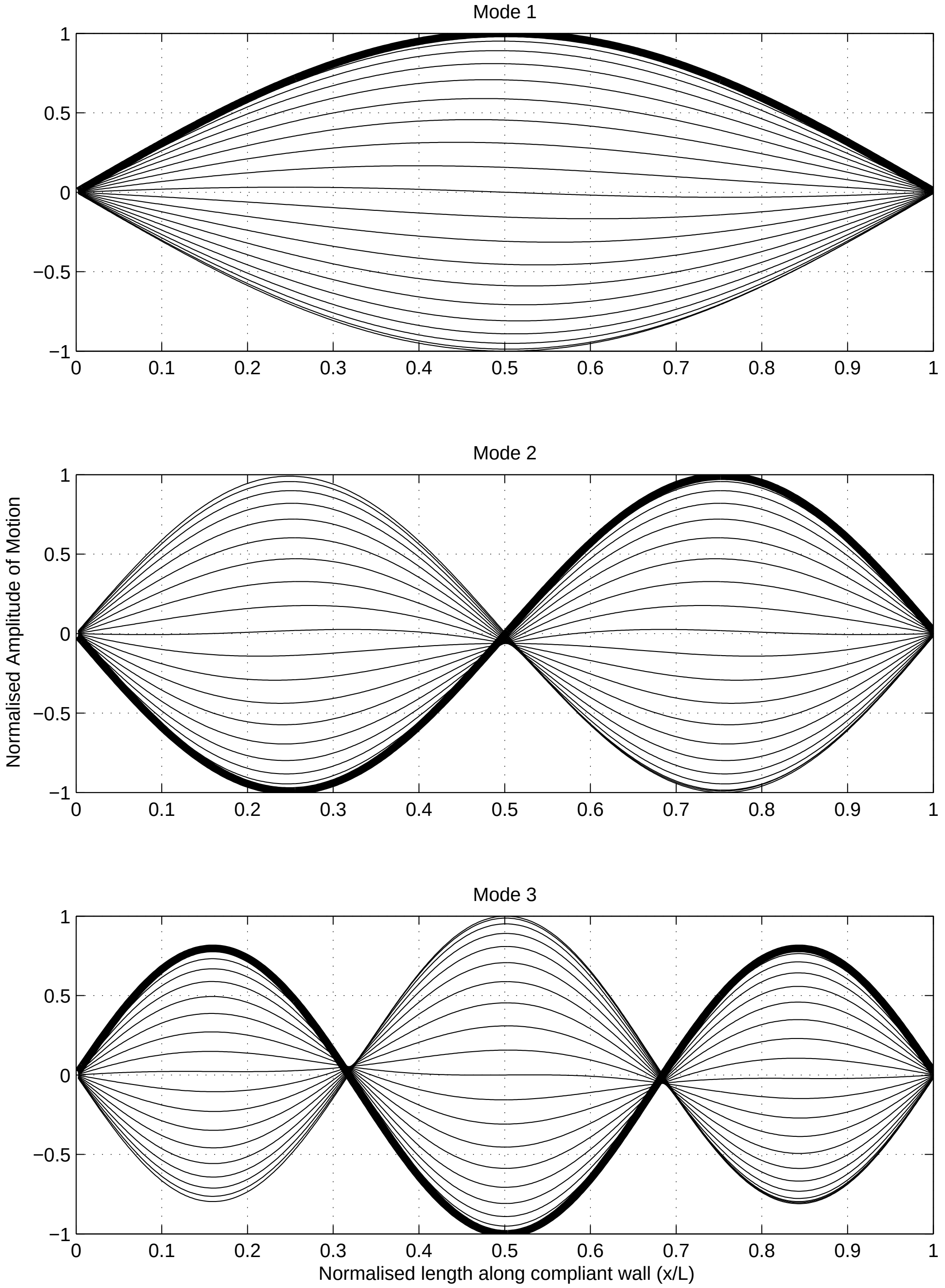

Figure 4.3: Wall motion for the the first second and third eigenmode when $\Lambda^F = 17.6$ (pre-divergence). Wall properties as in Figure 4.1. The bold line indicates the final position of the wall.

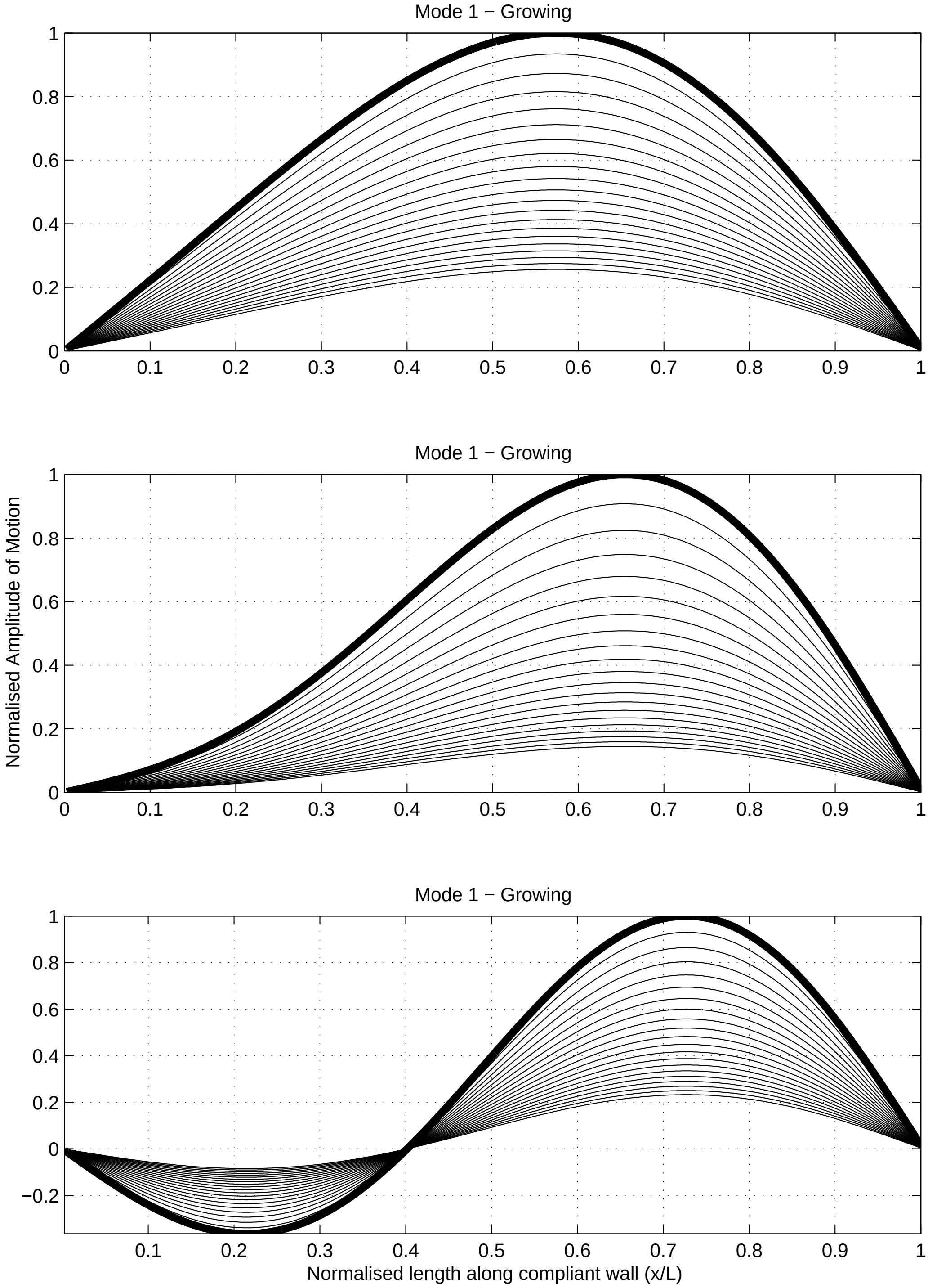

Figure 4.4: Plot of the most unstable mode growth at various flow speeds post-divergence onset when $\Lambda^F = 70.5, 138$ and 228 from top to bottom respectively. No structural damping, wall properties as in Figure 4.1. The bold line indicates the final position of the wall.

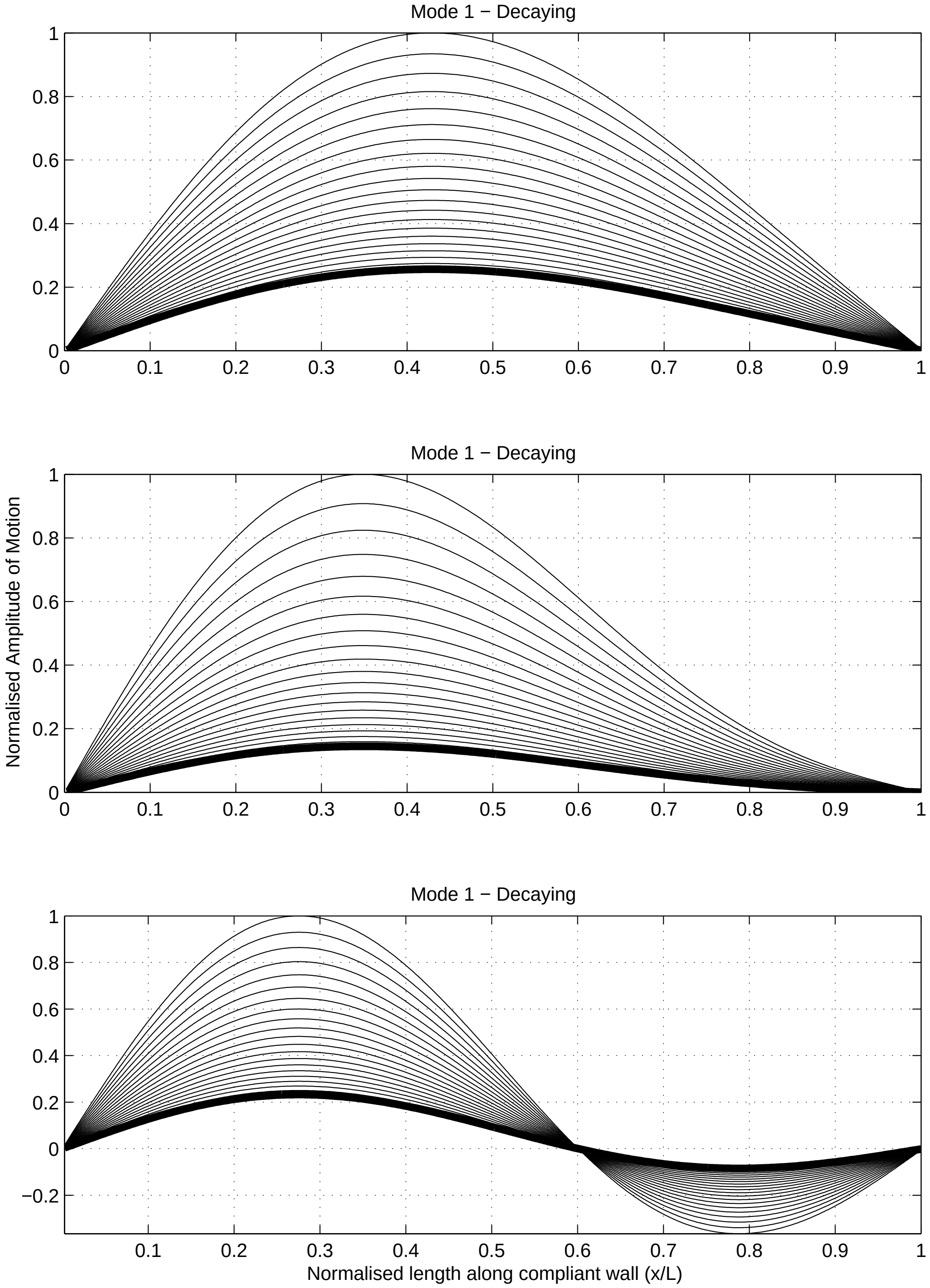

Figure 4.5: Shows the corresponding decaying modes for the exact same parameters described in Figure 4.4. The bold line indicates the final position of the wall.

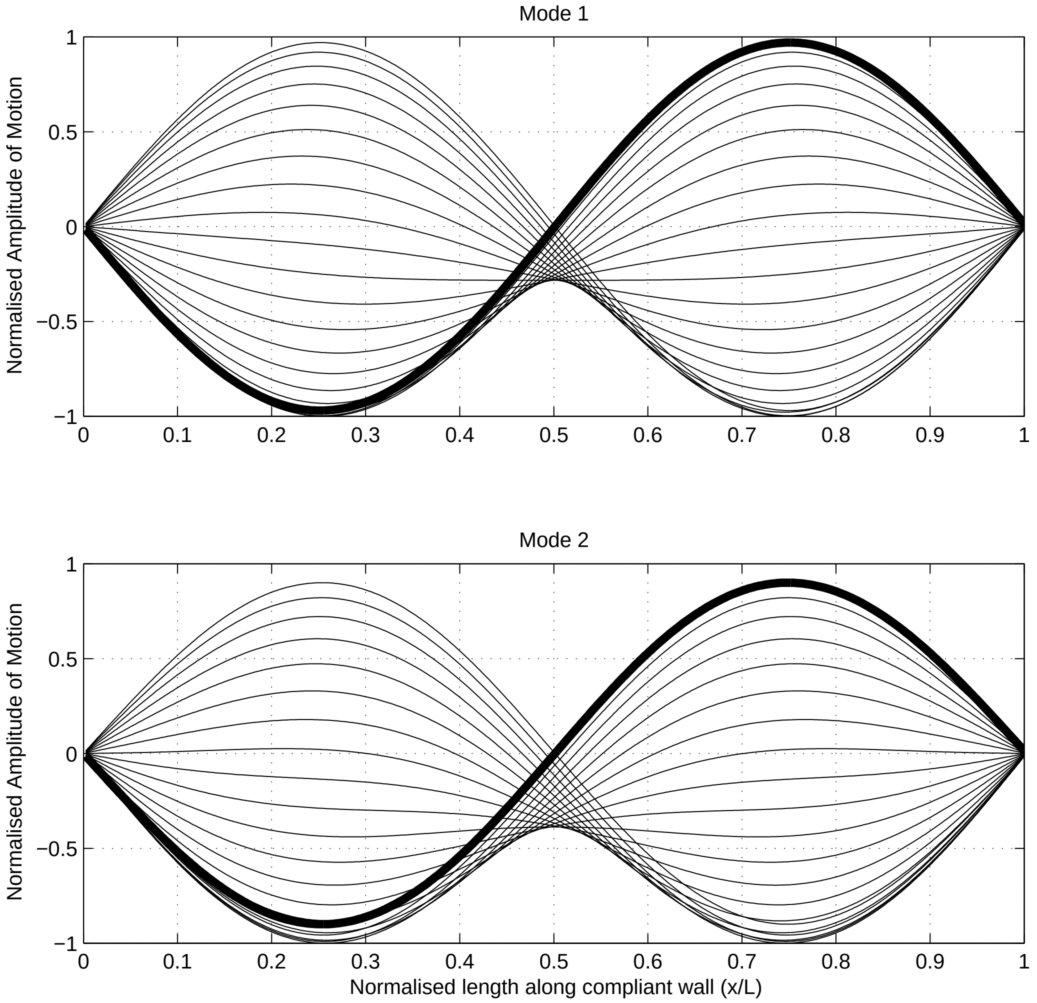

Figure 4.6: Wall motion for the the first and second eigenmode when $\Lambda^F = 254$ (divergence recovery zone). Wall properties as in Figure 4.1. The bold line indicates the final position of the wall.

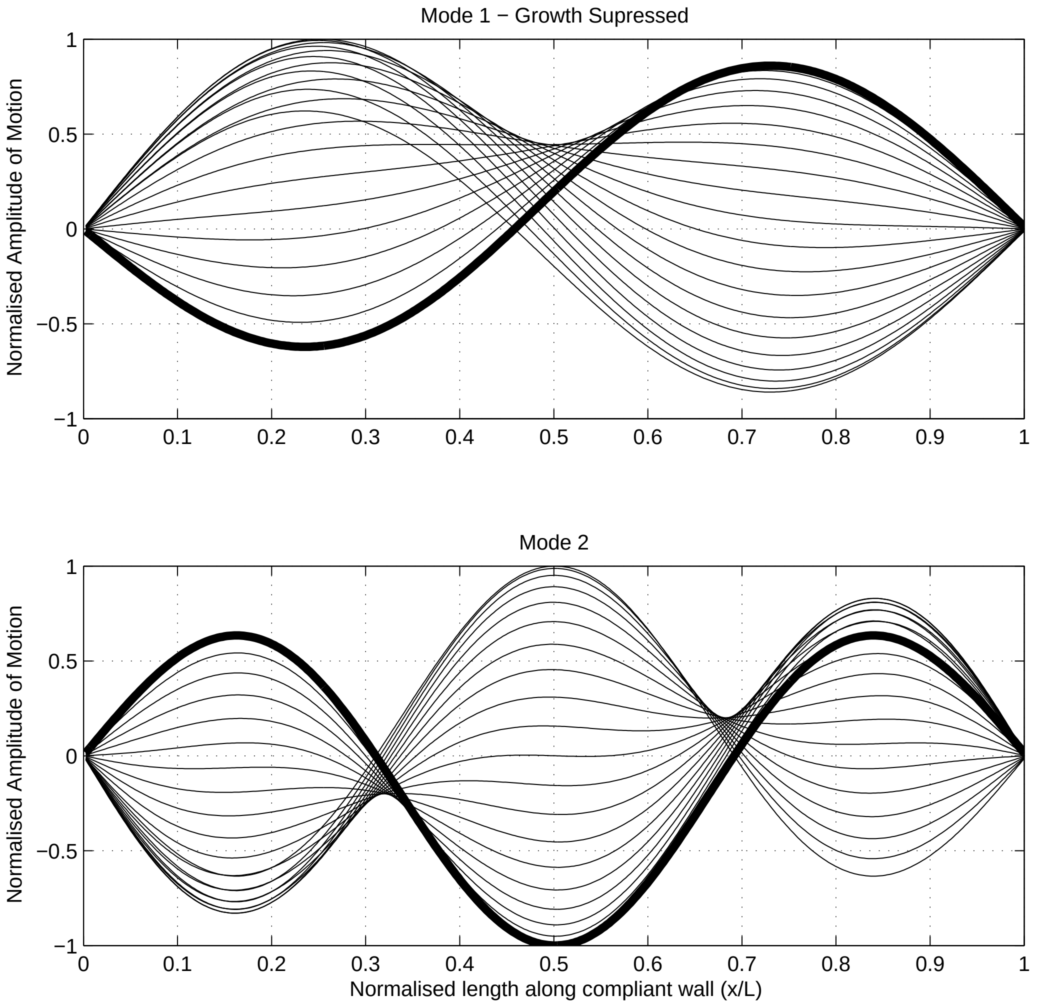

Figure 4.7: Wall motion for the the first and second eigenmode when $\Lambda^F = 281$ (Post divergence recovery). Note that wall growth has been suppressed in these figures. Wall properties as in Figure 4.1. The bold line indicates the final position of the wall.

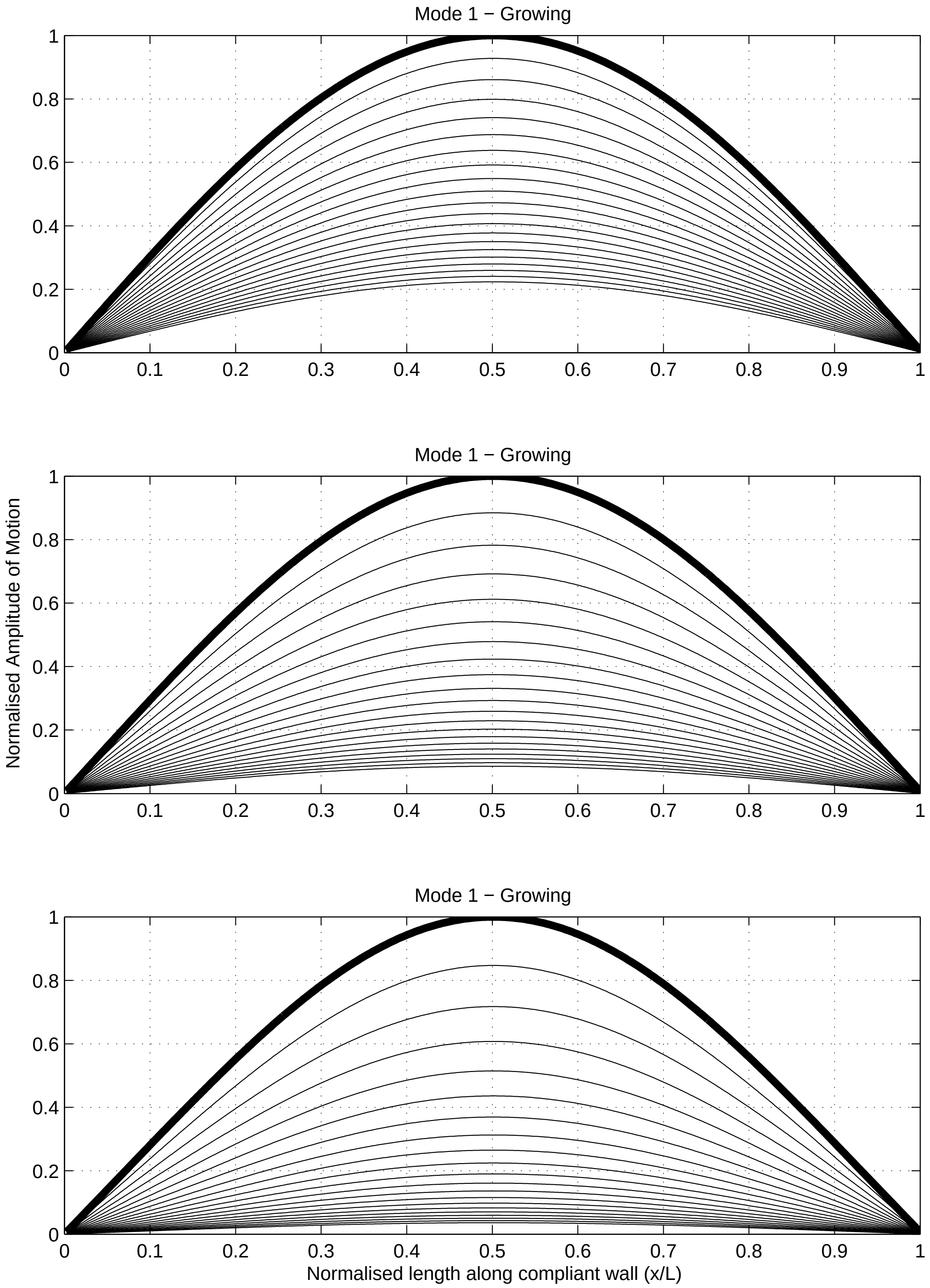

Figure 4.8: Plot of the most unstable mode growth at various flow speeds post-divergence, same as Figure 4.4, but with the hydrodynamic damping term suppressed. The bold line indicates the final position of the wall.

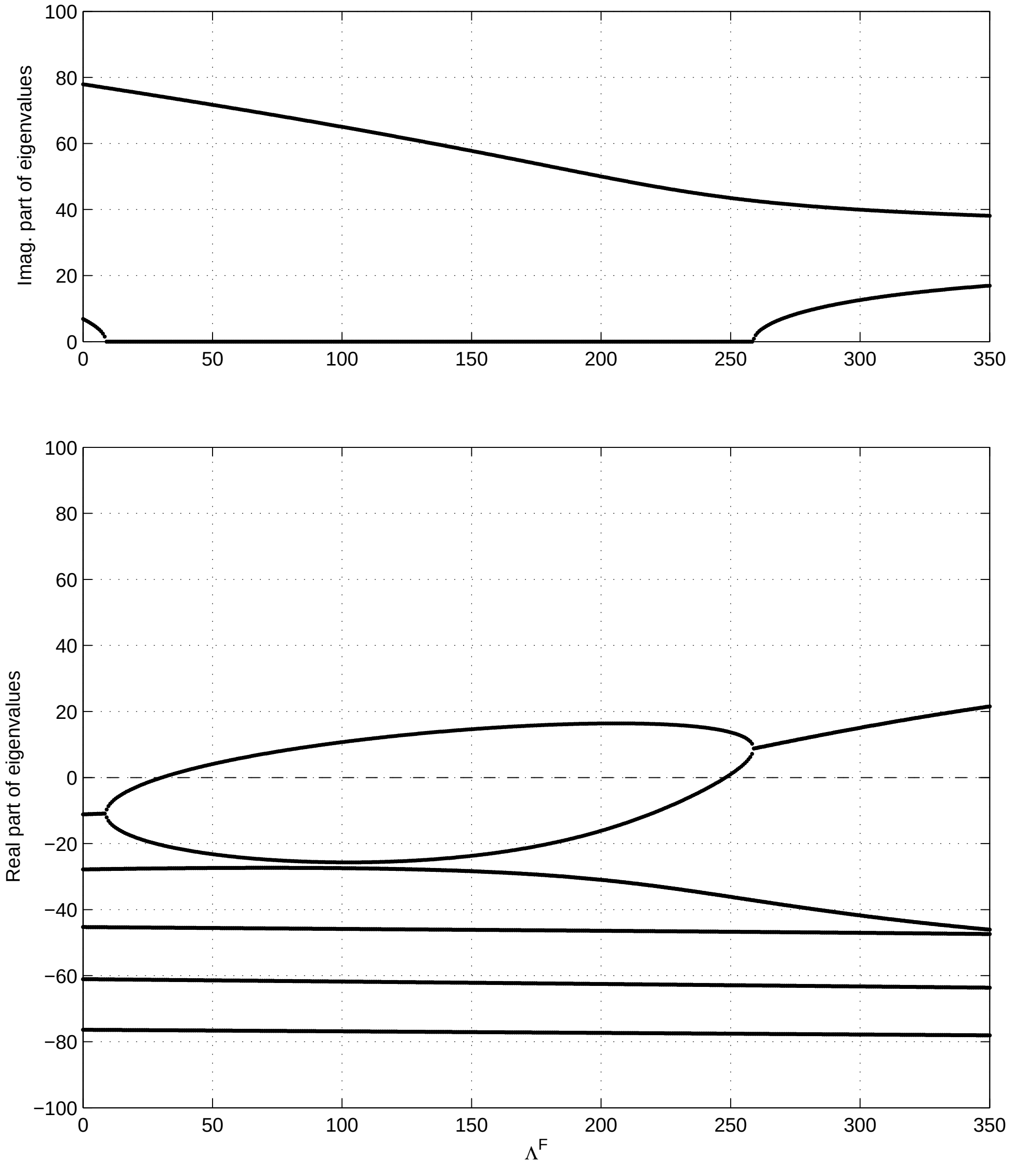

Figure 4.9: Imaginary (top) and Real (bottom) parts of the 10 eigenvalues nearest to $0 + 0i$ for a compliant wall with same properties as Figure 4.1 except that structural damping is added to give a damping ratio of $\zeta = 6.13$

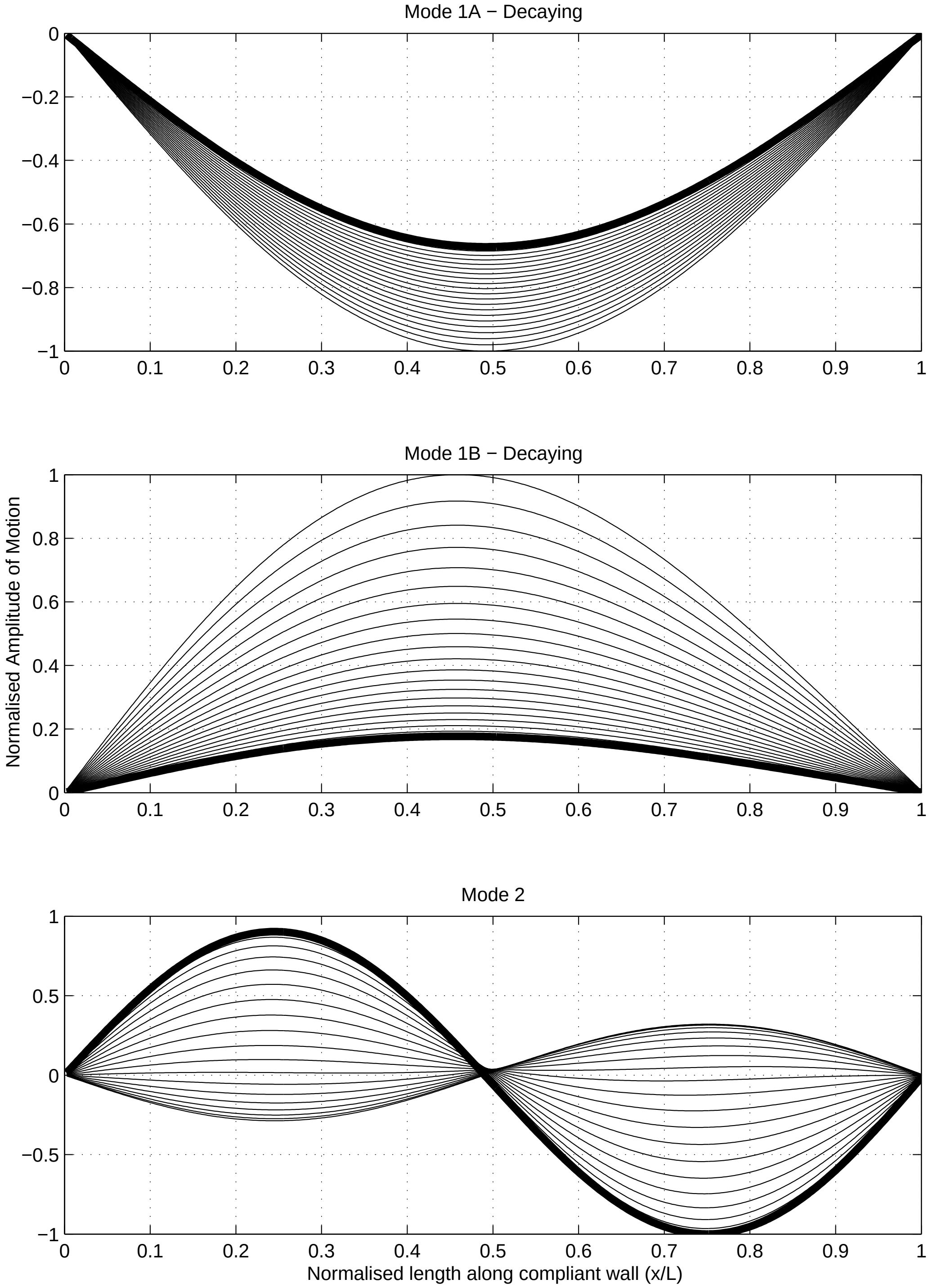

Figure 4.10: Wall motion for the the first second and third eigenmode when $\Lambda^F = 17.6$ (pre-divergence). Wall properties as in Figure 4.9. The bold line indicates the final position of the wall.

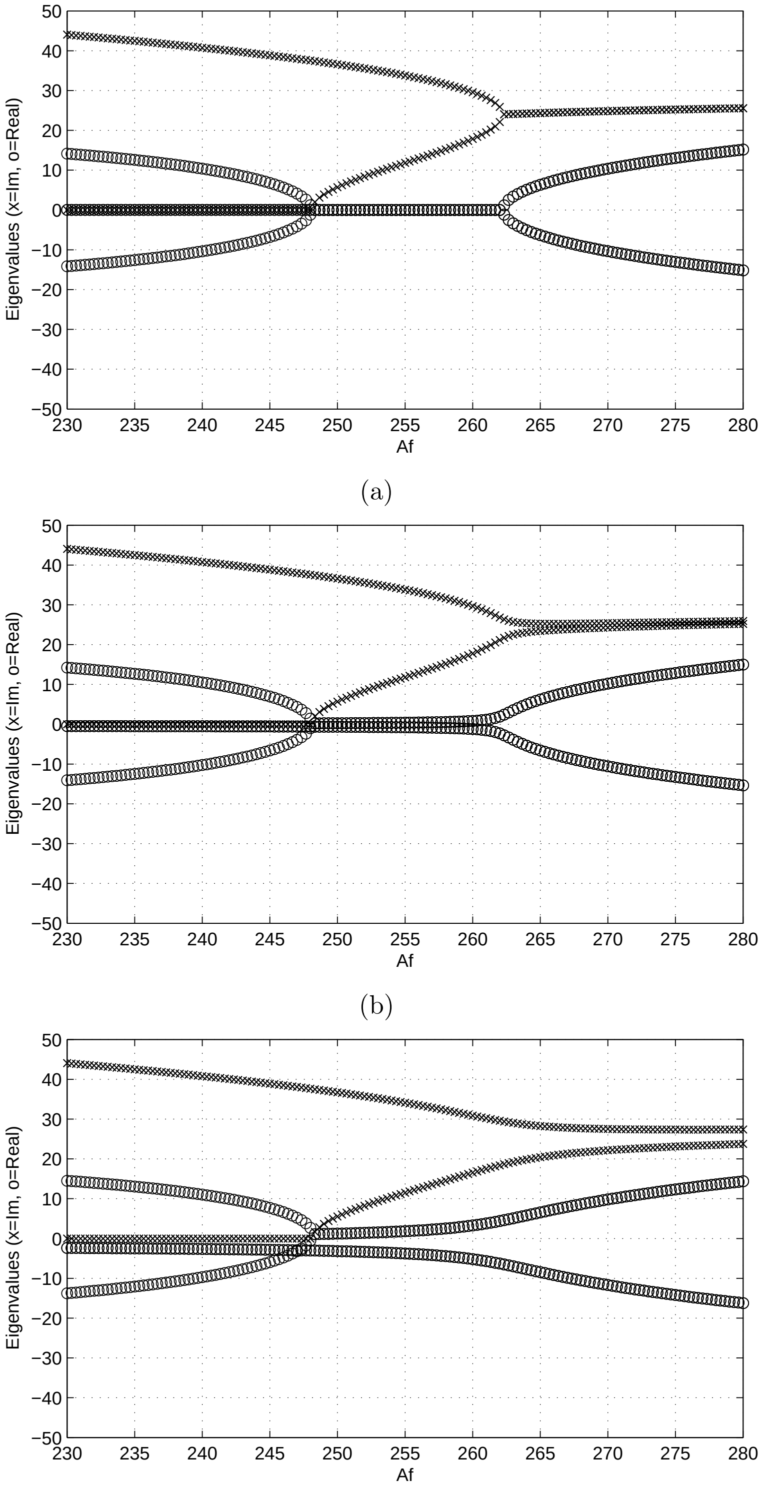

(a)

(b)

(c)

Figure 4.11: Plot of the eigenvalues at the divergence recovery zone for various amounts of small damping. Wall properties as in Figure 4.1, except that strucural damping is varied from top to bottom so that $\zeta = 0, 0.08$ and 0.4 respectively.

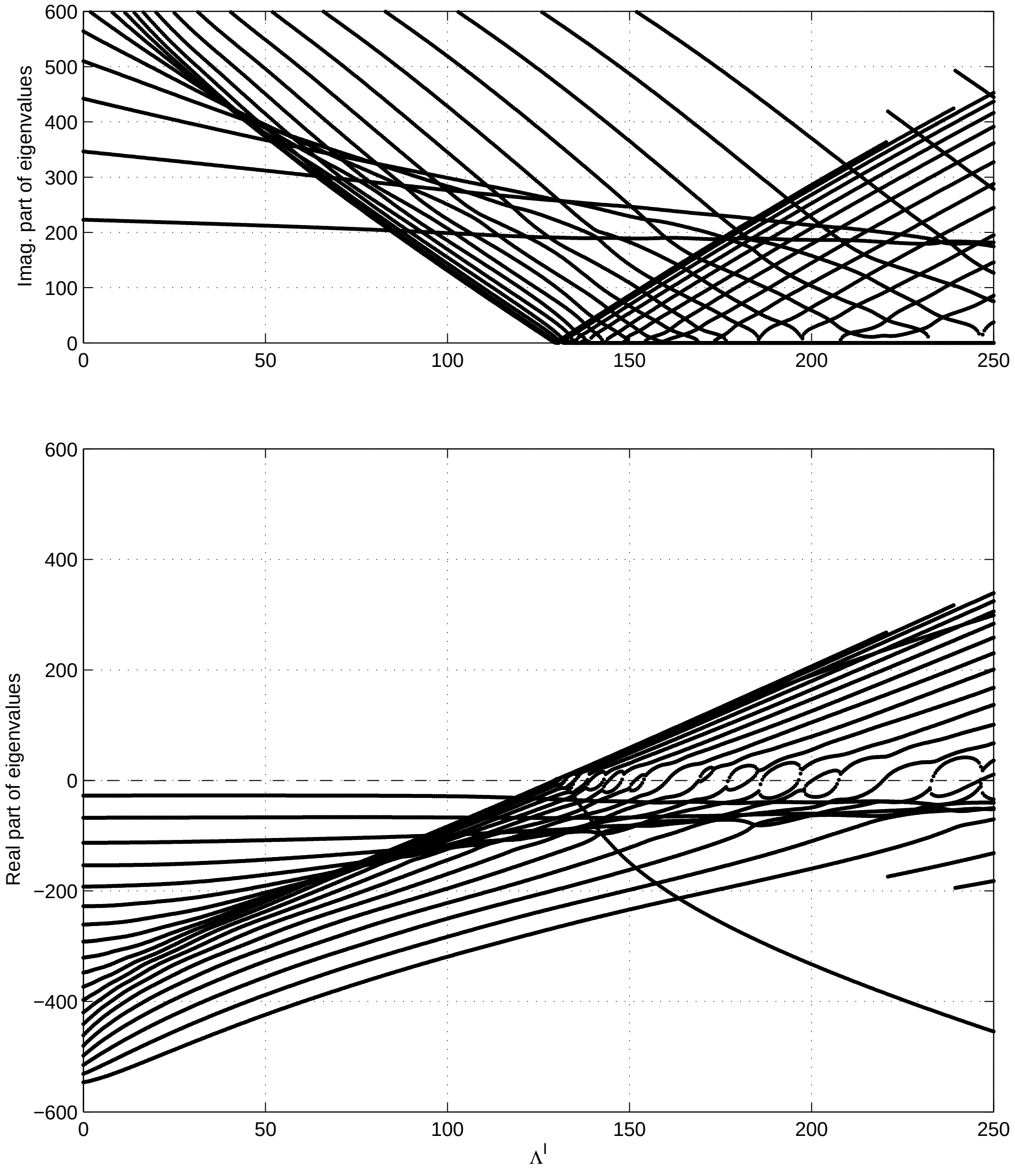

Figure 4.12: Imaginary (top) and Real (bottom) parts of the 40 eigenvalues nearest to $0 + 0i$ in the range $\Lambda^I = 0$ to 250 for a spring backed flexible wall with structural damping so that $\zeta = 0.56$

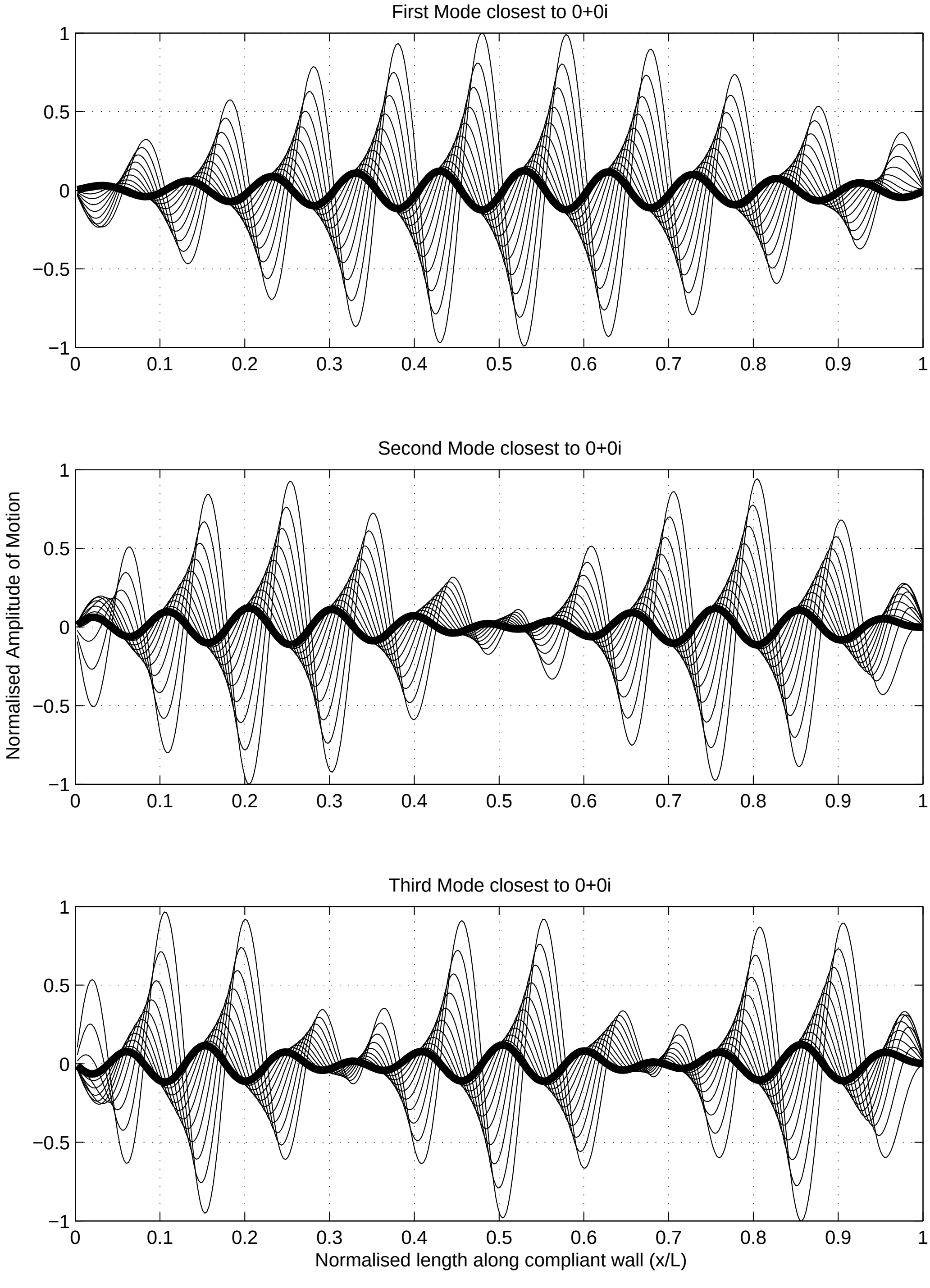

Figure 4.13: Wall motion for the the first, second, and third eigenmodes nearest to $0 + 0i$, when $\Lambda^F = 123$ (pre-divergence). Wall properties as in Figure 4.12. The bold line indicates the final position of the wall.

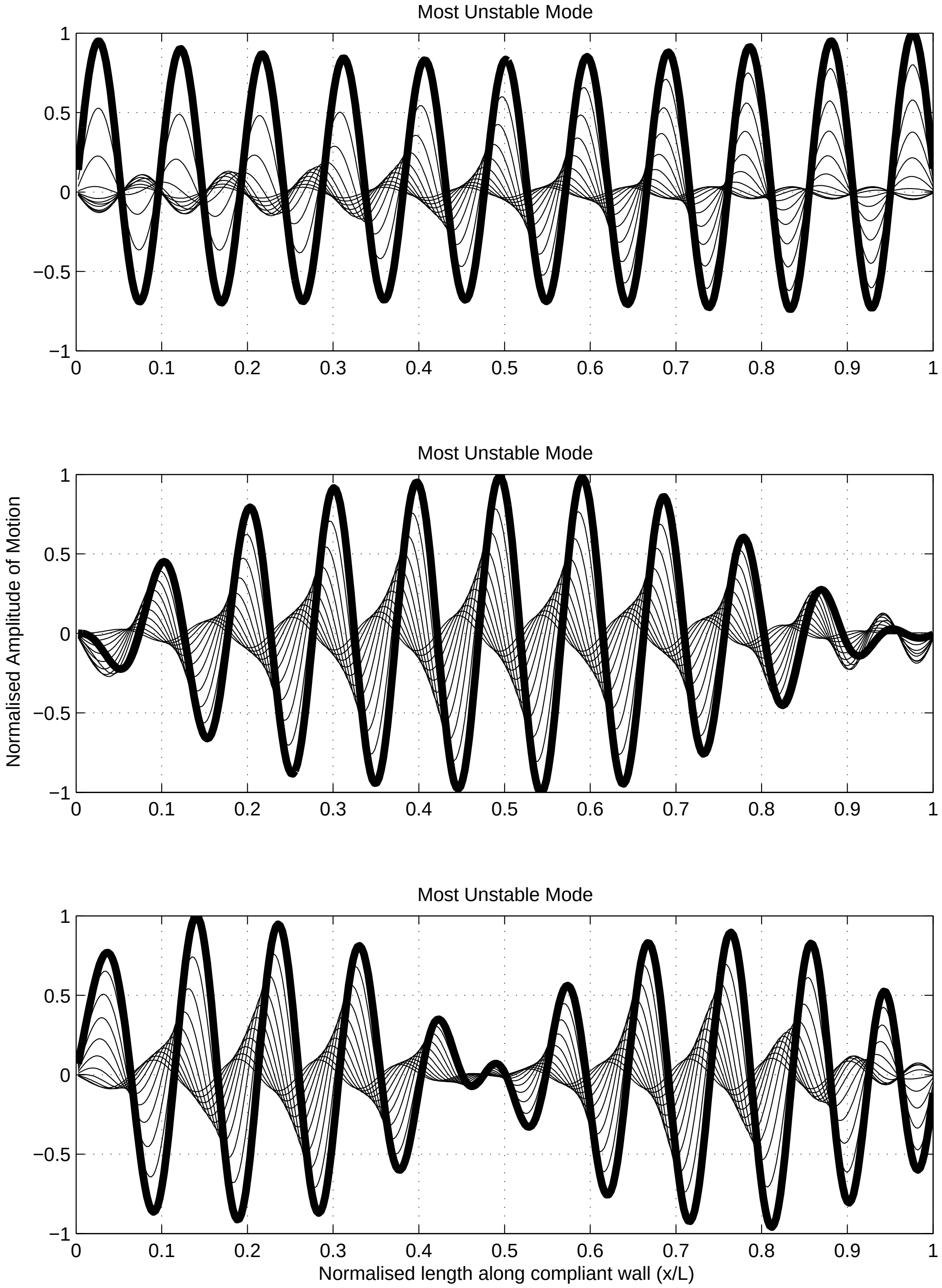

Figure 4.14: Wall motion for the most unstable mode (positive real part) at slightly post divergence onset flow speeds, where $\Lambda^F = 130, 136$ and 140 from top to bottom respectively. Wall properties as in Figure 4.12. The bold line indicates the final position of the wall.

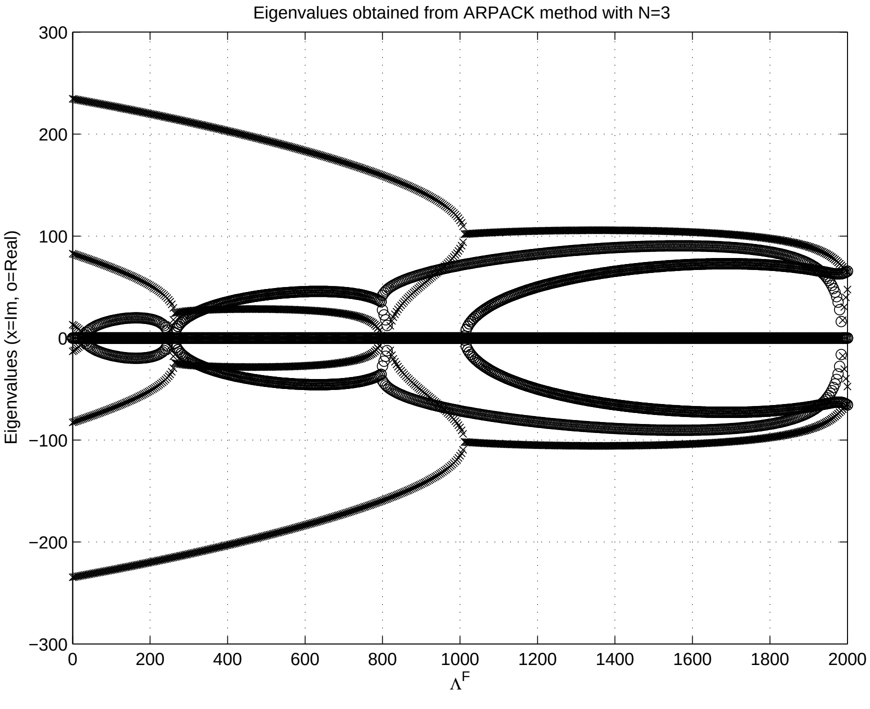

(a)

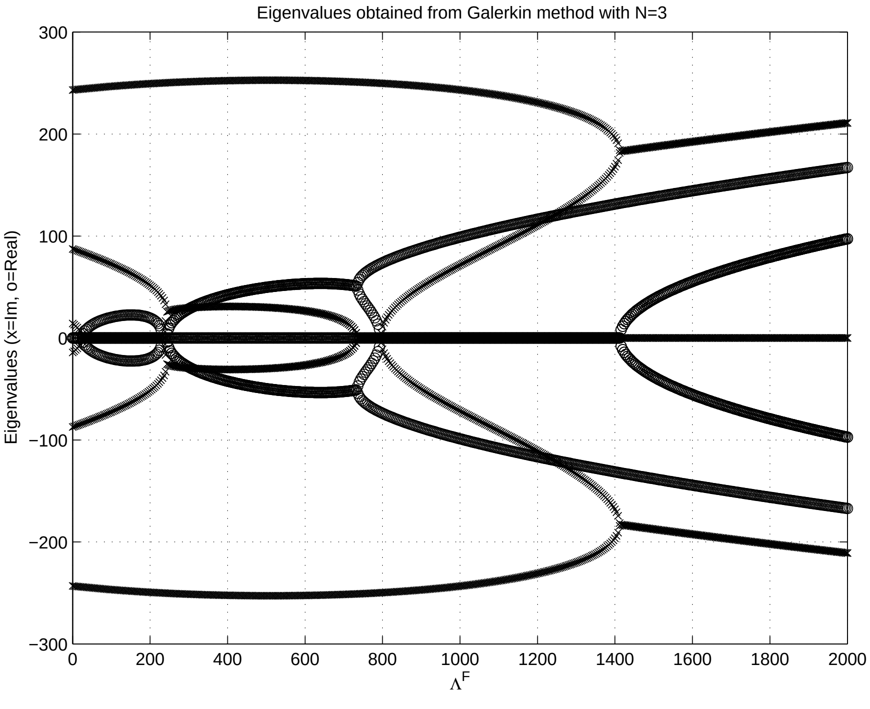

(b)

Figure 4.15: Imaginary (x) and Real (o) parts of the eigenvalues for a compliant wall with the same properties as in Figure 4.1. a) Using the full eigenvalue solution and b) using the Galerkin method with number of modes $N_m = 3$

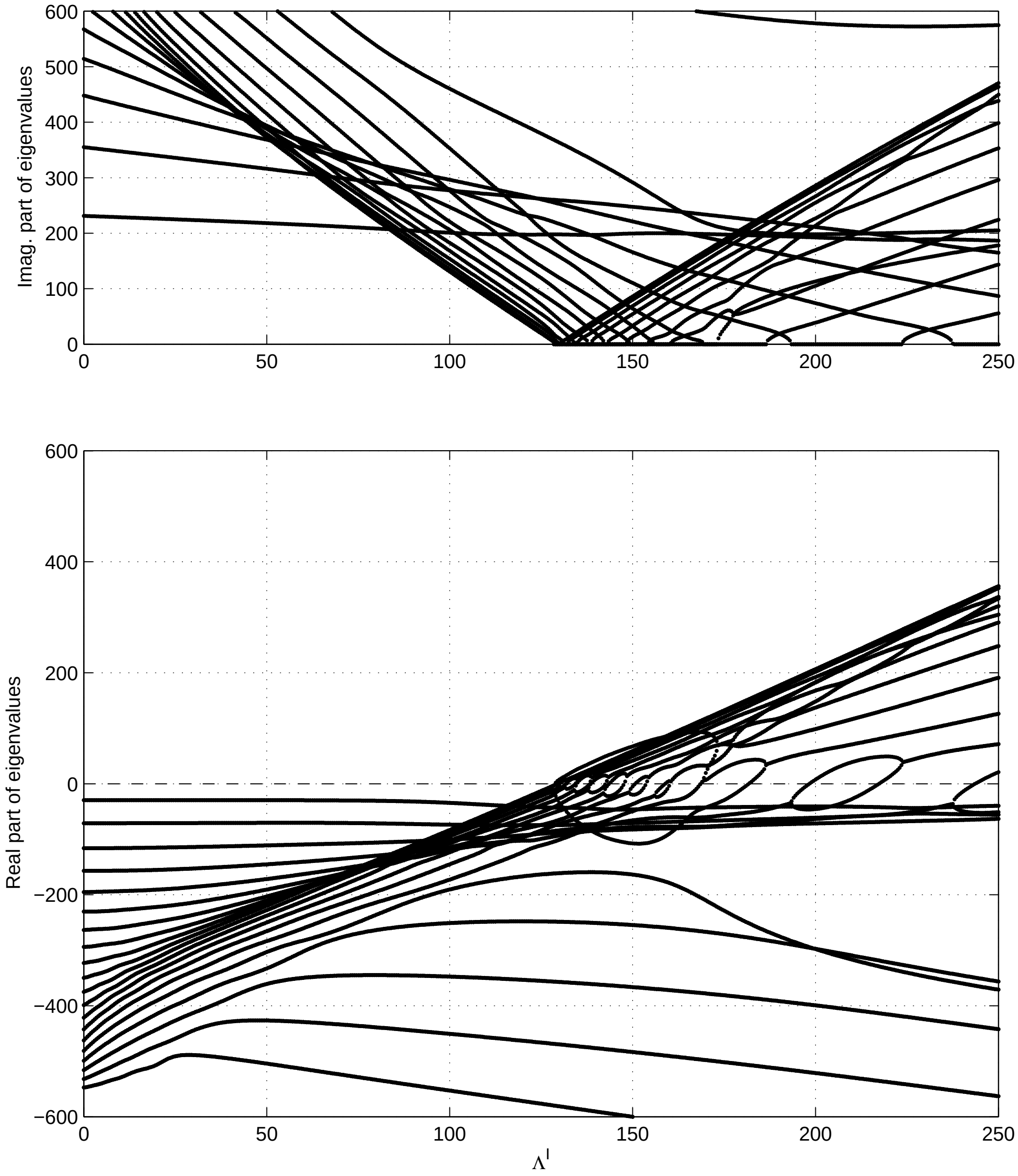

Figure 4.16: Imaginary (top) and Real (bottom) parts of the 40 eigenvalues nearest to $0 + 0i$ for a compliant wall with the same properties as in Figure 4.12. These results correspond directly to the results of 4.12 *except* that the results here are generated with the Galerkin method.

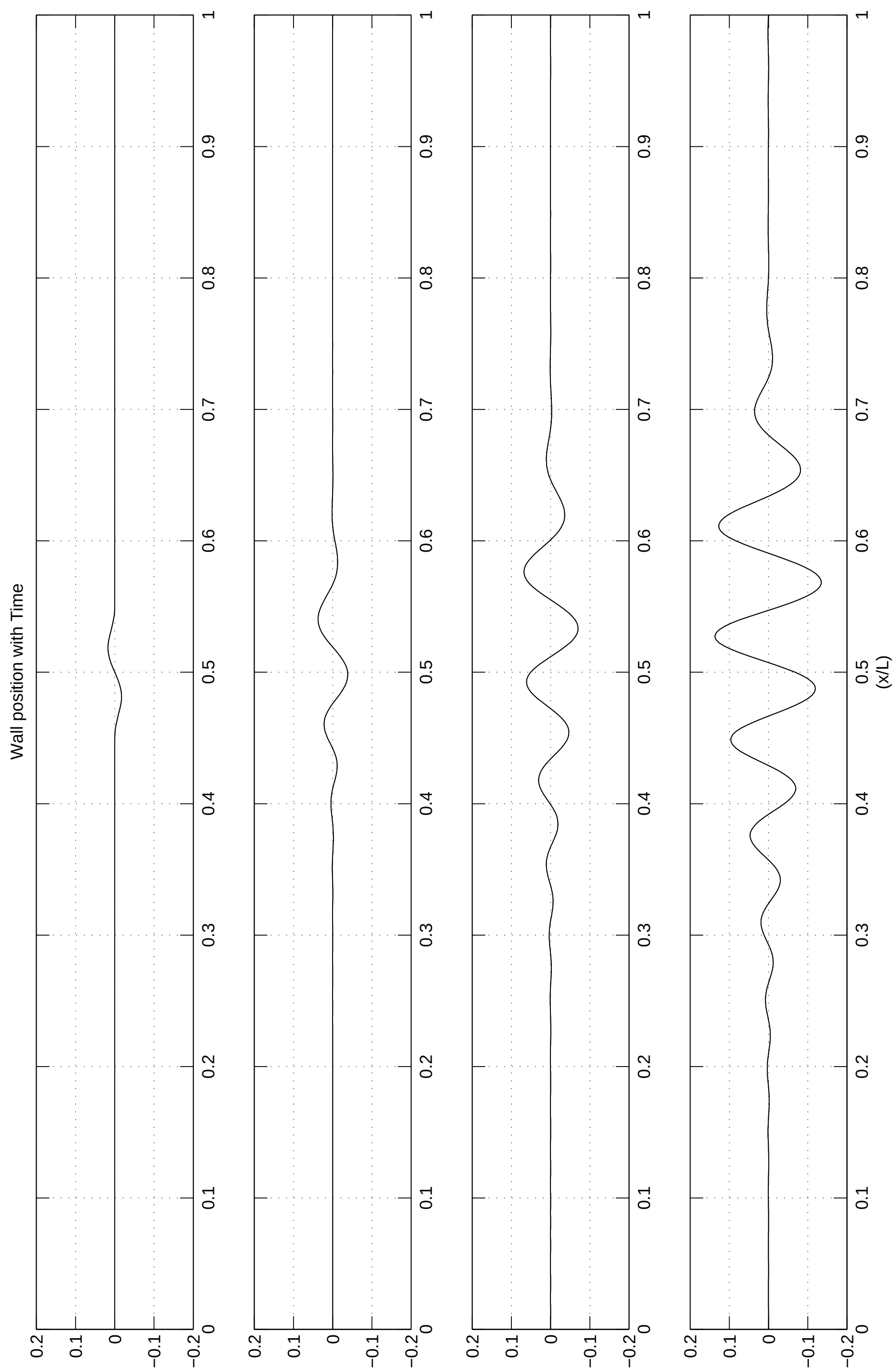

Figure 4.17: Wall position at time steps $1, 10, 20$ and 30, where time step size $dt' = 0.33s^*$, for the non-linear growth of a spring-backed flexible wall where $\Lambda^I = 277$ and structural damping giving a damping ratio of $\zeta = 0.12$. Starting from an isolated small-wavelength sinusoidal disturbance of wavelength $\lambda \approx \lambda_D$ at the centre of the compliant wall

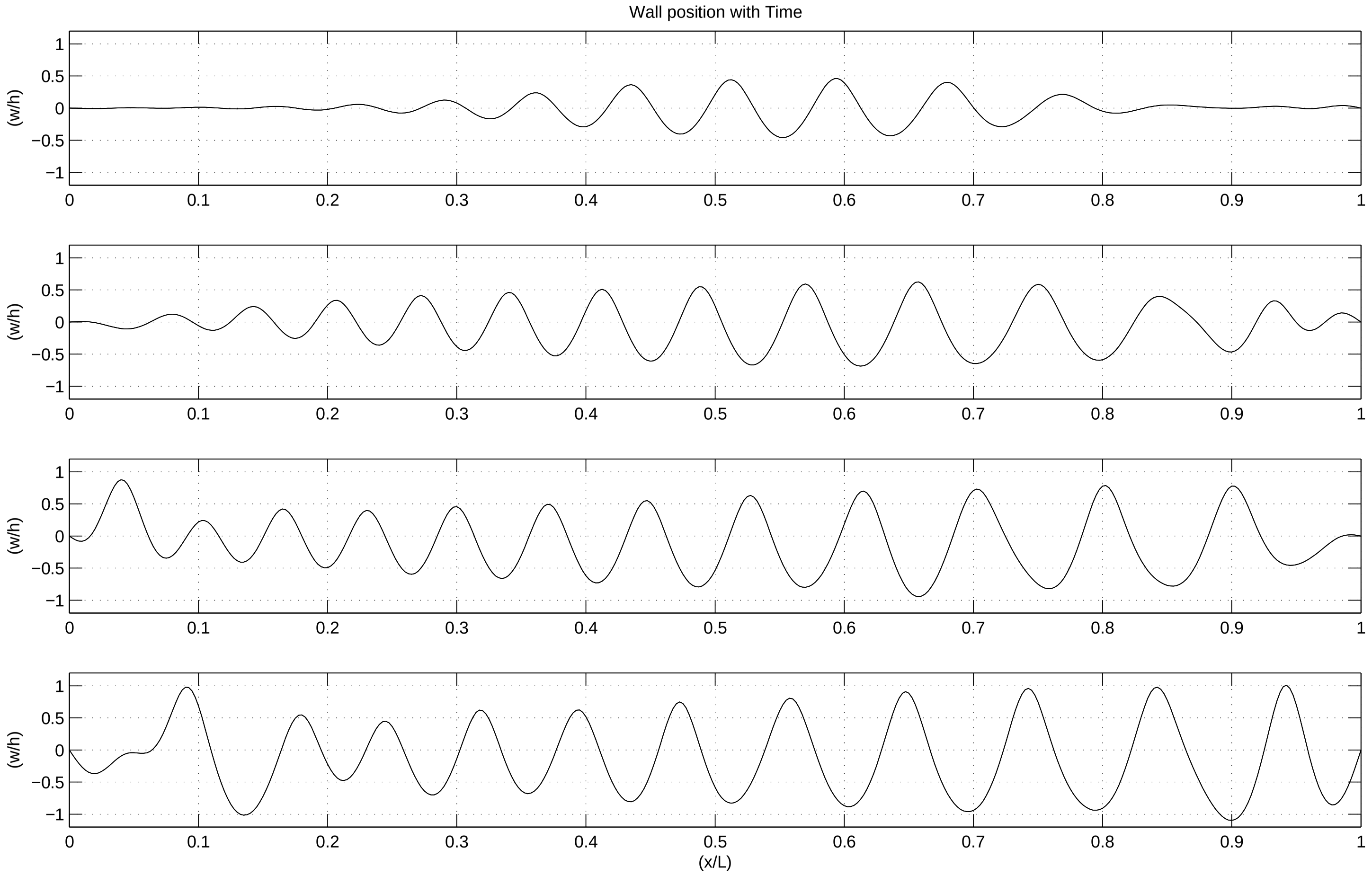

Figure 4.18: Wall position at time steps $50, 75, 100$ and 125 for the simulation parameters described in Figure 4.17

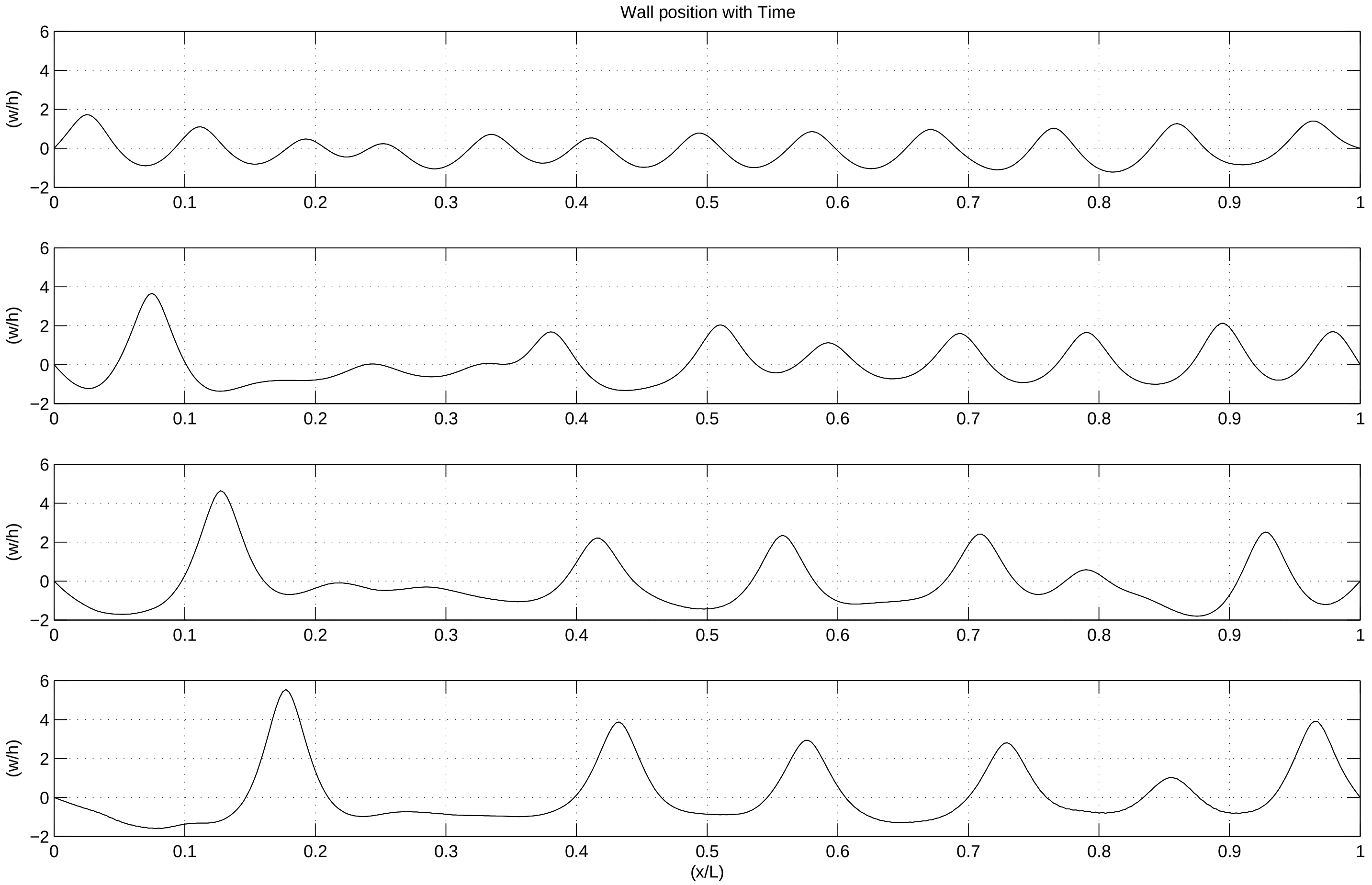

Figure 4.19: Wall position at time steps $150, 200, 250$ and 300 for the simulation parameters described in Figure 4.17

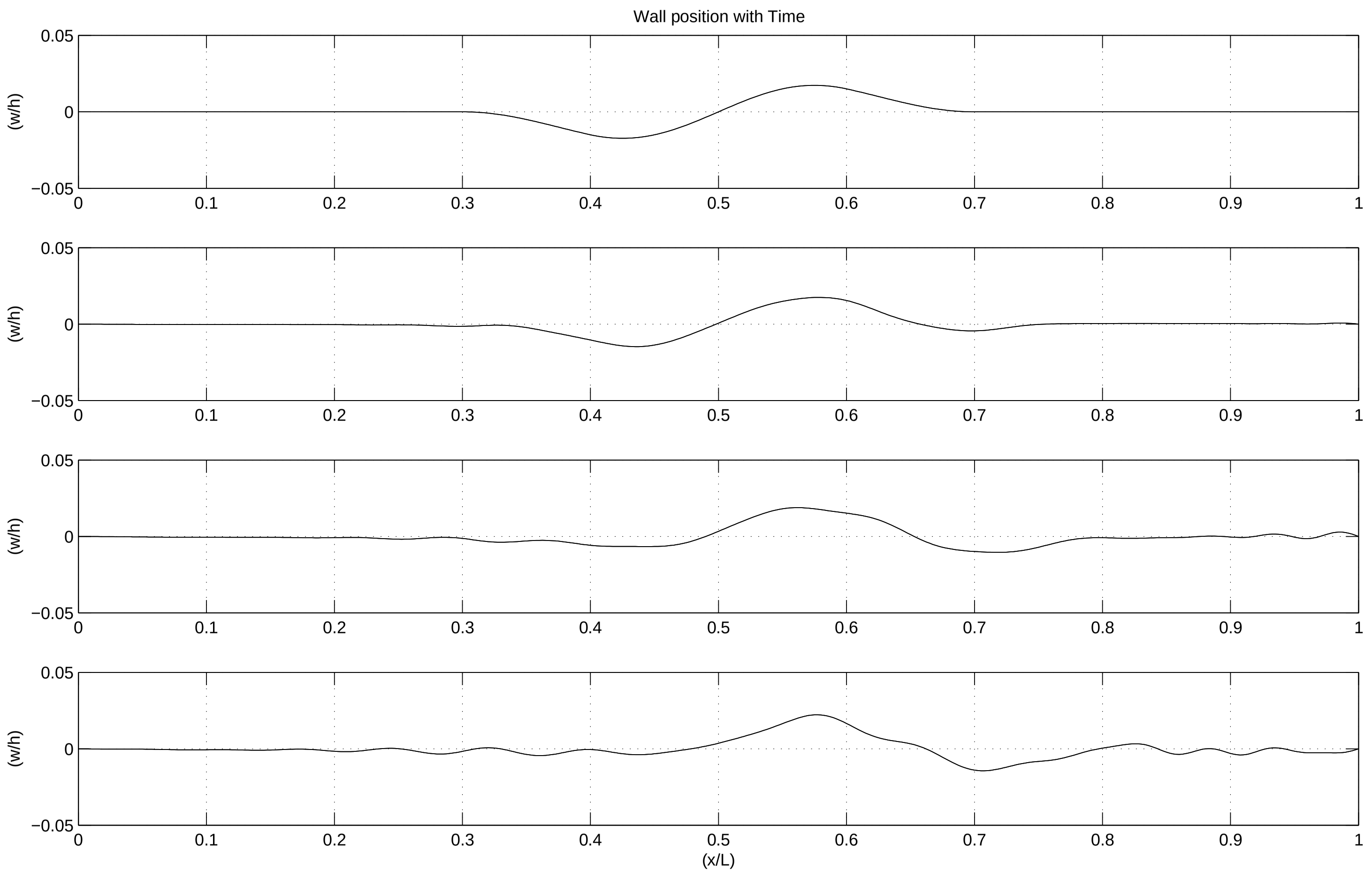

Figure 4.20: Wall position at time steps $1, 10, 20$ and 30, where time step size $dt' = 0.33s^*$, for the non-linear growth of a spring-backed flexible wall where $\Lambda^I = 277$ and structural damping giving a damping ratio of $\zeta = 0.12$. Starting from an isolated small-wavelength sinusoidal disturbance of wavelength $\lambda \approx 4\lambda_D$ at the centre of the compliant wall

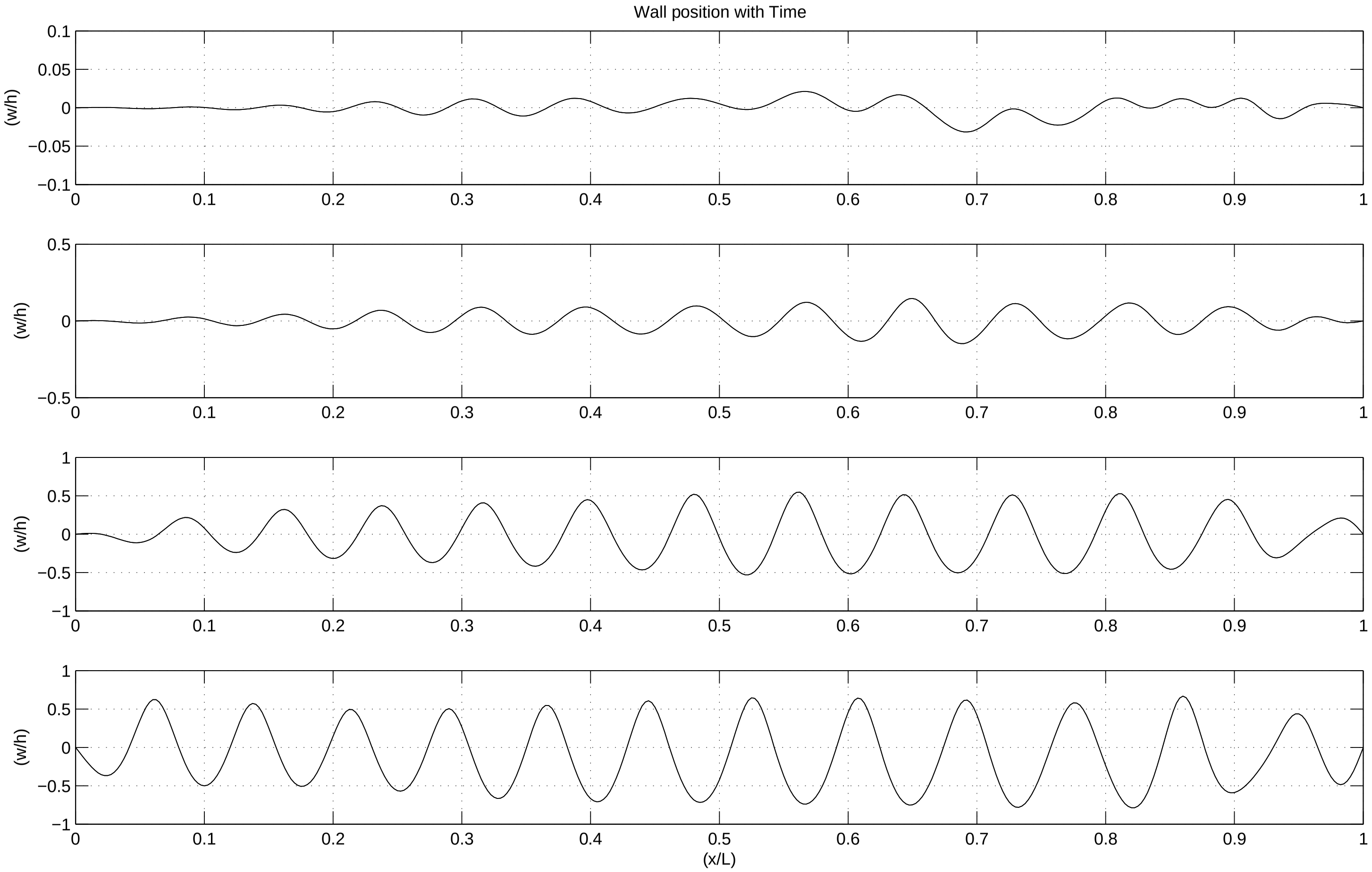

Figure 4.21: Wall position at time steps 50, 75, 100 and 125 for the simulation parameters described in Figure 4.20

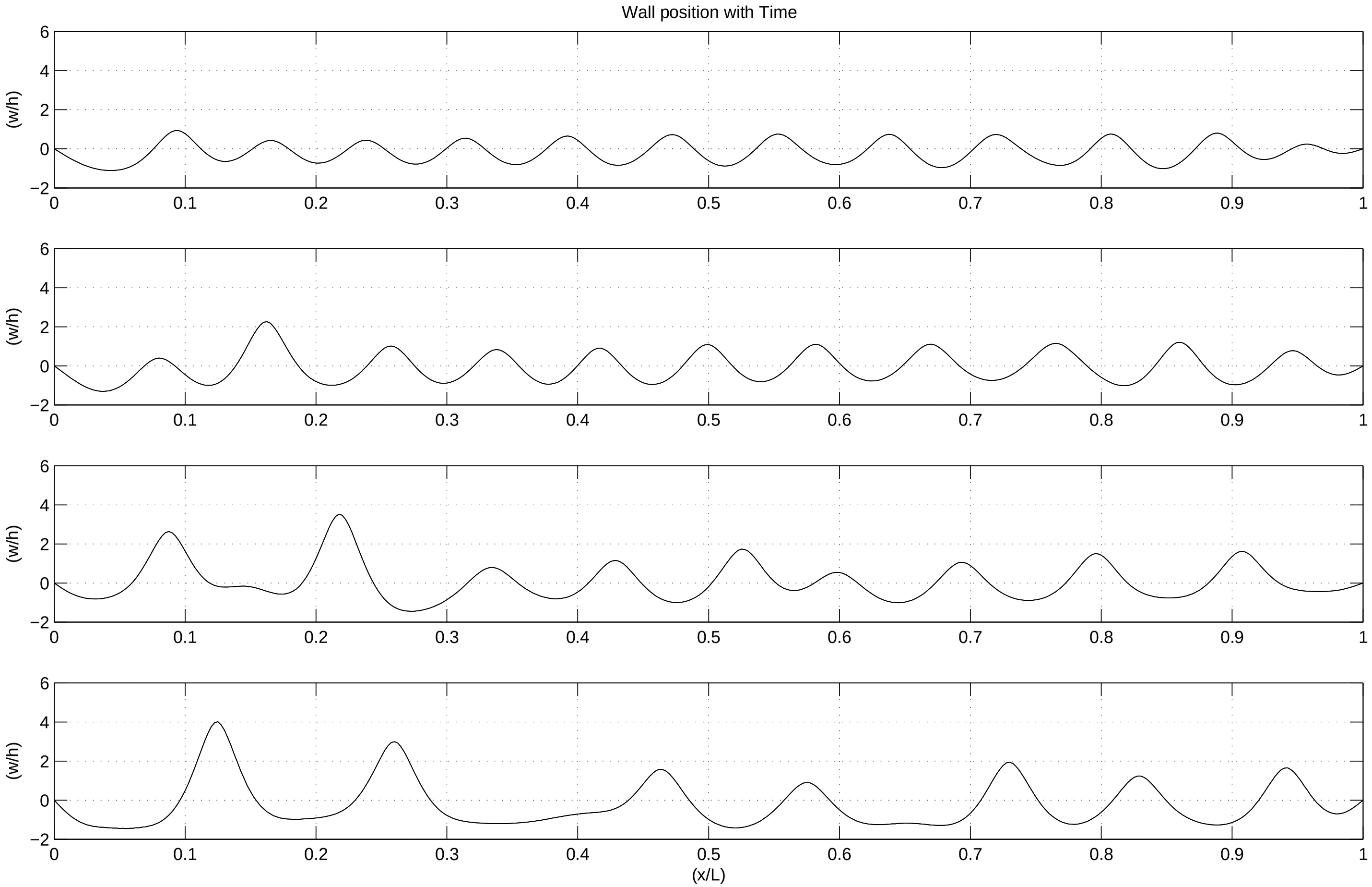

Figure 4.22: Wall position at time steps 150, 200, 250 and 300 for the simulation parameters described in Figure 4.20

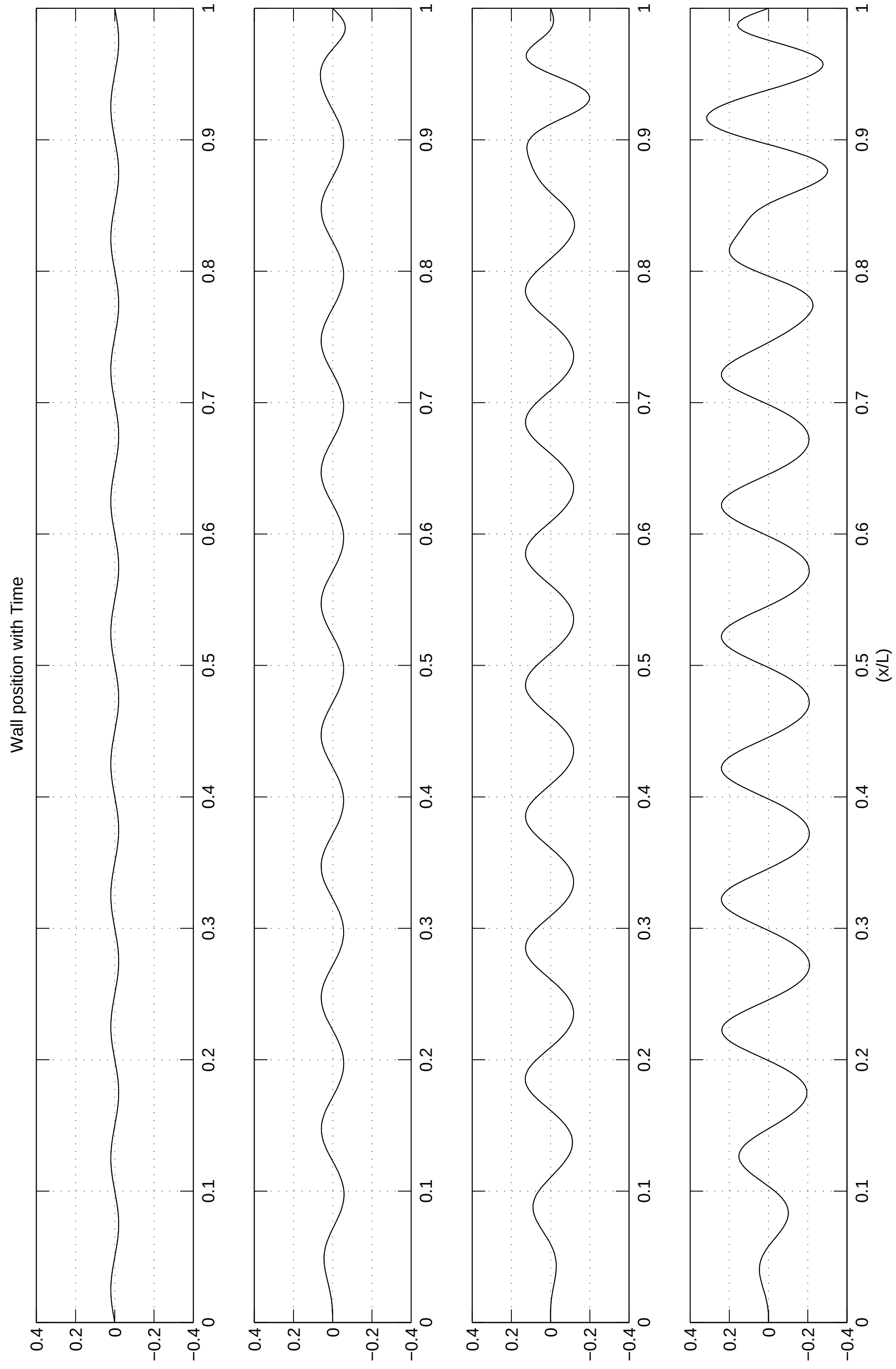

Figure 4.23: Wall position at time steps 1, 10, 20 and 30, where time step size $dt' = 0.33s^*$, for the non-linear growth of a spring-backed flexible wall where $\Lambda^I = 277$ and structural damping giving a damping ratio of $\zeta = 0.12$. Starting from an sinusoidal disturbance of wavelength $\lambda \approx \lambda_D$ that covers the entire compliant wall

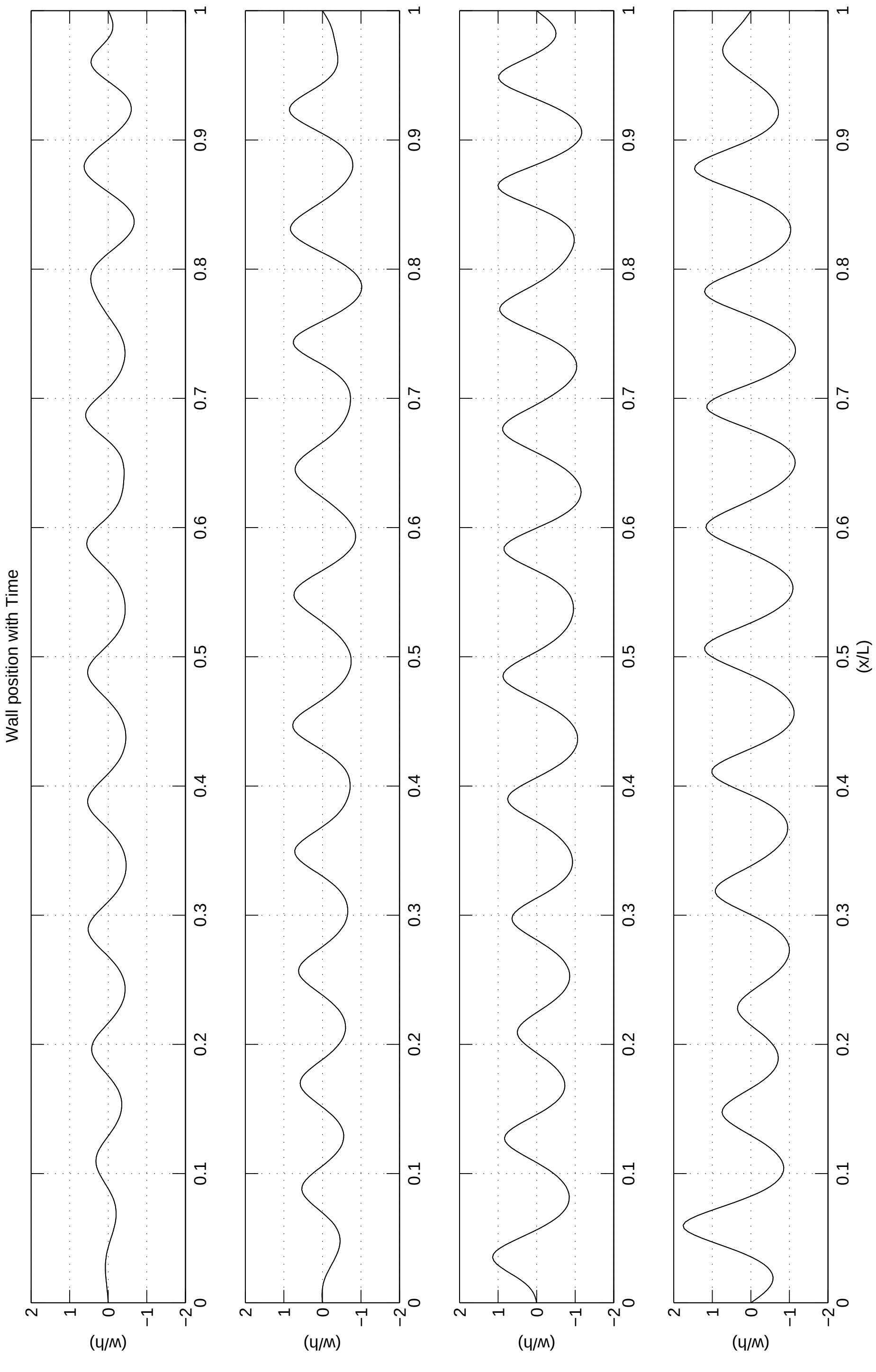

Figure 4.24: Wall position at time steps 50, 75, 100 and 125 for the simulation parameters described in Figure 4.23

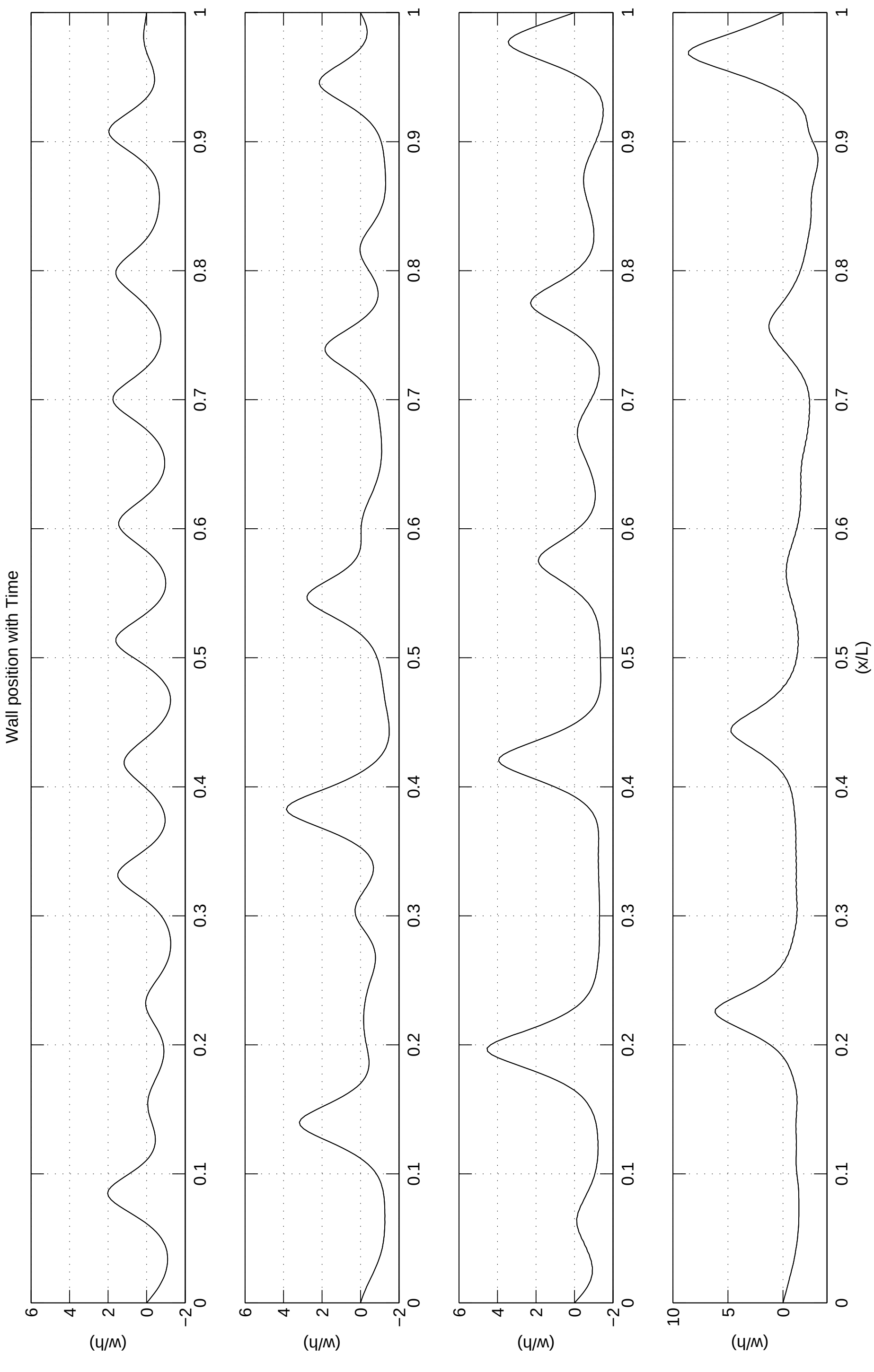

Figure 4.25: Wall position at time steps 150, 200, 250 and 300 for the simulation parameters described in Figure 4.23

Part III

The DVM Boundary Layer Model

Chapter 5

Boundary-layer modelling with the CCSVM

5.1 Introduction

In order to model the development of perturbations in the presence of a fully viscous boundary layer flow a boundary layer model is developed. The boundary layer model uses the Corrected Core-Spreading Vortex Method of Rossi [73]. The CCSVM is a variant of the traditional core-spreading discrete vortex method (DVM) which was found by Greengard [36] to approximate a set of equations that are not the viscous Navier-Stokes equations. The CCSVM corrects for this to give a solution to the Navier-Stokes equations.

Various other viscous vortex methods exist. Other methods considered were the vortex redistribution, random walk and diffusion velocity methods. A review of these methods is found in Takeda et al. [78]. The CCSVM was selected as a desirable viscous vortex method because it is deterministic, maintains better bounds on error control, is simple to implement and can be easily merged with a method for implementing upstream/downstream conditions. One of the greatest advantages of this method is that the vortex fusion algorithm used to control problem size can also be utilised to detect and deal with near-wall vortices. This eliminates the need for a separate algorithm for dealing with the flow in the near-wall region, such as using vortex sheets.

In the following sections a description of the formulation of the CCSVM is given along with some numerical experiments that validate its accuracy across a range of Reynolds numbers. The coupling of the CCSVM to the wall algorithm through the pressure formulation is then considered. A novel method for handling the far-field boundary conditions is also presented.

5.2 Formulation of the inviscid DVM

Before formulating the viscous method a brief introduction to the formulation of the standard DVM for inviscid fluid flow is given. The fluid transport equations to be solved are the two-dimensional, unforced, incompressible Euler's equations given in Equation 5.1 along with the two-dimensional mass conservation equation in Equation 5.2.

$$\begin{aligned} \dot{\vec{u}} + (\vec{u} \cdot \nabla)\,\vec{u} &= -\frac{1}{\rho}\nabla p \qquad (5.1) \\ \nabla \cdot \vec{u} &= 0 \qquad (5.2) \end{aligned}$$

These equations correspond to the Navier-Stokes equations at infinite Reynolds number (or zero viscosity). The curl operator is applied to the equations, which eliminates the pressure variable and produces the vorticity transport equation. In a two-dimensional flow field, the vortex stretching term, $(\omega \cdot \nabla)\vec{u}$, vanishes to zero. The resulting two-dimensional vorticity transport equation for the scalar two dimensional vorticity field is given by Equation 5.3,

$$\frac{\partial \omega}{\partial t} + (\vec{u} \cdot \nabla)\,\omega = 0 \qquad (5.3)$$

where ω is the two-dimensional scalar vorticity field, defined as the curl of the velocity field as

$$\omega = v_x - u_y \qquad (5.4)$$

Tracking the vorticity in a Lagrangian reference frame, Equation 5.3 reduces to

$$\frac{D\omega}{Dt} = 0 \tag{5.5}$$

This indicates that vorticity is conserved along particle paths. As Strain [76] states, "... the 2D Euler equations reduce to an infinite system of ordinary differential equations for the flow map".

The vorticity is inherently linked to the velocity field by Equation 5.4. Therefore, to close the system of equations and enable the calculation of particle stream paths the unknown velocity field must be determined from Equations 5.2 and 5.4. From these equations, the solution for velocity field $\vec{u}\,(x, y)$ for a given vorticity field $\omega\,(x_n, y_n)$ is given by the Biot-Savart law

$$\vec{u}\,(\vec{x}) = \int K\,(\vec{x} - \vec{x}_n)\,\omega\,(\vec{x}_n)\,dx_n dy_n \tag{5.6}$$

where K is the Biot-Savart kernel that corresponds to the x and y components in the velocity field.

$$K\,(\vec{x}) = \frac{((x - x_n), \ -(y - y_n))}{2\pi|\vec{x} - \vec{x}_n|^2} \tag{5.7}$$

5.2.1 Numerical Form

In order to solve numerically the system given by Equations 5.6 and 5.7 the 'infinite system' must be discretised to a finite number of vorticity impulse functions. In this case, the velocity field for unit circulation created by each point vortex remains the same as that defined by Equation 5.7. The integral equation presented in Equation 5.6 can be reduced to a finite summation of the vortex cores as

$$\vec{u}\,(\vec{x}) = \sum K\,(\vec{x} - \vec{x}_n)\,\Gamma_n \tag{5.8}$$

where Γ_n is the strength of each vortex core that must be prescribed at the initial conditions or at creation of each vortex element. In the inviscid form, this strength Γ does not change with time as stated in Equation 5.5.

The means of evaluating the velocity field, and therefore the motion of each vortex element, for any vorticity field is given by Equation 5.8. Therefore the evolution of the vorticity field, represented by the vortex elements, can be determined from some initial condition by a numerical time-stepping scheme. The position of each vortex element at some time $t + \delta t$ can be determined from their positions at time t by

$$\vec{x}_n^{t+\delta t} = \vec{x}_n^t + \vec{u}_n dt \tag{5.9}$$

5.3 Mathematical Formulation of the CCSVM

The full mathematical formulation of the CCSVM is presented in detail in Rossi [73]. Therefore, only the pertinent features of the method are presented here. Later, detailed descriptions are presented for the new methods that are developed for handling the no-slip and no-flux boundary conditions at the wall-flow interface.

Conceptually, the CCSVM is a simple algorithm. The vortex cores are allowed to grow and diffuse through time according to the exact solution of the diffusion equation. In this sense it is the same as the traditional core-spreading method that has been shown by Greengard [36] to approximate equations other than the Navier-Stokes.

The fluid transport equations to be solved are the two-dimensional, incompressible Navier-Stokes equations. The curl operator is applied to the equations, which eliminates the pressure variable and produces the vorticity transport equations for the scalar two dimensional vorticity field, as in Equation 5.10

$$\frac{\partial \omega}{\partial t} + (\vec{u} \cdot \nabla)\,\omega = \nu \nabla^2 \omega + (\nabla \times f) \tag{5.10}$$

Where f is some external forcing function (such as gravity) which in this work will be considered zero. The method uses Gaussian smoothed particles (also know as Lamb vortices) that are self-similar solutions to the diffusion equation. The scalar vorticity and vector velocity fields produced by a single Gaussian vortex element are given by Equations 5.11 and 5.12 respectively

$$\omega = \frac{\Gamma}{\pi\sigma(t)^2}\exp\left(\frac{-{R_{ij}}^2}{\sigma(t)^2}\right) \tag{5.11}$$

$$\vec{u}_i = \frac{\Gamma}{2\pi R_{ij}}\left(1-\exp\left(\frac{-{R_{ij}}^2}{\sigma(t)^2}\right)\right) \tag{5.12}$$

where R_{ij} is the absolute distance between the vortex core and the evaluation point, defined as $R_{ij} = \sqrt{(x_i - x_j) + (y_i - y_j)}$.

It is also useful to integrate these functions along a linear path from $-\infty < x < \infty$ and similarly across $0 < x < \infty$. The resulting infinite and semi-infinite vortex *sheets* have application as computational elements near the wall and in the upstream and downstream far-field respectively. A plot of the velocity fields taken through a cross-section of point vortex elements as well as infinite vortex sheet elements is shown in Figure 5.1.

The cores of these particles are allowed to spread and diffuse through time exactly according to the solution of the diffusive term so that the time-dependent core size function becomes

$$\sigma(t) = \sqrt{4\nu t_v} \tag{5.13}$$

where t_v is the time required for the vortex core to spread from an impulse function in agreement with the diffusion equation. This solves the diffusive term exactly but incorrectly solves for the convective term. This causes the uncorrected core-spreading method to approximate the wrong equation. Therefore, the diffusion is corrected by only allowing a vortex to diffuse to a certain limiting size, after which it is split into several more vortex cores and the process is repeated.

If this process is continued, the problem size will grow exponentially as more cores are split into many smaller ones. Remediation by a vortex fusion algorithm that merges close vortices into one must therefore be implemented. The processes of vortex splitting and fusion can be error controlled, ensuring consistency of the approximation to the solution throughout.

5.3.1 Core-spreading and splitting algorithm

At the centre of the CCSVM is the core-splitting algorithm. The core splitting is the fundamental difference between the original core-spreading algorithm, which approximated the wrong equations, and the CCSVM. In the CCSVM the vortex cores are permitted to spread according to the exact solution of the diffusion equation (no convection) where the core radius grows as stated in Equation 5.13. An arbitrary upper limit α is placed on the radius of the diffused vortex core. Any vortex core that reaches this limit splits into an arbitrary number of smaller cores, the size and strength of which are determined by conserving moments of vorticity. The process is depicted schematically in Figure 5.2.

The core-size of the newly created vortices, their strength, their insertion radius and positions are determined by conservation of moments of vorticity. The number of moments to conserve is equal to the number of unknowns to be solved in order to close the system of equations. In this work, conservation up to the second moment of vorticity is adopted. The strength of the new vortices is determined from the conservation of the zeroth moment. The conservation of the first moment enforces symmetry. The newly created vortices must be evenly spaced around the circle that dictates their insertion radius R_{IN}. The radius of insertion (R_{IN}) of the newly created vortices is determined through the conservation of the second moment of vorticity.

5.3.2 Core-merging algorithm

If the solution algorithm were allowed to proceed with splitting the vortices as in 5.3.1 the number of vortex elements in the flow field grows exponentially. Very rapidly the problem size becomes very large and solution becomes impractical. The solution also becomes very inefficient as the number of vortices grows because there will inevitably be some split cores that will lie almost in exactly the same position, having the same effect as a single vortex element.

The solution to this problem is to introduce a core-merging algorithm which merges vortices that lie close together into a single vortex with a similar vorticity field. A schematic of the vortex merging algorithm is shown in Figure 5.3. The procedure for the vortex merging algorithm is almost the reverse of the core-splitting algorithm presented in Section 5.3.1. Moments of vorticity are conserved throughout the merging process to give a closed system of equations that result in a final vortex that approximates the first. The difficulty with the core-merging procedure is that the original set of vortices lie in arbitrary positions and have arbitrary strengths. The system is not symmetrical, therefore, the resulting system of equations are slightly more complex.

As with the core-splitting algorithm, the critical parameters for the newly created vortex (created from merging nearby vortices) is determined by conserving moments of vorticity. By conservation of the zeroth moment, the merged vortex must have equal strength to the original n vortices. Conservation of the first moment determines the position of the new vortex. The merged-vortex will lie at the centre of vorticity of the original n vortices. The core-size of the merged vortex is determined by conservation of the second moment of vorticity.

A large part of the inefficiency associated with the core-merging procedure is locating and grouping vortices that lie close together. However, this computational 'weight' can be somewhat offset by the use of a Fast Multipole Method (FMM). Use of the FMM naturally dictates that vortices that lie close together must be found. Therefore, as will be shown later, the FMM can be used to determine particle-particle interactions as well as the proximity of neighbouring vortices efficiently.

5.4 Inter-facial modelling at the wall

An inherent problem of vortex methods is that as a smoothed vortex element moves close to a wall its core will cross the boundary and vorticity is essentially lost from the flow field that would normally be conserved. This creates problems with determining the flow field close to the boundary. Investigators have attempted various techniques to overcome this problem such as special vortex sheet methods, grid-based solutions and even ignoring the core function for vortices close to the wall. However, there are limitations with these methods. Implementation of a grid-based solver near the wall is complicated and strays from the grid-free and simple nature of the DVM. Use of special vortex sheets and ignoring the core-function near the wall tends to produce noisy results for the pressure footprint at the wall. Vortex sheet methods also suffer from inefficiency as sheets that require special consideration approximate the near-wall solution.

In our approach, as with the wall jet study of Rossi [72], the near-wall flow is approximated through the unsteady Rayleigh equation. Assuming that the diffusion length scale at the wall is small compared to the length of a panel, the diffusive term simplifies by one space dimension at the wall. The near-wall flow can then be approximated by a thin unidirectional flow above the wall. In this case, the diffusive length scale at the wall is small with respect to the panel length and solving the simplified diffusion equation, with y as the wall-normal coordinate, gives

$$\omega\left(y\right)=-\frac{2k}{\sqrt{4\pi\nu t}\exp\frac{-y^{2}}{4\pi t}} \tag{5.14}$$

where k is a parameter determined globally to impose the boundary conditions. Equation 5.14 is similar to the equation for the vorticity field of an infinite Gaussian vortex sheet along the x-axis when Equation 5.13 is substituted into Equation 5.14.

Therefore, the near wall flow may be represented by a set of Gaussian vortex sheets taken on a boundary element form. However, the Gaussian vortex approximation includes vorticity that lies below the wall which does not exist in the solution to the Rayleigh equation. This is cancelled by a point vortex sheet introduced on the wall of half strength and opposite sign to the Gaussian vortex sheet. The resulting boundary element used to impose the no-slip condition is a Gaussian-point vortex sheet couple.

In order to enforce the no-flux boundary condition, source/sink potential flow elements are also distributed along the panels. Thus, the complete boundary element that is used to enforce the no-slip and no-flux conditions, as well approximate the near-wall flow solution is a combination of three elements: a point source/sink sheet, a point vortex sheet, and a Gaussian vortex sheet. An approximate representation of this element using point vortices and sources and Gaussian blobs instead of sheets is shown in Figure 5.4.

5.4.1 Simultaneous boundary conditions

A distinct advantage to the CCSVM is that the solution of the diffusion equation is not solved through an operator-splitting method as in other methods such as the RWM. The most complicated and delicate procedure of a DVM is the handling of boundary conditions near a wall to impose the no-slip and no-flux conditions. Utilising source as well as the point-Gaussian vortex couple, these can efficiently be applied *simultaneously* using the CCSVM.

Because the core-spreading method does not rely upon operator splitting, these boundary conditions can be applied simultaneously at each time step.

The no-slip condition

A boundary element Gaussian-point vortex sheet couple handles enforcement of the no-slip condition. The influence of each wall Gaussian and point vortex sheet (assuming unit strength) on the other may be represented in matrix form. Using the resulting matrix of influence coefficients, the normal and tangential velocity at the elements due to the wall vortex boundary elements, denoted U_{VN} and U_{VT} respectively, are

$$\left[\left[I_{VNG} - \frac{1}{2}\left[I_{VNP}\right]\right]\right]\{\gamma\} = \left[I_{VN}\right]\{\gamma\} = \{U_{VN}\}, \tag{5.15}$$

$$\left[\left[I_{VTG} - \frac{1}{2}\left[I_{VTP}\right]\right]\right]\{\gamma\} = \left[I_{VT}\right]\{\gamma\} = \{U_{VT}\} \tag{5.16}$$

where γ is a vector defining the strength of each vortex couple boundary element, while I_{VTG}, I_{VTP}, I_{VNG}, and I_{VNP} are the square influence matrices of tangential and normal velocity respectively due to the Gaussian and point vortices.

The no-flux condition

A boundary element source sheet handles enforcement of the no-flux condition. By calculating the influence coefficients of each element upon another the normal and tangential velocity across each element due to the source/sink strengths, denoted U_{SN} and U_{ST} respectively, are

$$
\begin{aligned}
[I_{SN}]\{\lambda\} &= \{U_{SN}\} && (5.17)\\
[I_{ST}]\{\lambda\} &= \{U_{ST}\} && (5.18)
\end{aligned}
$$

where λ is a vector defining the strength of each source/sink boundary element, while I_{ST}, I_{SN} are the square influence matrices of tangential and normal velocity respectively due to the wall sources.

Simultaneous enforcement

Given the matrix equations represented by the sets of Equations 5.15 and 5.16. The boundary conditions may be solved simultaneously through the coupled set of matrix equations

$$
\begin{aligned}
[I_{VN}]\{\gamma\} + [I_{SN}]\{\lambda\} &= \{U_{SN}\} + \{U_{VN}\} = \{U_N\} && (5.19)\\
[I_{VT}]\{\gamma\} + [I_{ST}]\{\lambda\} &= \{U_{ST}\} + \{U_{VT}\} = \{U_T\} && (5.20)
\end{aligned}
$$

Straightforward solution of these equations for the vortex and source strengths yields

$$
\begin{aligned}
\{\lambda\} &= ([I_{SN}] + [K][I_{ST}])^{-1}(\{U_N\} + [K]\{U_T\}) && (5.21)\\
\{\gamma\} &= ([I_{VN}] + [K][I_{VT}])^{-1}(\{U_N\} + [K]\{U_T\}) && (5.22)
\end{aligned}
$$

where

$$[K] = -1\,[I_{VN}]\,[I_{VT}]^{-1} \qquad (5.23)$$

5.5 Constructing the flow-field

5.5.1 Initial conditions

At the start of a simulation the initial condition for the boundary layer is set as a homogeneous shear layer above the compliant wall. The shear layer is equal to the upstream boundary condition which approximates a Blasius boundary layer profile through the genetic algorithm described in Section 5.5.3 below.

5.5.2 Up/downstream far-field approximation

For the upstream and downstream boundary conditions, a flow field that approximates the Blasius boundary layer will be used. This flow field is constructed from semi-infinite vortex sheets as shown in Figure 5.5. This method is derived from the method of handling upstream and downstream boundary conditions for mixing layer models as demonstrated in Basu et al. [8, 9] and Inoue [41]. In mixing layer models a single semi-infinite vortex sheet is used to approximate the upstream flow profile, whereas in the boundary layer model multiple sheets are used to approximate the boundary layer profile upstream.

As with the mixing layer models, the more critical condition to set is the upstream flow profile. This defines the entry conditions for the vortex particles that then begin to convect downstream. Setting the downstream condition is important, more so from the point of view of conserving vorticity and therefore ensuring zero net circulation. The exact profile of the downstream boundary conditions is not critical because there is very little upstream communication from this boundary. For this reason, while the downstream conditions may not accurately represent the *real* profile this has little effect on the calculated profile at the compliant section. More sophisticated downstream conditions have been established in mixing-layer models by using conical-shaped semi-infinite vortex elements downstream. Likewise, more sophisticated techniques could be used in this form of boundary layer modelling. For this work, it was determined that the upstream communication of the crude downstream conditions would be minimal. This is based on qualitative as well as quantitative results from mixing layer experiments, such as Ashurst [5], Basu et al. [9], [8] and Inoue [41], which adopt a similar method for implementing upstream and downstream conditions. A thorough study that quantifies the effect of the upstream influence of the downstream boundary, and vice-versa, is left as future work in Part 4.

5.5.3 Genetic algorithm for vortex positioning

The approximation of the upstream velocity profile plays an important role in the starting conditions for downstream convection of the vortex elements. However, each semi-infinite vortex sheet element has three main parameters that must be adjusted in order to approximate a given velocity and/or vorticity profile. Namely, these are strength, core-size and position. Most of these parameters interact in a non-linear way with the final desired profile. Therefore finding a way to adjust the three parameters for N semi-infinite vortex sheets is a multi-variant non-linear optimisation problem involving $3N$ input variables.

In the work of Cafolla [12], a trial-and-error type method which required human intervention was used to optimise only three vortex sheet layers. This is a very time-consuming as well as inexact method of finding the optimal solution. Also, in the present work it was desirable to use an arbitrary number of semi-infinite vortex sheet elements to approximate the Blasius profile. Various techniques were considered for the solving this non-linear optimisation problem. However, most relied upon gradient-methods that found only local solutions to the problem. The Genetic Algorithm (GA) was found to be the most robust optimisation method for this type of non-linear multi-variant optimisation problem.

A detailed description of the development of the GA is presented in Appendix A. The algorithm is based on the principles of natural selection. Strings of parameters in binary form that constitute a solution represent individual 'gene-strings'. Based upon an individual's score it is assigned a probability of 'breeding' with another string of parameters. In this sense, stronger solutions have a higher probability of carrying the optimal bit-strings into future generations. This creates a 'survival of the fittest' situation that is effective for searching non-linear, multi-dimensional solution spaces for the global optimum.

The GA was applied directly to the problem of positioning the semi-infinite vortex sheets in order to optimise the upstream/downstream boundary conditions through the semi-infinite vortex sheets. Figure 5.6 shows the maximum and average scores for individuals in each generation for a typical run of the GA through one hundred generations. While the maximum score tends towards a convergence the average score lags behind as a result of the mutation rate. Continual mutation of the generations ensures that one individual does not dominate the solution, which could cause all the individuals to tend toward a local optimum. This also means that when one individual has found the global optimum, the average population will lag behind as mutation continues to search the remaining (less optimal) solution space.

Figure 5.7 shows the position of the vortices and the core sizes resulting from the GA. The core sizes and overlap limit of the vortices can be adjusted to ensure that vortices do not overlap excessively. Figure 5.8 shows the resulting boundary-layer velocity profile from the vortex distribution shown in Figure 5.7. The solid line represents the solution obtained from the GA optimisation over the discretised system, while the dashed line represents the Blasius boundary layer profile that the GA was attempting to optimise toward. Figure 5.9 shows the corresponding vorticity distribution for the velocity distribution shown in Figure 5.8. The vorticity is related to the first derivative of the velocity profile with respect to position above the wall. There is a slight mismatch between the Blasius boundary layer vorticity profile and the discretised approximation. This is particularly the case in the near-wall region where the near-wall approximation from the BEM matches with the free-stream solution of the DVM.

It is important to note that the Blasius boundary layer profile is adopted in this case because it provides some agreement with the work of Cafolla [12] as well as being a common known profile. However the method allows for any arbitrary flow profile to be selected. The initial profile will adjust throughout the simulation to give the full numerically solved profile from the Navier-Stokes equations, while only the upstream and downstream boundary conditions will influence the introduction and removal of vortices from the calculation domain. It is therefore logical to use an initial, and upstream (downstream) profile, that is as close to the expected calculated profile as possible. This will reduce transience from initial conditions and minimise the influence of the upstream and downstream boundary conditions on the calculation domain. These were the main factors behind the selection of the Blasius boundary layer profile in this work.

5.5.4 The complete flow field

Figure 5.10 shows a schematic diagram of the computational elements that are used to construct the entire flow field. In summary, the complete flow field is constructed from three major components. These are:

- **Free discrete vortices** - the vortex elements in the free flow field above the wall undergo core-spreading, splitting and merging to give a viscous solution to the high Reynolds rotational boundary layer flow field.
- **Boundary elements** - the special boundary elements positioned along the flexible surface enforce the no-flux and no-slip boundary conditions while also solving for the near-wall flow field. The near-wall flow field is conceptually similar to a viscous sub-layer
- **Semi-infinite vortex sheets** - the vortex sheets upstream and downstream from the calculation domain involving the discrete vortices are responsible for approximating the far-field flow.

5.6 Pressure formulation and wall-coupling

With the CCSVM, or any DVM for that matter, the pressure is not explicitly determined within the governing equations as a primitive variable. Therefore, as with the inviscid method in Section 3.2.2, the pressure must be determined separately and then coupled to the wall in order to create an equation that governs the driving of the wall.

In order to obtain full-coupling between the wall and fluid equations, it is desirable for the equations to take the same form as those presented in Equation 3.12 where the pressure can be separated into parts corresponding to wall velocity, acceleration and displacement respectively.

What follows then is a derivation of the pressure equations from the full Navier-Stokes equations. The development of the pressure equations from the Navier-Stokes is shown, followed by a full description of the methodology for numerical implementation.

5.6.1 Non-linear pressure formulation

This section presents the derivation of the full non-linear pressure formulation from the basis of the Navier-Stokes equations.

We begin with the full unsteady Navier-Stokes equations in fully-expanded form so that the individual terms may be easily identified. In the present work only a two-dimensional model will be considered; therefore, the equations are

$$\rho\frac{\partial u}{\partial t}+\rho\left(u\frac{\partial u}{\partial x}+v\frac{\partial u}{\partial y}\right)+\frac{\partial p}{\partial x}=\mu\left(\frac{\partial^2 u}{\partial x^2}+\frac{\partial^2 u}{\partial y^2}\right) \tag{5.24}$$

$$\rho\frac{\partial v}{\partial t}+\rho\left(u\frac{\partial v}{\partial x}+v\frac{\partial v}{\partial y}\right)+\frac{\partial p}{\partial y}=\mu\left(\frac{\partial^2 v}{\partial x^2}+\frac{\partial^2 v}{\partial y^2}\right) \tag{5.25}$$

taking v to be the velocity in the direction normal to the boundary and u to be tangential. Considering a small section at a solid boundary (that may be moving), the condition is always enforced that $u = 0$. However, between two points in time δt apart, a small slip velocity is created that in turn creates a small amount of vorticity that is ‘injected’ into the boundary layer. This small amount of vorticity indirectly enforces the no-slip condition. Therefore, between two time-steps, $u = 0$ at the first time and $u = (du/dt)\,dt$ at some time dt later.

Also, at least for the numerical method, the diffusion equation is solved exactly between timesteps. Therefore, the right hand side terms of the Navier-Stokes that correspond to diffusion should be set equal to 0.

It is important to note also that the slip velocity that is found at the wall between each time step is directly proportional to the amount of injected vorticity (γ). Therefore, writing the Navier-Stokes at this later time dt with these conditions gives

$$\rho \frac{du_s}{dt} = \rho \frac{d\gamma}{dt} = -\frac{\partial p}{\partial x} \tag{5.26}$$

The significance of Equation 5.26 is that it states that at a solid boundary where there are no convective effects (and diffusive effects have already been considered) then the pressure gradient along the wall is directly proportional to the rate of vorticity injection (which enforces the no-slip condition). This is not a new concept and is referred to as the Lighthill mechanism, as mentioned in Leonard [51].

The pressure derivation is based upon this concept that the streamwise pressure gradient at the wall is directly proportional to the amount of injected vorticity at each time-step. The full numerical implementation of the pressure formulation is described below.

Numerical implementation

To develop the numerical scheme by which the pressure is determined we investigate the differences between the fluid solution at two consecutive time-steps. At some time t the no-slip and no-flux conditions ensure the following balance at the wall interface

$$U_N = [I_{SN}]\{\lambda\} + [I_{VN}]\{\gamma\} + \{\omega_N\} = \{\dot{\eta}\} \tag{5.27}$$

$$U_T = [I_{ST}]\{\lambda\} + [I_{VT}]\{\gamma\} + \{\omega_T\} \;\; = 0 \tag{5.28}$$

at some time dt later, the balance becomes

$$\begin{aligned}\{U_N\} =& \left[I_{SN} + dI_{SN}\right]\{\lambda + d\lambda\} + \left[I_{VN} + dI_{VN}\right]\{\gamma + d\gamma\} \\ &+ \{\omega_N + d\omega_N\} = \{\dot{\eta} + d\dot{\eta}\} \end{aligned} \tag{5.29}$$

$$\begin{aligned}\{U_T\} =& \left[I_{ST} + dI_{ST}\right]\{\lambda + d\lambda\} + \left[I_{VT} + dI_{VT}\right]\{\gamma + d\gamma\} \\ &+ \{\omega_T + d\omega_T\} = 0 \end{aligned} \tag{5.30}$$

Subtracting Equations 5.27 and 5.28 from Equation 5.29 and 5.30 gives an expression for the change in slip and normal velocity flux between two time steps.

$$[I_{SN}]\{d\lambda\} + [dI_{SN}]\{\lambda\} + [I_{VN}]\{d\gamma\} + [dI_{VN}]\{\gamma\} + \{d\omega_N\} = \{d\dot{\eta}\} \tag{5.31}$$

$$[I_{ST}]\{d\lambda\} + [dI_{ST}]\{\lambda\} + [I_{VT}]\{d\gamma\} + [dI_{VT}]\{\gamma\} + \{d\omega_T\} = 0 \tag{5.32}$$

Multiplying Equation 5.32 by some constant and subtracting from Equation 5.31, then dividing the final result by the time-step duration dt gives an expression for the rate of change of vorticity at the wall between time-steps

$$\begin{aligned} K_C\left\{\frac{d\gamma}{dt}\right\} = \left\{\frac{d\dot{\eta}}{dt}\right\} &- \left\{\left(\frac{d\omega_N}{dt}\right) - K\left(\frac{d\omega_T}{dt}\right)\right\} \\ &- \left\{\left(\frac{dI_{\lambda N}}{dt}\right) - K\left(\frac{dI_{\lambda T}}{dt}\right)\right\}\lambda \\ &- \left\{\left(\frac{dI_{\gamma N}}{dt}\right) - \left(\frac{dI_{\gamma N}}{dt}\right)\right\}\gamma \end{aligned} \tag{5.33}$$

where

$$\begin{aligned} [K_C] &= [I_{VN}] - [K]\,[I_{VT}] \\ [K] &= [I_{SN}]\,[I_{ST}]^{-1} \end{aligned}$$

However, as was derived previously, Equation 5.26 states that the streamwise pressure gradient is directly proportional to the rate of vorticity injection. Therefore, substituting Equation 5.26 into Equation 5.33 gives an expression for the streamwise pressure gradient along the wall-tangential axis s at each time-step

$$\frac{dP}{ds} = K_P - K_C \left\{ \frac{d\gamma}{dt} \right\} \tag{5.34}$$

where

$$K_P = \frac{\rho}{2} [[I_{VN}] - [K]\,[I_{VT}]]^{-1}$$

The pressure may be achieved through integration of the above equation, yielding three distinct pressure terms

$$\int \frac{dP}{ds} ds = P = \delta P^S + \delta P^{U1} + \delta P^{U2} \tag{5.35}$$

where

$$\begin{aligned}
\delta P^S &= \int K_P \left[\left(\frac{d\omega_N}{dt} \right) - K \left(\frac{d\omega_T}{dt} \right) \right] ds \\
\delta P^{U1} &= \int K_P \left\{ \left[\left(\frac{dI_{\lambda N}}{dt} \right) - K \left(\frac{dI_{\lambda T}}{dt} \right) \right] \lambda - \left[\left(\frac{dI_{\gamma N}}{dt} \right) - \left(\frac{dI_{\gamma N}}{dt} \right) \right] \gamma \right\} ds \\
\delta P^{U2} &= \int -K_P \left(\frac{d\dot{\eta}}{dt} \right) ds
\end{aligned}$$

Comparison of this result with the pressure formulation of the non-linear inviscid flow model that was developed in Section 3.2.3 reveals similarities between the two pressure formulations. Particularly, the existence of three pressure terms that are functions of the wall position, velocity and acceleration respectively. In Equation 5.35, the hydrodynamic damping term δP^{U1} becomes a function of the wall velocity through λ and γ, which are both functions of wall velocity through Equations 5.21 and 5.22.

As with the inviscid flow model that was developed in Section 3.2.3 the pressure consists of three pressure terms, one of which is the steady pressure field, the other two relate to the motion of the wall. Of particular importance is the fact that the pressure term δP^{U2} is directly related to the acceleration of the wall. Therefore, the method of coupling the flow solution to the wall remain the same as for the inviscid method.

5.6.2 Wall mechanics and flow-coupling

The wall mechanics remain the same as that presented in Equation 3.1, and the coupling by using the various pressure components remains similar to the method that was presented in Section 3.2.3.

5.7 Discussion

This model was selected because it has many advantages over other computational methods. Some of these advantages are:

- The vorticity based formulation of the CCSVM gives a more natural representation of the unsteady behaviour of high Reynolds number flow. The solution of the vorticity-velocity formulation of the Navier-Stokes equations by a DVM does not make any underlying simplifications that require turbulence-models or such to capture averaged unsteady behaviour at high Reynolds numbers.

- DVM's are based on a Lagrangian solution to the transport equations. The computational elements are radial basis function 'particles' that move with the streamlines of the flow. The computational 'grid' therefore naturally adapts to the changing boundary conditions (the wall motion). The 'grid' also naturally adapts to give greatest resolution where it is required at the points of high velocity gradient.

- The CCSVM is a robust method. It may be expanded to three dimensions if desired, and it may be adapted to solve for arbitrary flow-structure situations, not only boundary-layer flow. In three dimensions, although more complex due to the added vortex stretching term, there exist means of handling this extra term that do not adversely influence the method of flow-structure coupling presented in this work.

- The CCSVM has various desirable components within the method that allow for more efficient solution, particularly at the wall-flow interface. The components of the method may be exploited to achieve a more efficient solution.

However, there remain certain problems with the CCSVM of Rossi [73]. Some of these problems include:

- The method is difficult to couple to a solid boundary. Problems arise with the handling of computational elements that come in close proximity to the wall. The definition of 'close proximity' also introduces a new arbitrary parameter to the calculation.
- DVM's are notorious for being very sensitive to the setting of parameters, and many arbitrary parameters have to be dealt with in the CCSVM.
- The no-slip boundary condition cannot be enforced strongly. The condition of no-slip at the wall is enforced only by the injection of vorticity at the wall at each time step. While it can be argued that this gives a more realistic representation of vorticity evolution, it also means that there are instances where a certain amount of slip is tolerated at the wall.
- The pressure term does not appear explicitly in the vorticity-velocity form of the Navier-Stokes equations. This is a problem because it is the pressure that drives the wall. Therefore, an efficient means by which to calculate the pressure distribution at the wall must be developed.

5.8 Conclusion

A new computational method has been developed for modelling boundary-layer flow interactions with a flexible surface. Key features of the method include:

- a robust corrected core-spreading method that models viscous effects in flow over a compliant boundary;
- a novel boundary element method to impose the no-slip and no-flux boundary conditions concurrently at the moving wall-flow interface and with reduced numerical noise;

- a rapid genetic algorithm that aids the accurate enforcement of upstream and downstream conditions; and
- all of the techniques that are developed in here may be extended to model the corresponding three-dimensional system.

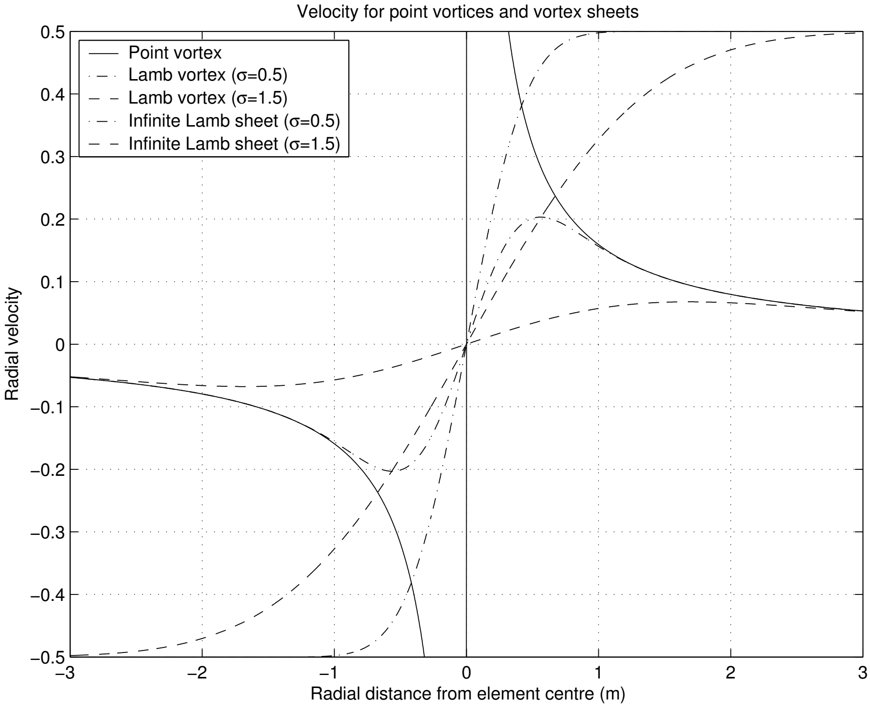

Figure 5.1: Plot of the velocity fields for single point and Lamb vortices and Lamb vortex sheets

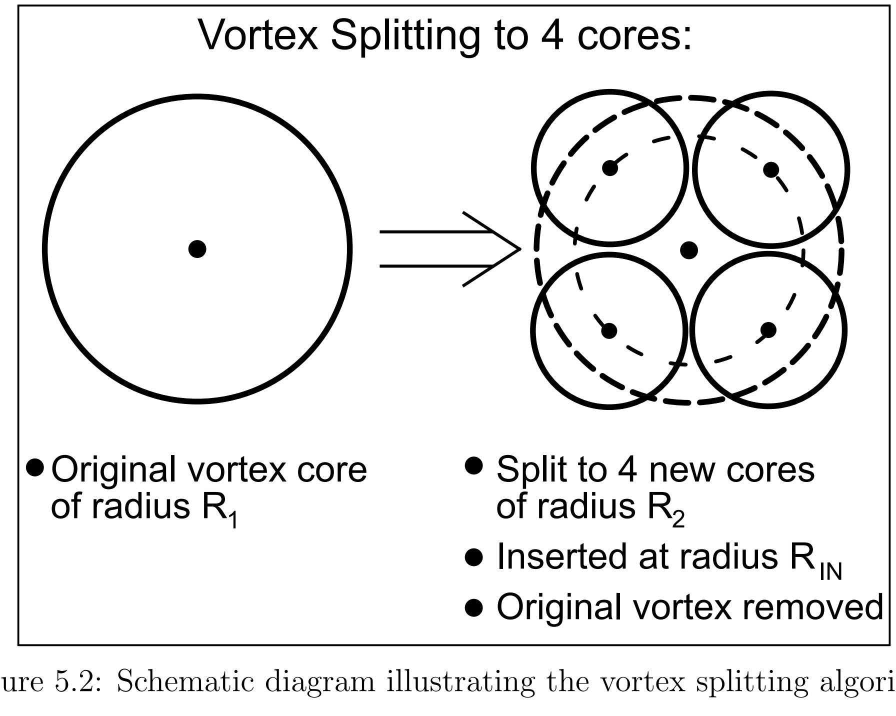

Figure 5.2: Schematic diagram illustrating the vortex splitting algorithm

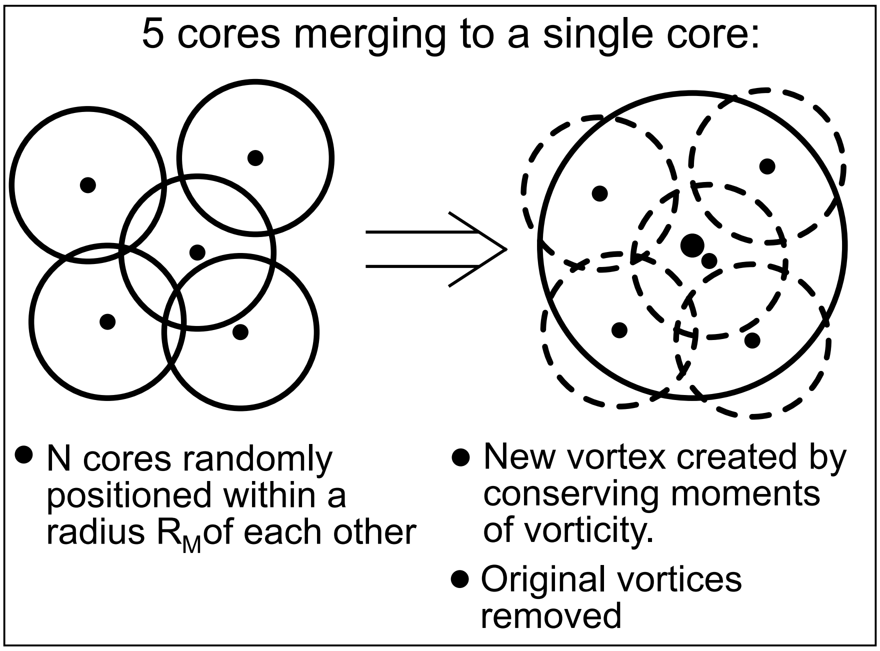

Figure 5.3: Schematic diagram illustrating the vortex merging algorithm

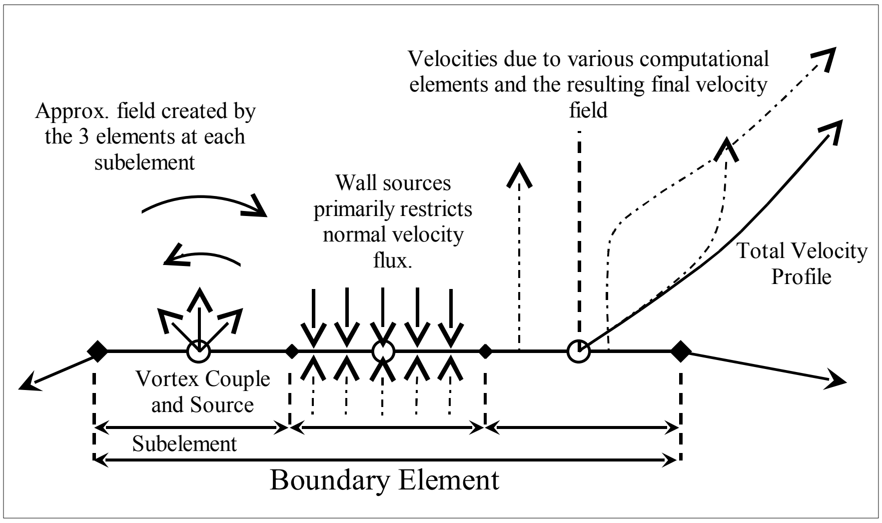

Figure 5.4: Schematic diagram showing the use of computational elements in the domain near the flexible wall.

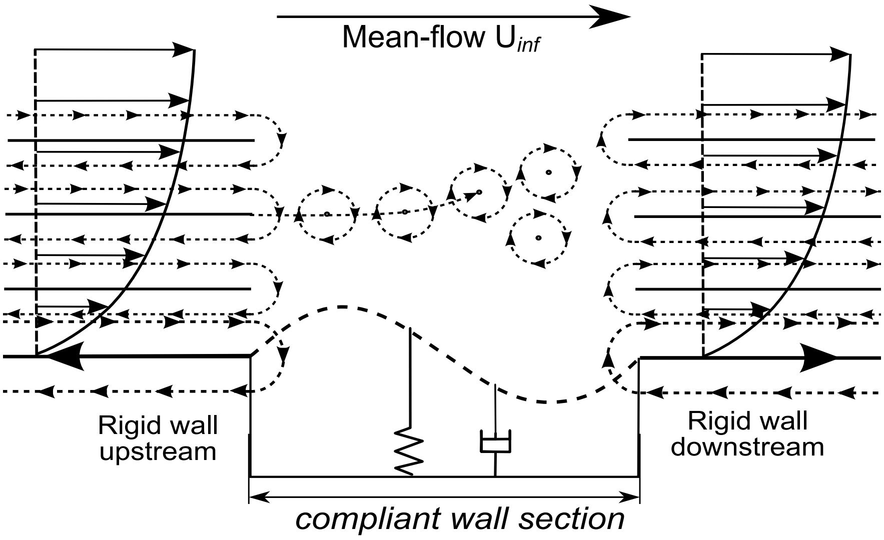

Figure 5.5: Use of semi-infinite vortex sheets to approximate the Blasius boundary layer profile upstream and downstream of the compliant section

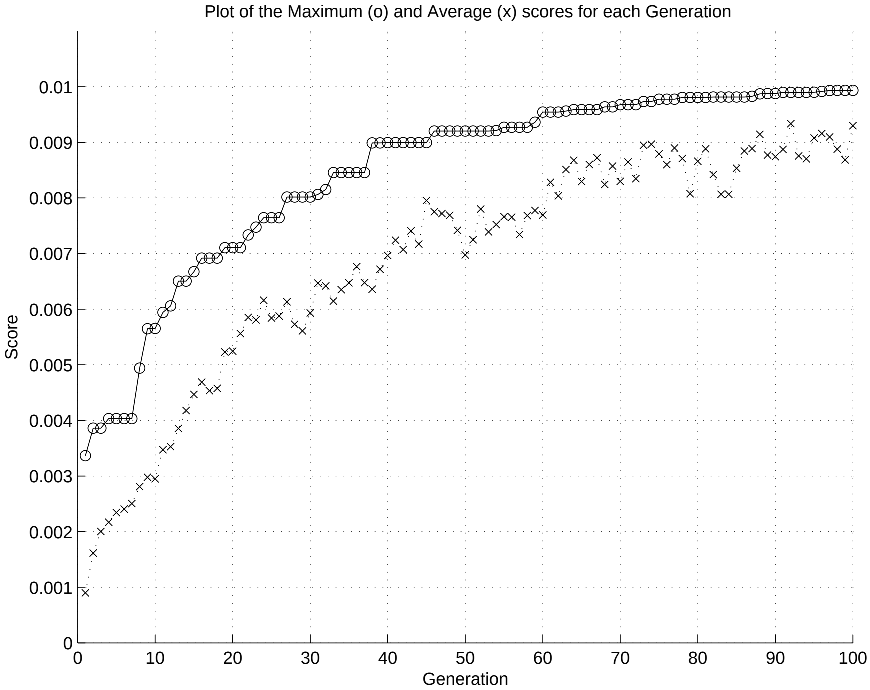

Figure 5.6: Plot of the GA maximum (o) and average (x) scores converging to an optimal over 100 generations.

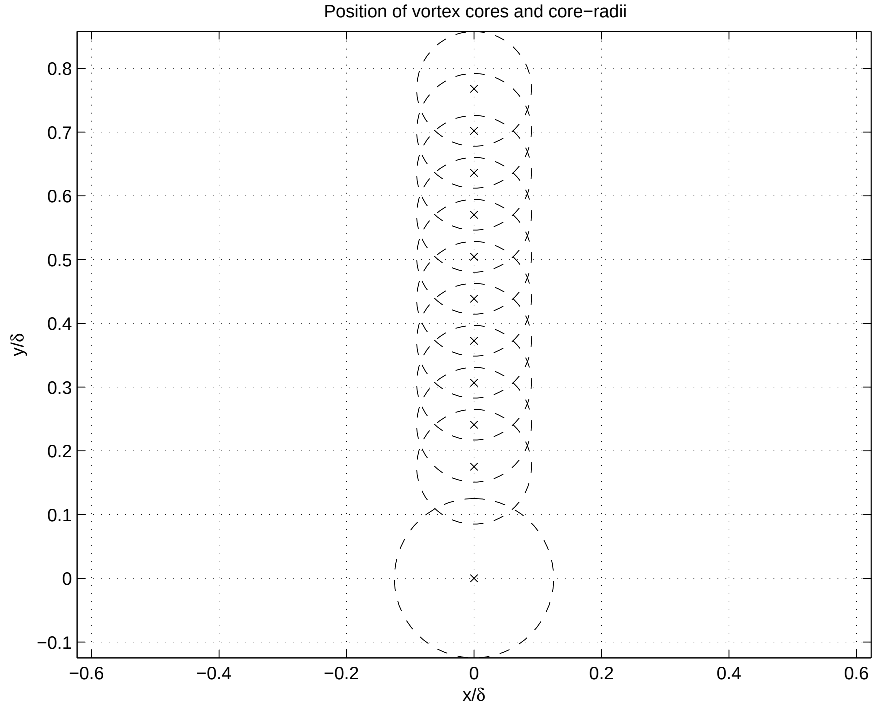

Figure 5.7: Position of the vortex elements from the wall at the initial condition and their relative core-sizes.

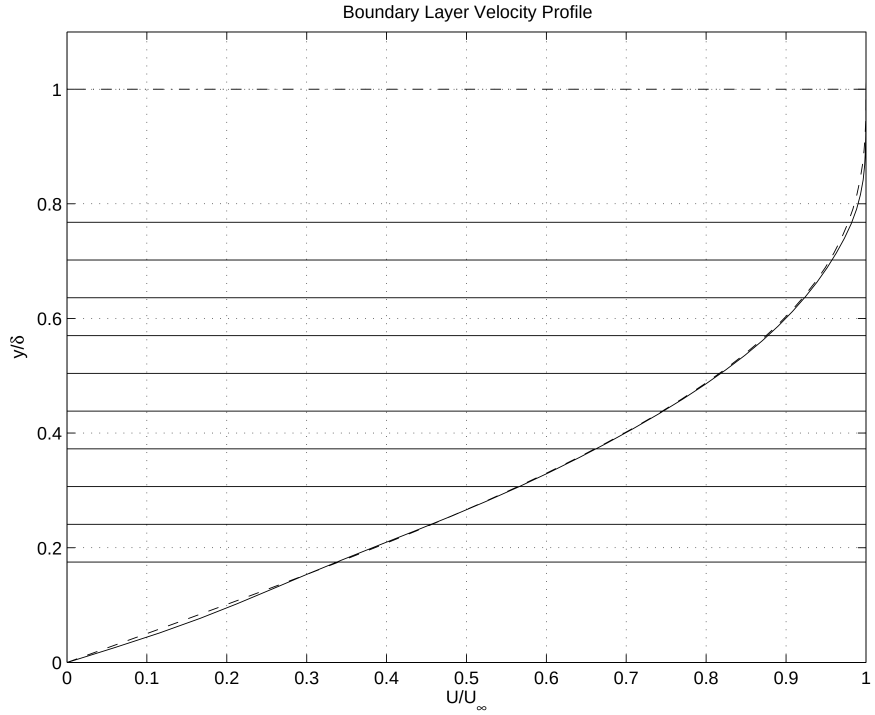

Figure 5.8: Boundary layer velocity profile obtained using the GA (solid), and from the Polhousen approximation to the Blasius boundary layer profile (dashed), defined as $u/U_\infty = 2y - 2y^3 + y^4$. The horizontal solid lines represent the vertical position of the vortex cores at the initial condition.

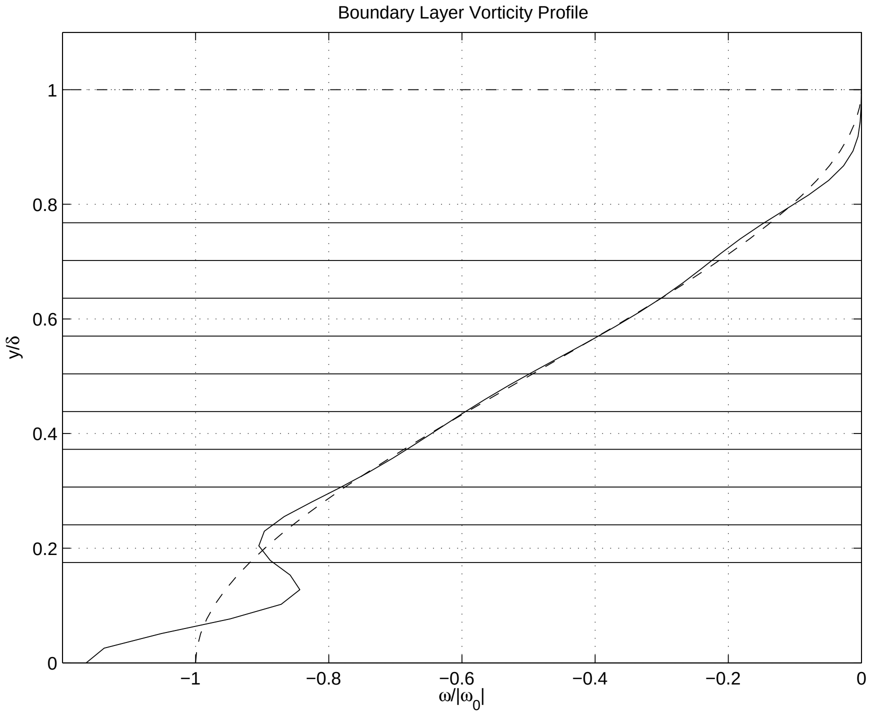

Figure 5.9: Boundary layer vorticity profile obtained using the GA (solid), and from the Polhousen approximation to the Blasius boundary layer profile (dashed). The horizontal solid lines represent the vertical position of the vortex cores at the initial condition.

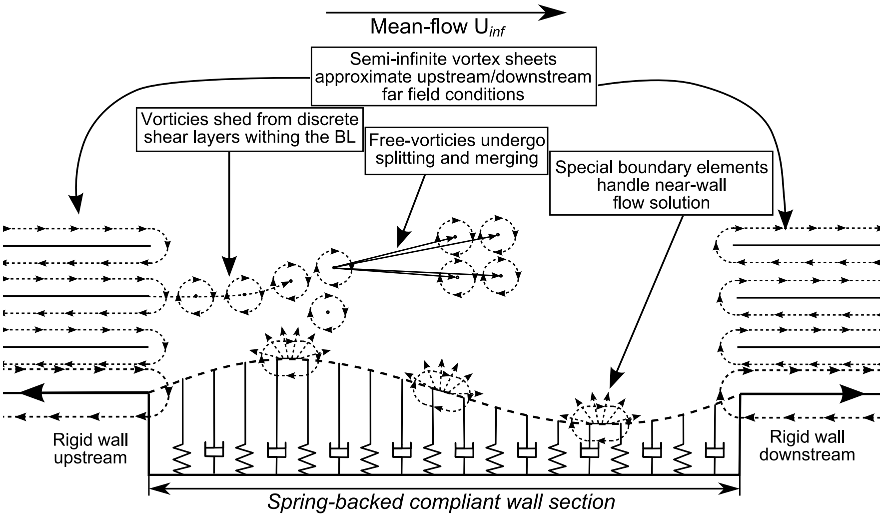

Figure 5.10: Schematic diagram of the totally constructed flow field using the various computational elements.

Chapter 6

Numerical experiments with the CCSVM

6.1 Introduction

This chapter presents results of various simulations performed using the CCSVM. Firstly, some results illustrating the validation of the CCSVM for modelling diffusive rotational flows are shown. Once, the validity of the model is established, some results of the full boundary-layer/compliant wall model are presented.

These results do not present, nor are intended to be, an exhaustive study. Rather, the study focuses on the response of an initial disturbance in a fluid-structure configuration that is shown theoretically to give drag-reducing properties. The results are intended to demonstrate the successful application of the computational method presented in Chapter 5 to achieve qualitative and some quantitative information on a particular FSI interaction problem. An exhaustive parametric study to establish the broader validity of the method along with more general application to FSI problems is a vast field of study and is left for further work.

6.2 Validation of the CCSVM

Presented below are some validation results of the CCSVM model. Two validation models are investigated, the first is the diffusion of a single point vortex in an unbounded flow. The second is the generation of a starting vortex in the wake of an accelerating airfoil.

The diffusion of a single point vortex with *no convection* is useful for investigating the validity of the diffusion modelling and the core-splitting and merging algorithms. Diffusive modelling is primarily where the CCSVM differs from other vortex methods, therefore the validity of the solution of highly diffusive flows such as this should test the methods accuracy for diffusive modelling.

The generation of a starting vortex in the wake of an accelerating airfoil tests a further two important factors of the CCSVM. Firstly, this validation model will include an instance of the boundary element method. The accuracy and stability of this boundary element model can be tested here. Secondly, the flow is highly convective and will allow a validation of the convective solver of the CCSVM to complement the diffusive validation that is obtained through the modelling of a single point vortex.

6.2.1 Diffusion of a single point-vortex

The solution of a single point vortex in a water-type fluid where $\rho = 1000 kg/m^3$ and $\mu = 1 \times 10^{-3} N.s/m$ was calculated using typical calculation parameter values. The critical parameter values for the diffusive modelling are α and β. α corresponds to the core size of the newly created vortices after a splitting event, it is the core size as a proportion of the maximum core size. The parameter β is the primary parameter for the merging algorithm. β corresponds to the minimum separation distance between two cores before they are merged into a single core, it is the separation distance as a proportion of the maximum allowed core-size.

Time evolution of vortex diffusion

As a first test, the calculation parameters were set $\alpha = 0.8$ and $\beta = 0.2$. In this case, $\alpha = 0.8$ is a typical value that will be used in later simulations. However, the low value of β results in a dense distribution of vortices and this parameter setting would probably not be ideal for computational efficiency in boundary layer modelling. The simulation was allowed to run its course and the actual discrete vortex positions, as well as vorticity distributions, and velocity distributions were plotted at various times. The results of the simulation is presented in Figure 6.1.

From left to right, the three columns show the results for the vortex distribution, vorticity and y-component of velocity along the x-axis respectively. The four rows from top to bottom correspond to the results achieved at times $4, 14, 34$ and $59 \times 10^{-4}s$ respectively. For the vorticity and velocity plots, the exact solution of the diffusive term of the Navier-Stokes equation is plotted for comparison with the results obtained through the CCSVM.

It can be seen that between times 4 and 14, the initial vortex core has spread to its limit and therefore split into four vortices that approximate the first (with random orientation). Between times 14 and 34, these four vortices have grown in core size to their limit and split again. However, in this splitting event, some vortices were created in close proximity to others so the vortex merging algorithm begins to combine these close vortices back into one. For this reason there is 15 rather than 16 vortices. Finally, at the latest time, many splitting and merging events have occurred and the vortices becomes very randomised in their distribution.

It can be seen that at all time steps, due to the low value of β, there is a good agreement between the exact theoretical result for the vorticity and velocity distribution, and the result obtained through the CCSVM. The vorticity distribution is more sensitive than the velocity distribution because of the integral relation that exists between these two.

Final distribution for varying values of β

Figure 6.2 presents the results for the final time-step result of the calculation presented in Figure 6.1. In these results the calculation parameter β varied from 0.4 to 1.0 in steps of 0.2 from top to bottom.

As mentioned above, the parameter β corresponds to the minimum separation distance between two (or more) vortices before they will be merged into a single vortex. Varying this parameter adjusts the density of the final vortex distribution, and hence the ‘resolution’ of the computation. As can be seen in the results, lower values of β result in a higher density of vortices and therefore higher accuracy of the solution whereas higher values of β have the opposite effect.

For lower values of β the vorticity distribution becomes less accurately approximated by the CCSVM. Another critical effect that is not seen in these figures is that the distribution begins to shift randomly as the vortices are more sparsely distributed and random motion has a greater effect on the distribution.

6.2.2 Lift on an Airfoil and Wake

We will first present the results for a aerofoil that is not shedding a DVM wake. After, the testing of the various methods of introducing vortex blobs will be carried out.

Aerofoil Discretisation

For the discretisation of the aerofoils into a set of N panels, the MATLAB code of Marchman[1] was used. Although the discretisation could be done a variety of ways, the method of Marchman increases discretisation near the leading and trailing edges where more resolution is required to handle the higher velocity gradients found there.

---

[1] Code available at: http://www.aoe.vt.edu/ marchman/software/index.html

Steady-state Airfoil (zero-wake)

As a validation of the first-order panel method that will be used in this investigation, the results are presented below for a NACA 2412 aerofoil that does not shed vortices and has a trailing-edge Kutta condition applied. These results can be validated against other code, such as Xfoil[2], and other documented experimental results from Katz and Plotkin [42] and Abbott and Von Doenhoff [2].

The NACA 2412 section profile can be seen in Figure 6.3. The corresponding calculated pressure distribution (presented non-dimensionally as the coefficient of pressure) for angles of attack of 0°and 5°, obtained through the computational method discussed above and also results obtained from the code of Marchman, are shown in Figure 6.4.

Table 6.1 gives the values of lift coefficient for both the codes. The results show an excellent agreement between both codes. For the 5°angle of attack there is a slight difference between the two for the peak pressures obtained near the leading edge. This is most likely due to the fact that the Marchman code uses zero-order source/sink panels to enforce the no-flux, and vortex panels to enforce the Kutta condition. The code developed in this work uses first-order vortex panels to achieve both the no-flux and Kutta boundary conditions.

Table 6.1: Comparison of Lift Coefficients for 0 and 5°angles of attack using the BEM developed in this thesis and that of Marchman

Attack Angle (degrees)	C_L	C_L (Marchman)	% diff
0	0.2535	0.2497	1.52%
5	0.8477	0.8493	0.02%

DVM wake model

In this study the airfoil that was modelled in Section 6.2.2 will be modelled in a transient state following an impulsive start. In order to capture the transient dynamics, discrete vortex elements will be shed from the trailing edge in order

---

[2] Xfoil [1] - Open Source Subsonic Airfoil Development System (http://web.mit.edu/drela/Public/web/xfoil/)

to capture the formation of the starting vortex and subsequent convection in the wake of the foil.

The same BEM that was used in Section 6.2.2 will be re-used here and only the free-stream wake vortices, and necessary boundary conditions, will be added to the domain. The parameters used for this simulation are the same as in Section 6.2.2, with time-step size $dt = 10 \times 10^{-3}s$, and an angle of attack of 5°.

Boundary conditions that are applied are:

1. zero total vorticity in the computational domain at all times;
2. a new discrete vortex is inserted at the trailing edge at each time step; and
3. the new vortex enforces the Kutta condition at the trailing edge.

Figure 6.5 shows the position of the actual discrete vortex elements with respect to the airfoil Section at the time $t = 3s$. The formation of a starting vortex is clearly visible and its rate of convection matches the mean-flow speed of $5m/s$.

Figure 6.6 shows the coefficient of pressure distribution at various times after the impulsive start of the airfoil. The results show that the pressure coefficient distribution is asymptoting towards the steady state value that was plotted in Figure 6.4.

6.3 Investigations of drag over compliant surfaces

Some numerical results of the fully coupled DVM boundary-layer/compliant wall system are presented. As is mentioned in Section 6.1, the results presented in this section are not intended to be exhaustive. Rather, a case-example of a theoretical drag-reducing compliant panel configuration is chosen. The results show the development of this compliant wall throughout time from some initial disturbance on the wall.

From this initial disturbance, results are presented illustrating the variation in wall position, fluid shear stress at the wall (directly proportional to drag) and wall energy with respect to time for various amounts of structural damping.

6.3.1 Initial Conditions

The FSI system was initially disturbed by a set deformation on the wall. This was done so that calculation time was not wasted waiting for disturbances to grow from a flat plate. The initial disturbance on the wall is the same as that described in Section 4.4 which was used in the non-linear potential flow study. The disturbance is a piecewise continuous function of displacement which is described by Equation 4.2.

Initially, the boundary layer is set as a homogeneous shear layer above the compliant wall. The homogeneous shear layer has the same profile as the Blasius boundary layer profile that is set as the upstream, inlet boundary condition for the flow. In this respect the growth profile of the boundary layer is initially ignored, meaning that there will be a period of time where the boundary layer will adjust toward a downstream-thickening profile. However the flow parameters are such that the boundary layer growth over the length of the compliant wall section is in the range of 5-10%, therefore adjustments will remain relatively small with respect to the mean boundary layer profile.

6.3.2 Calculation Parameters

The parameters used for this simulation are based on theoretical drag-reducing compliant panels. The wall-based parameters are similar to those used in Section 4.4, the primary difference being the addition of several boundary layer parameters.

In dimensional form, the wall properties correspond to: a thickness of $h = 2\times10^{-3}m$, density $\rho_w = 952kg/m^3$, Youngs modulus of $E^* = 5.0\times10^5 Pa$, flexural rigidity of $B = 3.33 \times 10^{-4} Nm$ and a length of $L = 0.1m$. The backing springs have a stiffness of $K = 90\times10^6 N/m^2$. The various amount of structural damping that were used were $0, 5000, 20000$ and $50000 Ns/m^2$.

The flow properties correspond to: a mean-flow velocity of $U_\infty = 10m/s$, a dynamic fluid viscosity of $\mu = 9.5 \times 10^{-3} Pa.s$, fluid density of $\rho = 950 kg/m^3$, and an inlet blasius boundary layer displacement thickness at the upstream boundary of $\delta^* = 4 \times 10^{-3} m$

The time step size is $dt = 1 \times 10^{-5} s$ and the snapshots of wall positions (and shear stresses) shown in Figures 6.7-6.16 give snapshots at time steps $23, 163, 230$ and 298 respectively from top to bottom. The wall is released from its initial position at time $23dt$.

For the inviscid case, these parameters give a value for the dimensionless parameter Λ^I defined in Equation 4.1 of 53.8. This is below the divergence onset flow speed which can be seen in Figure 4.12 corresponds to a value for Λ^I of approximately 130. The flow speed therefore is sub-critical with respect to divergence onset.

6.3.3 Simulation Results

Figure 6.7 shows the physical position of the various computational elements for a typical simulation using the CCSVM. In the early time-steps, the vortices maintain a regular orientation as they are positioned this way for the initial conditions. After several timesteps the vortices undergo some splitting events and the positioning of the vortex elements becomes randomised. It is interesting to note that the Blasius boundary layer profile can be seen in the pattern created by the vortex elements near the upstream edge of the panel. This is a result of the velocity gradient at the upstream boundary, and certain vortex elements travel further before undergoing their first splitting event. The fact that this pattern resembles the Blasius boundary layer profile serves as another means of validation.

Figures 6.8, 6.9, 6.10, 6.11 show the development of the initial disturbance in the wall position throughout time for identical wall and flow parameters as 6.7, but with wall damping varied as $0, 5000, 20000$ and $50000 Ns/m^2$ respectively. In all cases, the emergence of a downstream wave-packet as well as an upstream travelling wave are observed. The addition of wall damping is seen to attenuate these convective wave packets, particularly the upstream-travelling component.

Figure 6.12 shows the development of the initial disturbance in the wall position for identical wall and mean-flow parameters as in Figures 6.8-6.11, except that the inviscid fluid model of Section 3.2 is used for the fluid modelling.

Figures 6.13, 6.14, 6.15, 6.16 show the development of the fluid shear stress at the wall interface throughout time for same same respective levels of wall damping. The shear stress is expressed non-dimensionally as $\frac{\tau}{\tau_S} - 1$, where τ_S is the shear stress over an equivalent static flat-wall case. A scaled plot of the wall position is superposed for comparison of the shear stress with wall position. In all cases, the shear stress is observed to be 90°out of phase with the downstream travelling wave packet. While for the upstream travelling wave packet, the shear stress is in-phase with the wall position. The shear stress profile also does not follow the sinusoidal shape of the wall disturbance for the downstream-travelling wave packets while the opposite is true for the upstream-travelling wave packets.

Figure 6.17 shows the development of the total wall energies with time for the four cases of structural damping. With increasing damping, the wall tends to become stabilised.

Figure 6.18 shows the total shear stress (per meter width) of the two-dimensional panel for the four levels of damping, along with the results for a static flat-wall for comparison. In all cases, the compliant wall tends to result in higher total shear stress (directly proportional to drag) over the panel.

Figures 6.19 and 6.20 show the wall energy for the energy for the upstream and downstream halves of the compliant panel respectively. Figure 6.19 indicates that the upstream travelling wave packets achieve a neutrally stable state for the case of zero structural damping, while the addition of structural damping attenuates the upstream disturbance in all cases. While Figure 6.20 indicates that the downstream travelling wave is unstable for the case of zero structural damping. The grow rate of this downstream-travelling instability is reduced with the addition of structural damping, however it is only with *heavy* structural damping that the instability is attenuated totally.

Figures 6.21, 6.22 and 6.23 show the variation of position, velocity and pressure with time at various stations along the compliant wall for three levels of structural damping respectively. The plots of the position and velocity of the wall have been scaled with respect to the pressure signal and are presented only for comparison. The three stations from which these measurements are taken are at positions $0.35L$, $0.5L$ and $0.75L$ from the upstream edge of the compliant section. Where L is the length of the compliant wall section.

Figure 6.24 give the results for the exact same mean flow and wall parameters as Figure 6.21 except that the ideal flow model of Chapter 3 is used for the fluid modelling. In this case the boundary layer effects are not modelled as in the DVM boundary layer model.

6.4 Discussion

The results presented in this chapter are presented for the purpose of indicating that the method developed in Chapter 5 can be applied directly to achieve results for a range of problems. They show that the model *can* provide valid and accurate results that are based on the mathematical principles developed in Chapter 5. Some interesting insight into the nature of the FSI system may be attained and are discussed below. While the results presented here indicate that the model is capable of yielding some quantitative and qualitatively correct results, caution should and has been used in the interpretation of these results.

Comparison of the results obtained through the inviscid fluid model of Figure 6.12 and the boundary-layer DVM models of Figures 6.8-6.11 give some insight into the effect that the boundary-layer has on the wall-based instabilities. In all cases involving the boundary-layer model, both an upstream and downstream-travelling distinct wave packets are seen to emerge from the initial disturbance. The energy plots of Figures 6.19 and 6.20 show that the downstream travelling wave is unstable for all but cases of heavy structural damping. Similarly, the upstream-travelling wave front is neutrally stable for cases of zero structural damping. The inviscid fluid model also shows an upstream and downstream wave propagation, however results from Section 4.2 show that the compliant wall is operating in the pre-divergence range of flow speeds. Therefore any disturbance will attenuate and eventually quiesce. These results indicate that the addition of the boundary layer into the modelling introduces a new mechanism for convective instability which destabilises the wall at lower mean-flow velocities than an inviscid fluid model. This type of instability is referred to as travelling-wave-flutter (TWF) and has been identified in theoretical as well as experimental observations. While this is not a new discovery, it does serve to further validate the numerical model in its capability to resolve TWF.

Figures 6.13-6.16 show the spatial variation of shear stress in comparison with wall displacement. These results indicate that for the upstream-travelling wave fronts the shear stress profile is in-phase with and conforms to the shape of the wall displacement. However for the downstream travelling waves, the shear stress profile is 90°out of phase with the wall displacement profile and does not conform to the wall displacement profile in the lee of the wave front. For the downstream travelling wave, the shear stress increases rapidly on the face of the downstream travelling wave until approximately 45°behind the displacement peak. After this sharp increase the shear stress then decreases gradually in the lee of the wave. This asymmetry in the shear stress profile tends to increase the drag over the entire compliant panel in this case. This is further supported by Figure 6.18 which indicates that total drag over the compliant coating is higher for all the cases of compliant walls over that of a rigid wall. This does not indicate that drag reduction through the use of compliant panels is not possible through the tendency of the compliant panel to reduce boundary layer instabilities and delay transition. However, it does indicate that the use of compliant coatings to achieve drag reduction could come at a cost of increased drag over the actual compliant panels. This implies that placing compliant coatings over the entire surface of a body may not be the optimal drag-reducing configuration.

The plot of the total wall energy in Figure 6.17 indicates that instabilities amplify on the compliant wall under the influence of a boundary layer and are only attenuated by heavy structural damping. Further plotting of the wall energies in the upstream and downstream halves, as in Figures 6.19 and 6.20, indicate that the upstream travelling wave is neutrally stable in the limit of zero structural damping. Figure 6.20 indicates that the downstream travelling wave is unstable for a range of structural damping, and is only attenuated with the addition of heavy structural damping. This could have important implications in the design of compliant panels for drag reduction. In this case it would be desirable to use finite-length compliant panels that are relatively short with respect to the growth rate of the downstream-travelling instability. Making the compliant panels longer will allow these convective instabilities to grow to an undesirable point where non-linear and detrimental effects to the drag, such as flow separation, can occur. Making a compliant panel shorter in length means that the downstream edge would stop these downstream-travelling instabilities before they grow to this point, and with the addition of some small structural damping, reflecting and upstream-travelling waves would be attenuated.

The forcing pressure plots of Figures 6.21-6.23 provide information regarding the varying stability between the upstream and downstream parts of the panel. In all cases, the upstream station records a pressure signal that is in-phase with the wall displacement signal (and 90°out of phase with the wall velocity signal). Likewise, the pressure signal is 45°and 90°out of phase with the wall displacement (and 45°and in-phase respectively with the wall velocity) at the centre and downstream stations respectively. These phase differences between the forcing pressure signal and the displacement and velocity signals indicate energy transfers between the wall and fluid.

The noise resulting from the random distribution of the vortex cores may be seen in the pressure signal. For most cases, the variation in the forcing pressure signal due to noise is small with respect to mean-variations in the pressure signal. The noise is significant in the $0.35L$ station of Figure 6.23, however in this case the wall is in a quiescent state and mean-variation of the pressure signal is small.

The results for pressure, displacment and velocity at 3 stations along the compliant wall for the non-linear inviscid fluid model, with no structural damping in the wall model, are presented in Figure 6.24. This result corresponds directly to the boundary layer model result of Figure 6.21. The pressure is in-phase and 180°out of phase with the displacement in the upstream and downstream halves of the panel respectively. At the centre of the panel the pressure signal is slightly out of phase with the displacement signal. The maximum pressures occur at the centre of the panel. The system is inviscid, therefore the convectely unstable wave packets that appear in Figures 6.21-6.23 do not occur. The system is in the pre-divergence range of flow speeds and therefore the wall does not gain energy and grow in amplitude. These factors explain the lower pressure signals at the upstream and downstream stations than are noted in the results involving the boundary layer model.

The numerical methods of the DVM boundary model used to generate the pressure plots in Figures 6.21-6.23 and the inviscid model used to generate the pressure plots in Figure 6.24 are very different. Also, the means of pressure evaluation and coupling to the wall model is derived from different fundamental principles. None the less the pressure signals recorded from the DVM model in Figures 6.21-6.23 and from the inviscid model in Figure 6.24 are similar in magnitude, as well as various qualitative aspects. This similar between the results obtained through the two methods provides a further source of validation for the DVM boundary layer model developed in the present work.

6.5 Conclusions

The results show that the DVM boundary layer model is capable of effectively simulating a FSI with the compliant surface. The results give qualitatively accurate results, through indicating that the no-flux and no-slip conditions are enforced accurately, and that the model is capable of capturing travelling-wave flutter (TWF) type instabilities. A further exhaustive study of the validity of the model is needed before an in-depth parametric study can be carried out. However, some conclusions could still be inferred from the preliminary results obtained in this work.

The results indicated that drag is increased over the length of a compliant panel due to the nature of the shear-stress profile for downstream-travelling instabilities. It may be possible to reduce the total drag on a body through the adoption of compliant panels to reduce fluid-based instabilities and prolong boundary-layer transition. However, this reduction comes at the cost of increased drag over the compliant panels themselves. This indicates that a trade-off might have to be sought between the benefits of transition delay and the cost of compliant panels when it comes to the practical design of compliant panels for drag reduction.

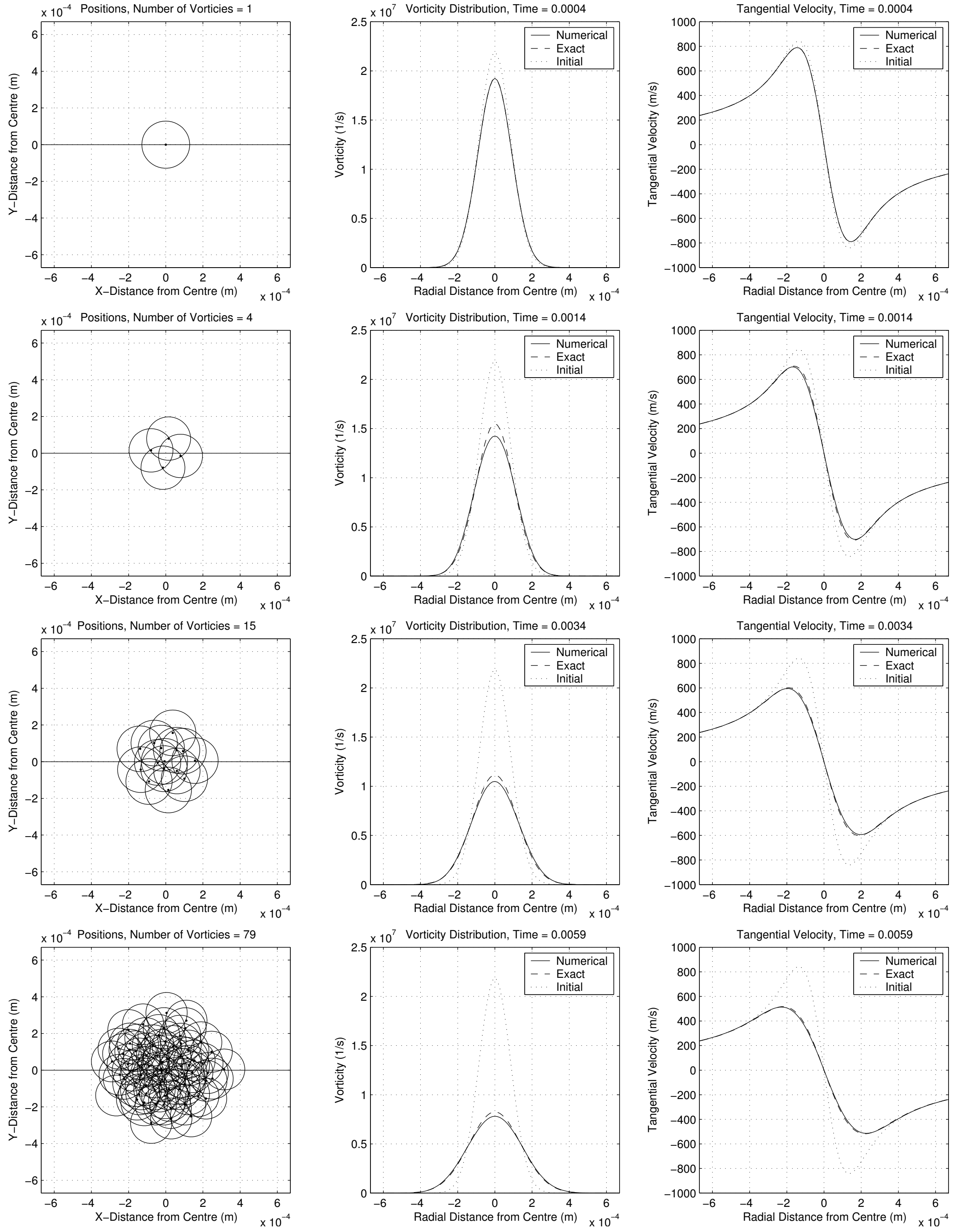

Figure 6.1: Diffusion of a single point vortex with *no convection* in a water-type fluid ($\rho = 1000 kg/m^3$, $\mu = 1 \times 10^{-3} Pa.s$). Results shown are the numerical solution with parameters $\alpha = 0.8$ and $\beta = 0.2$, splitting to four new vortices. And the exact theoretical solution from the diffusion equation. At times $4, 14, 34$ and $59 \times 10^{-4} s$ respectively from top to bottom.

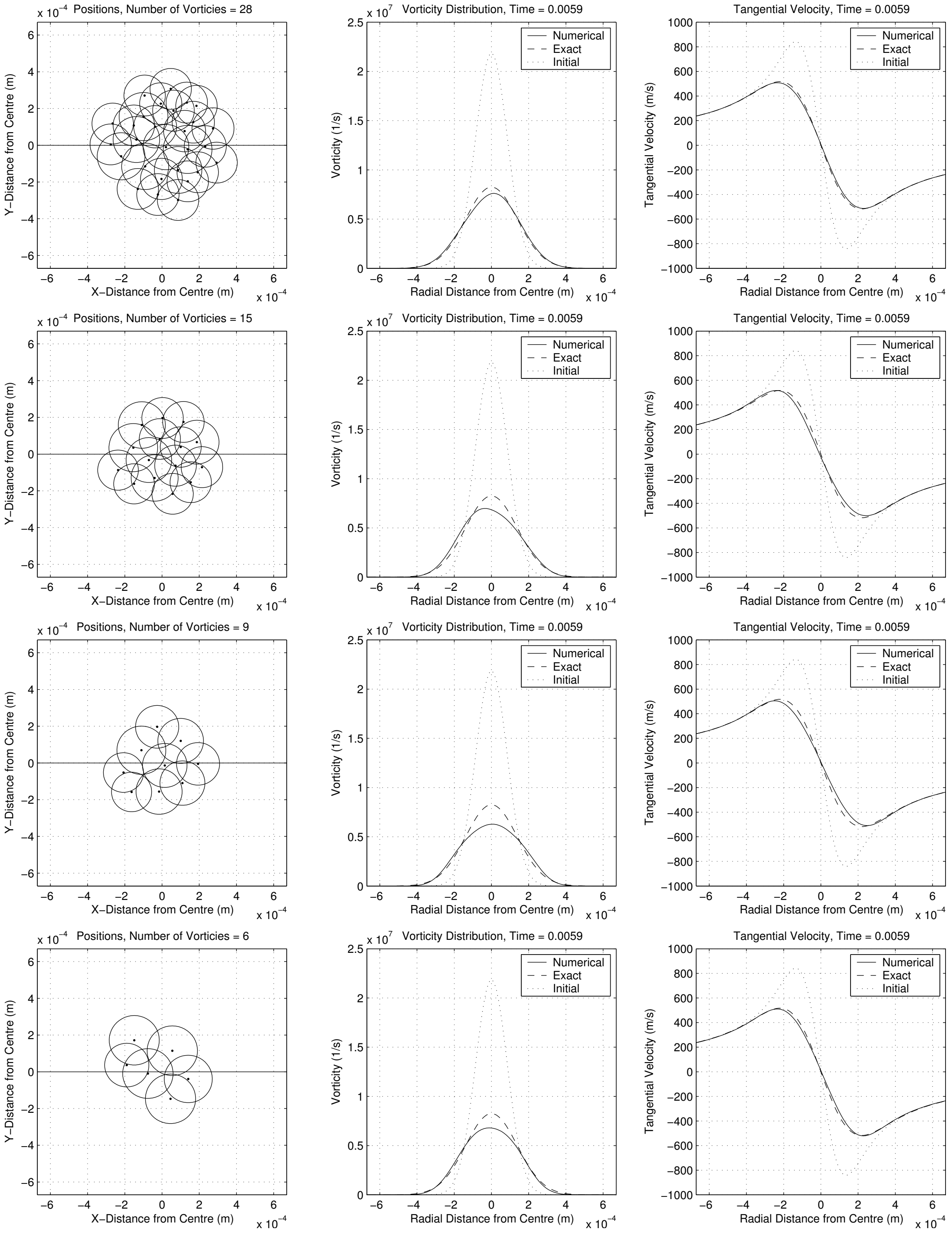

Figure 6.2: Results from the final time-step of the calculation of the diffusion of a single point vortex with parameters the same as in Figure 6.1 but with calculation parameter β varied. From top to bottom $\beta = 0.4, 0.6, 0.8, 1.0$ respectively

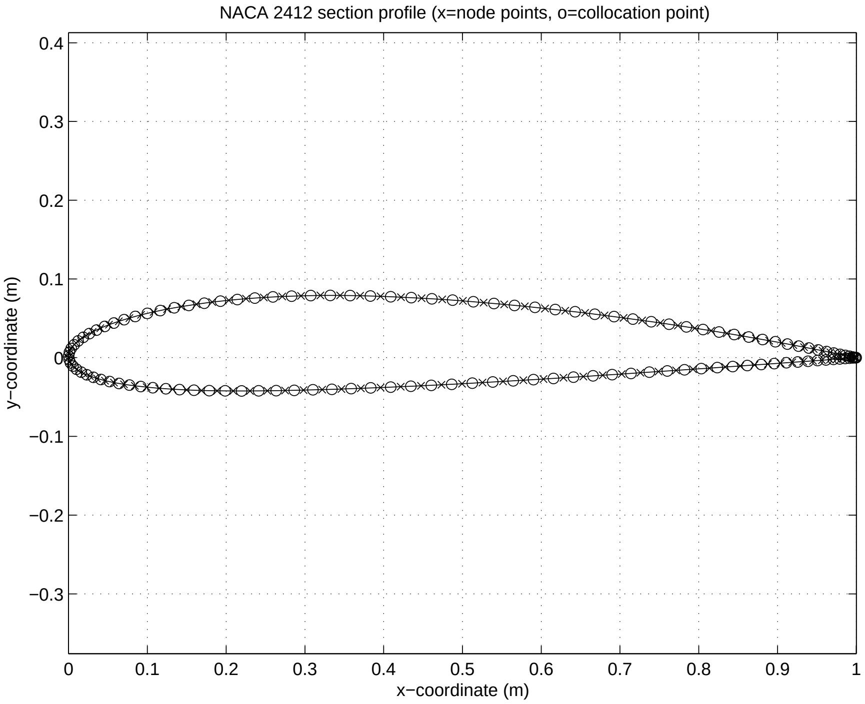

Figure 6.3: NACA 2412 section profile used for validation of the BEM and CCSVM. o = panel control points.

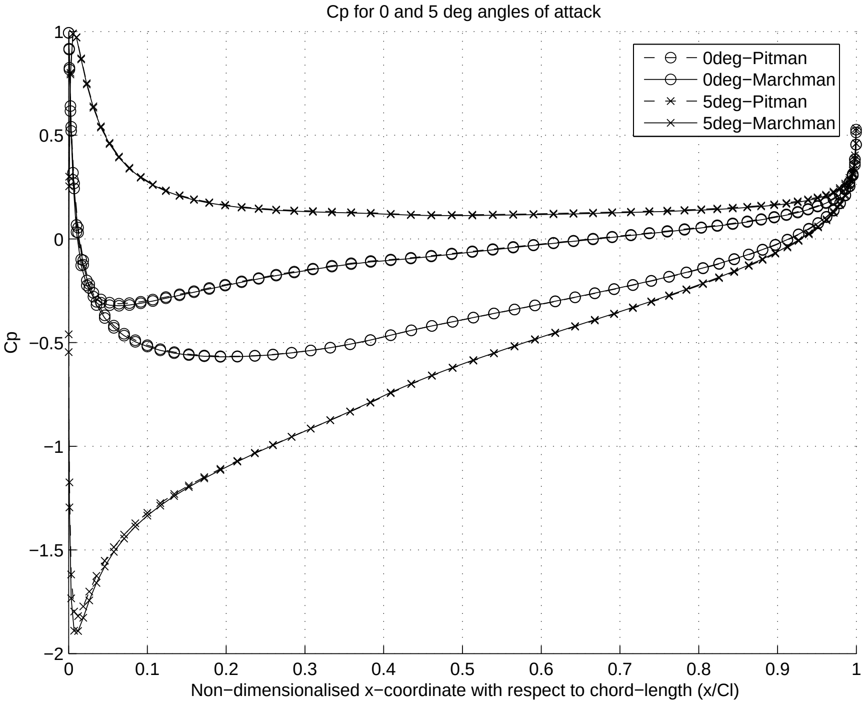

Figure 6.4: Pressure coefficient distribution around the section for angles of attack of 0°and 5°, comparison of results obtained from the BEM developed in this work and Marchman

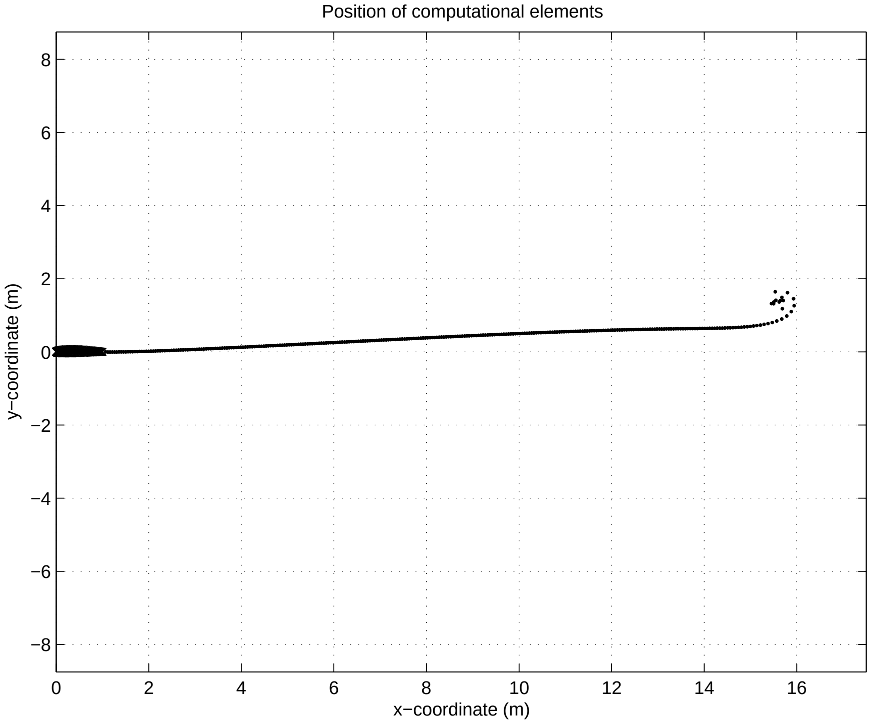

Figure 6.5: Position of computational elements at time $t = 3s$.

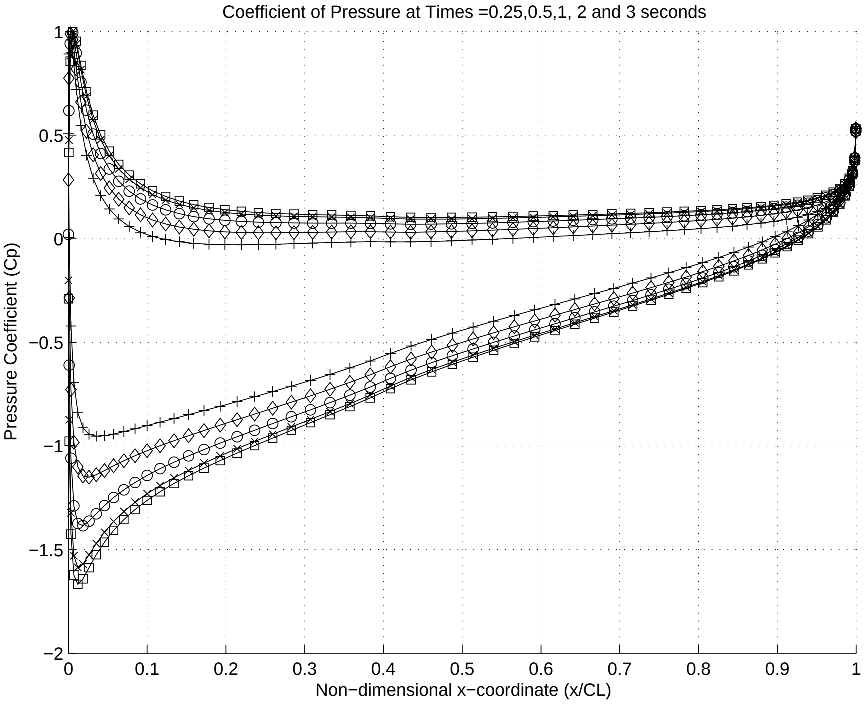

Figure 6.6: Pressure coefficient distribution (Cp) at times $0 < t < 3s$ for a time-step size of $dt = 10 \times 10^{-3}s$

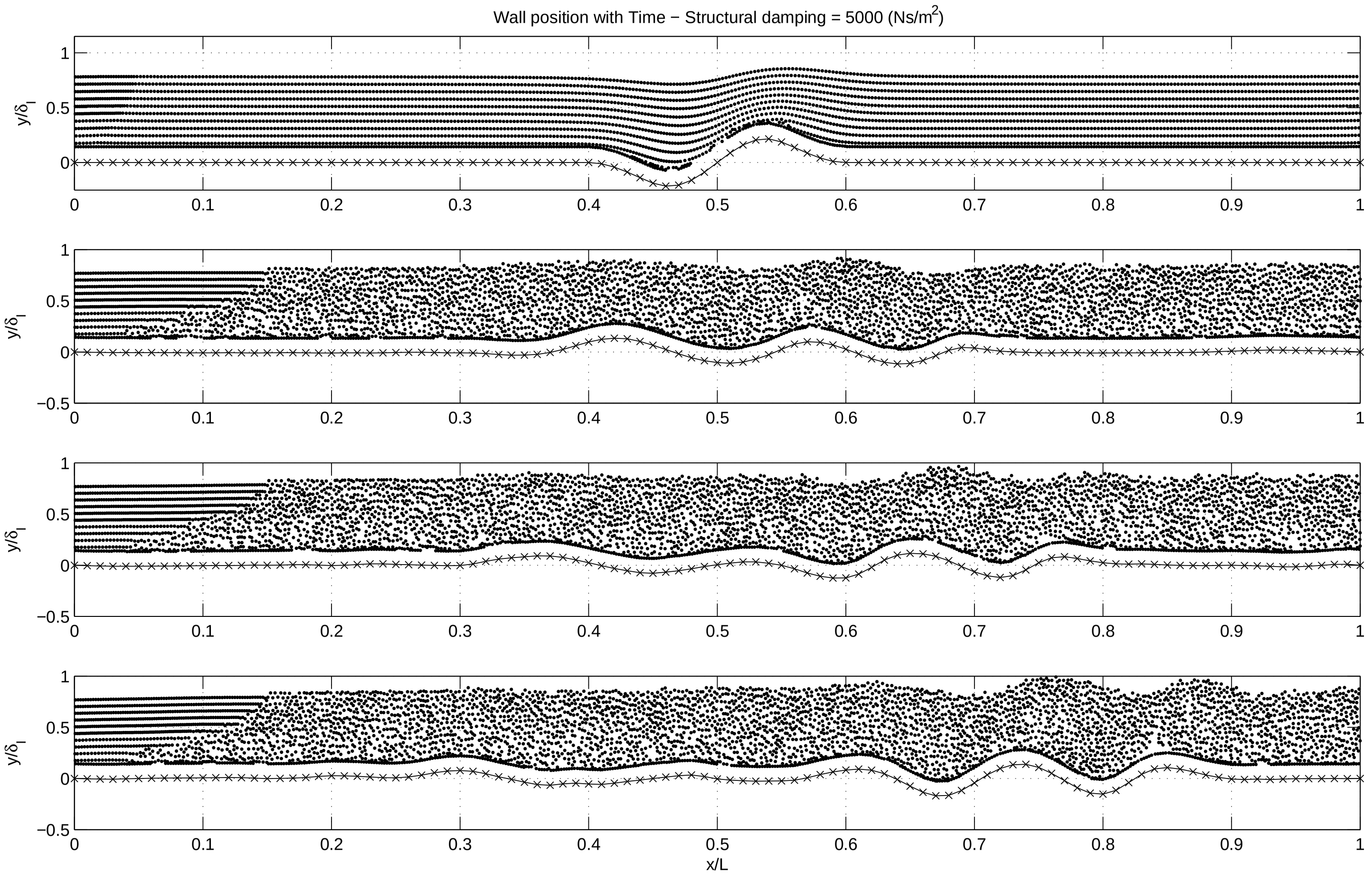

Figure 6.7: Wall and vortex positions at time steps $23, 163, 230$ and 298, respectively from top to bottom, where $dt = 1 \times 10^{-5}s$. For a spring-backed damped wall. The wall is released from its initial position at time $23dt$

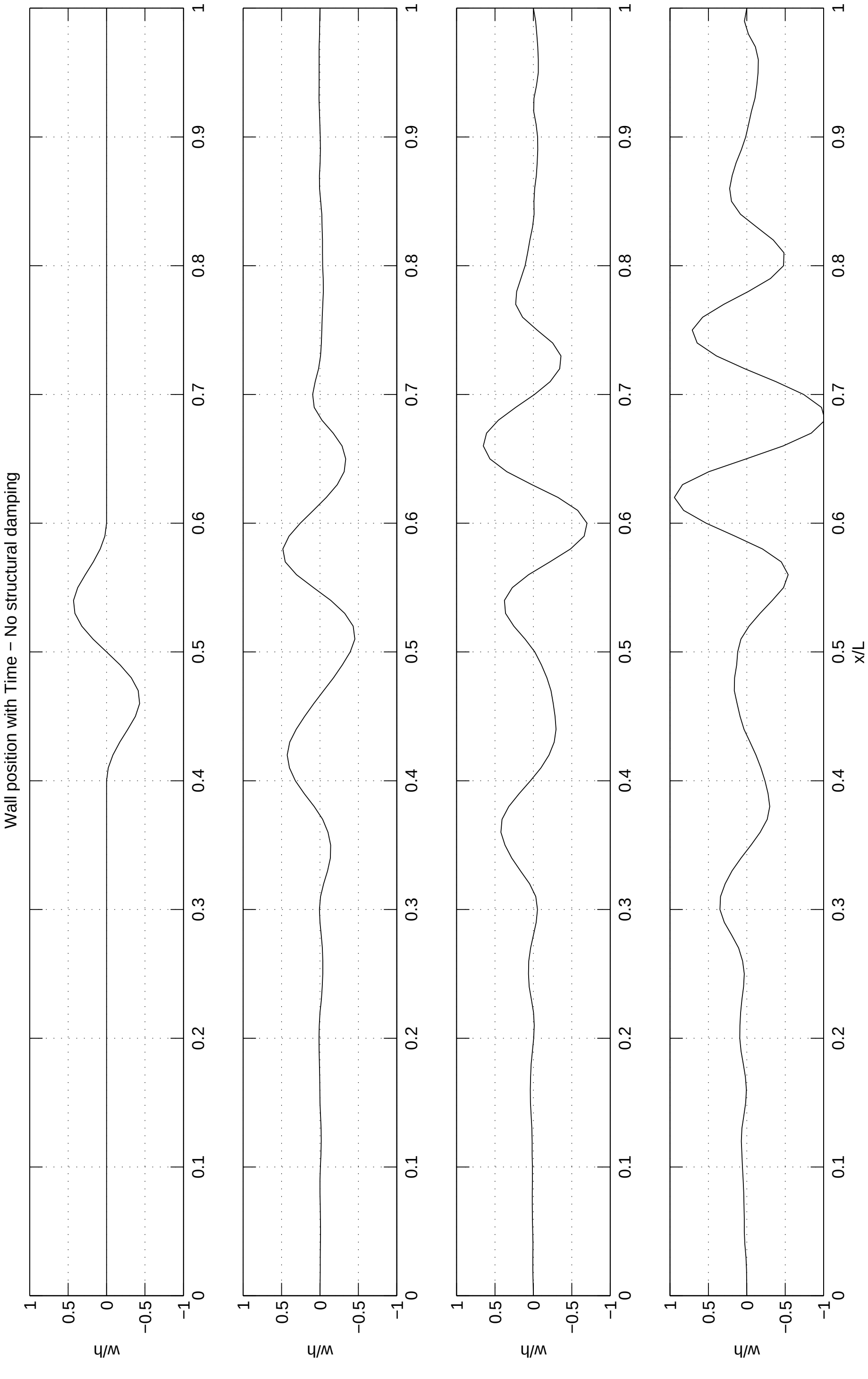

Figure 6.8: Wall position at time steps 23, 163, 230 and 298, respectively from top to bottom, where $dt = 1 \times 10^{-5}s$. For a spring-backed wall with *no structural damping*. The wall is released from its initial position at time $23dt$

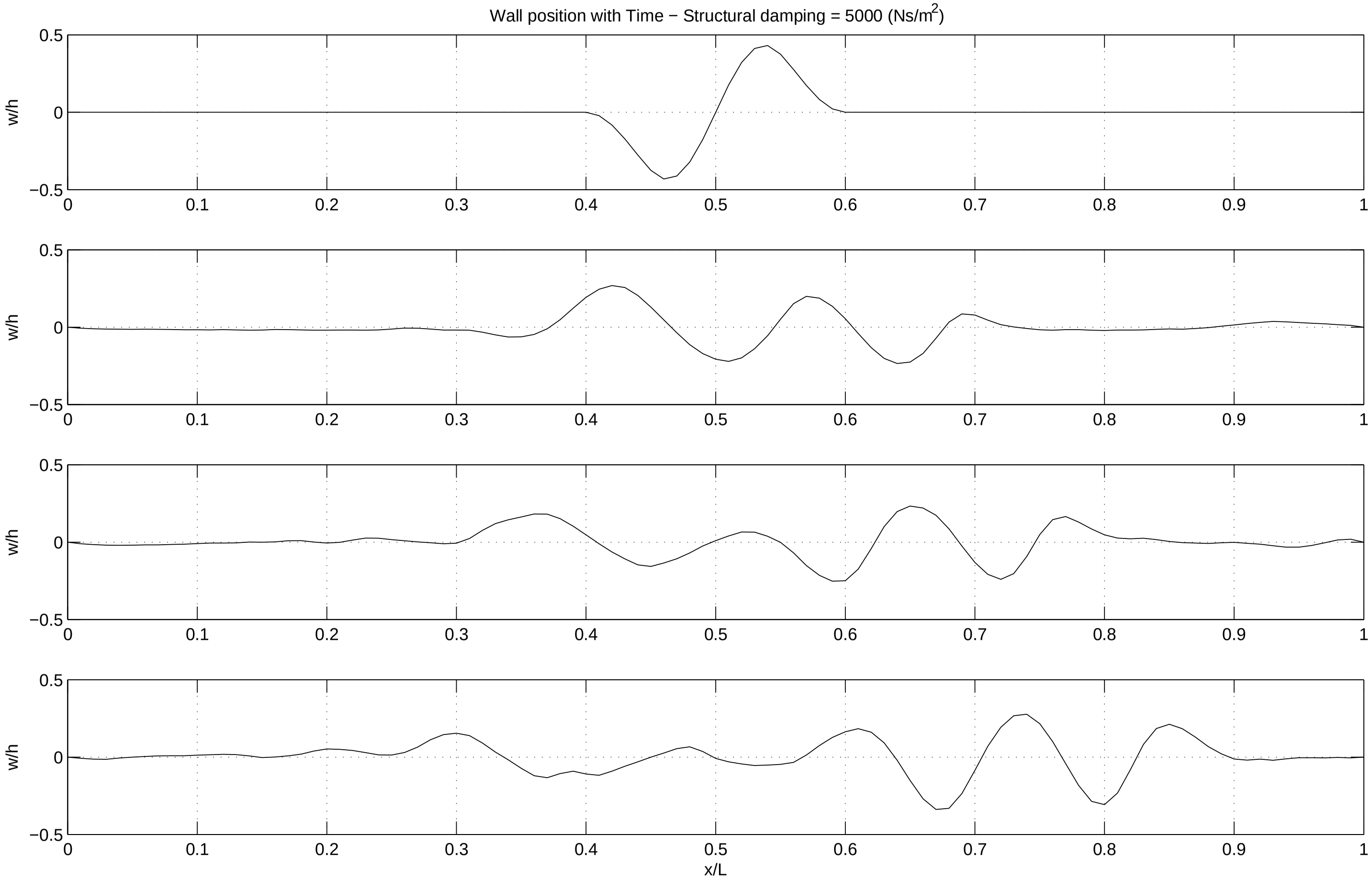

Figure 6.9: Wall position at time steps $23, 163, 230$ and 298, respectively from top to bottom, where $dt = 1 \times 10^{-5}s$. For a spring-backed damped wall, structural damping $= 5000Ns/m^2$. The wall is released from its initial position at time $23dt$

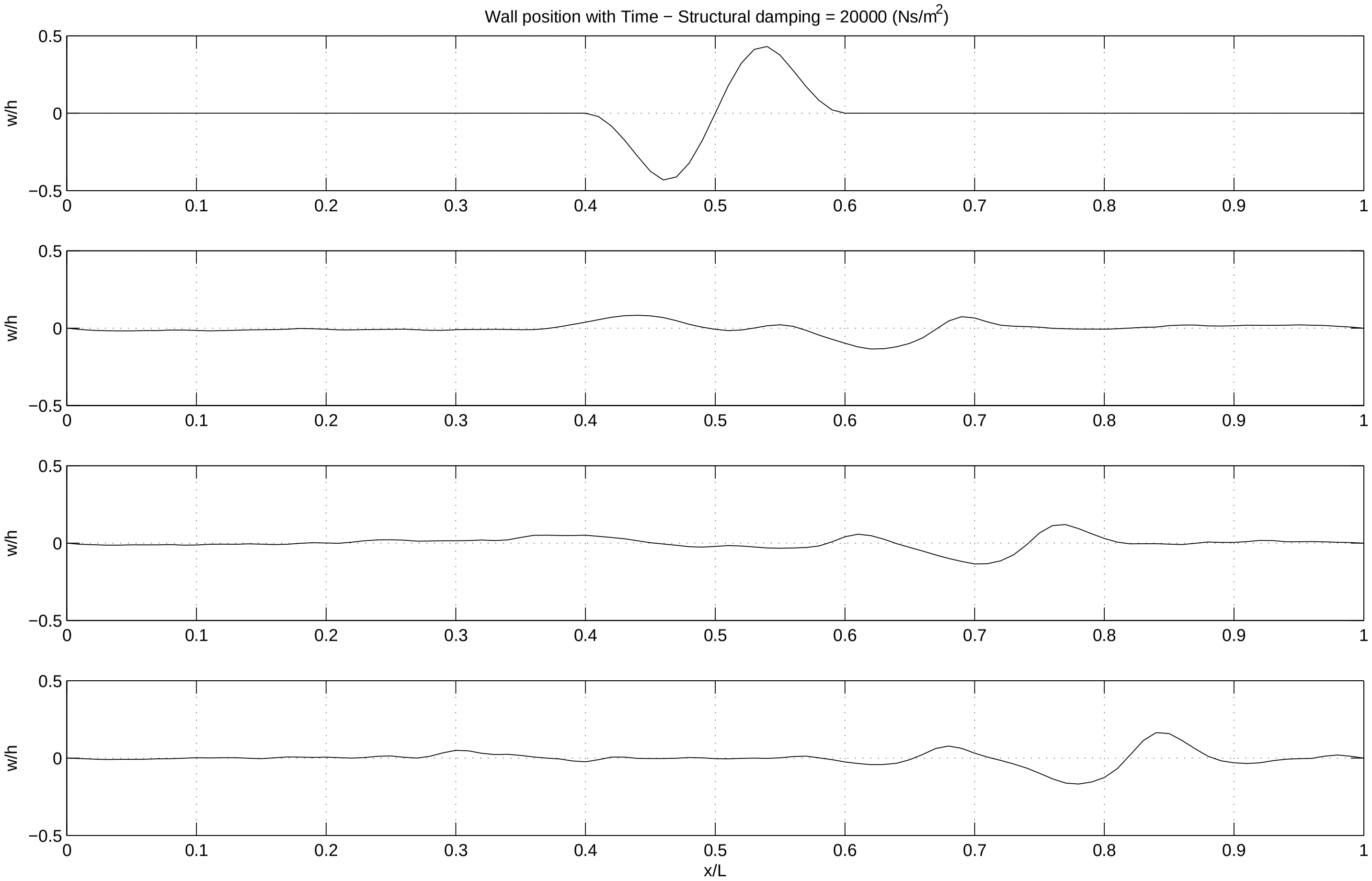

Figure 6.10: Wall position at time steps $23, 163, 230$ and 298, respectively from top to bottom, where $dt = 1 \times 10^{-5}s$. For a spring-backed damped wall, structural damping $= 20000Ns/m^2$. The wall is released from its initial position at time $23dt$

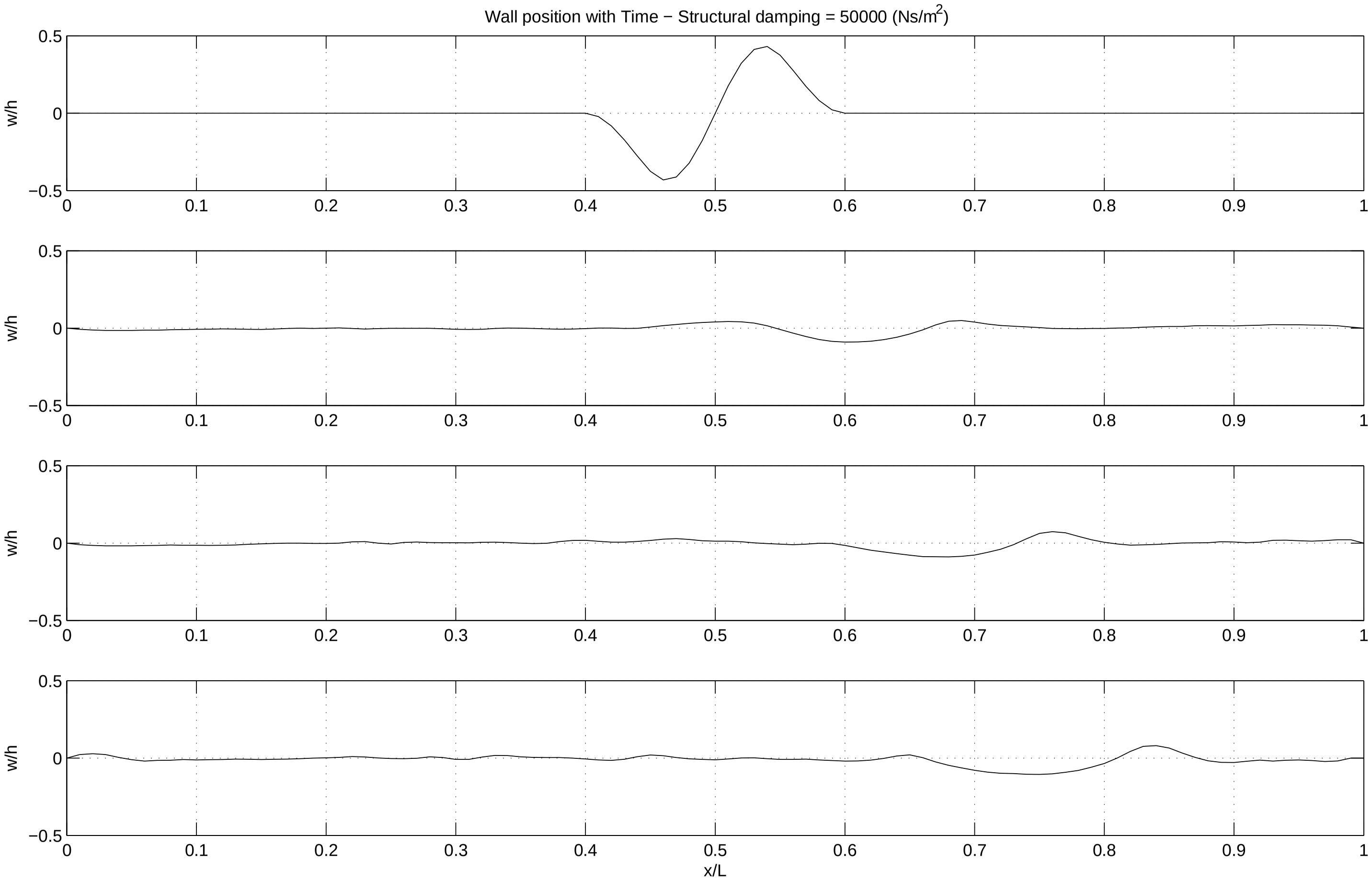

Figure 6.11: Wall position at time steps $23, 163, 230$ and 298, respectively from top to bottom, where $dt = 1 \times 10^{-5}s$. For a spring-backed damped wall, structural damping $= 50000Ns/m^2$. The wall is released from its initial position at time $23dt$

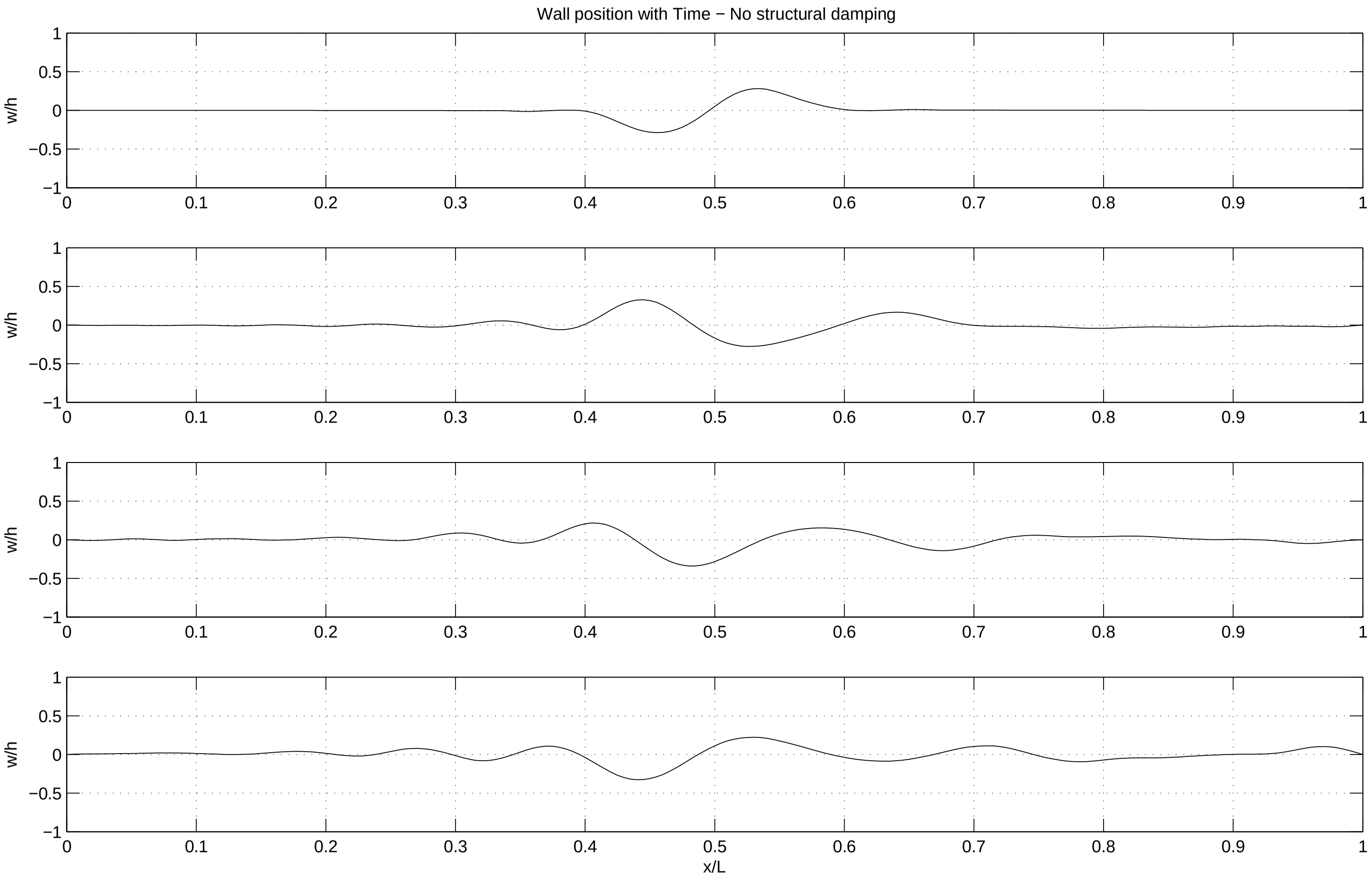

Figure 6.12: Wall position at time steps $23, 163, 230$ and 298, respectively from top to bottom, where $dt = 1 \times 10^{-5}s$. For a spring-backed damped wall with *no structural damping* using the inviscid fluid model. The wall is released from its initial position at time $23dt$

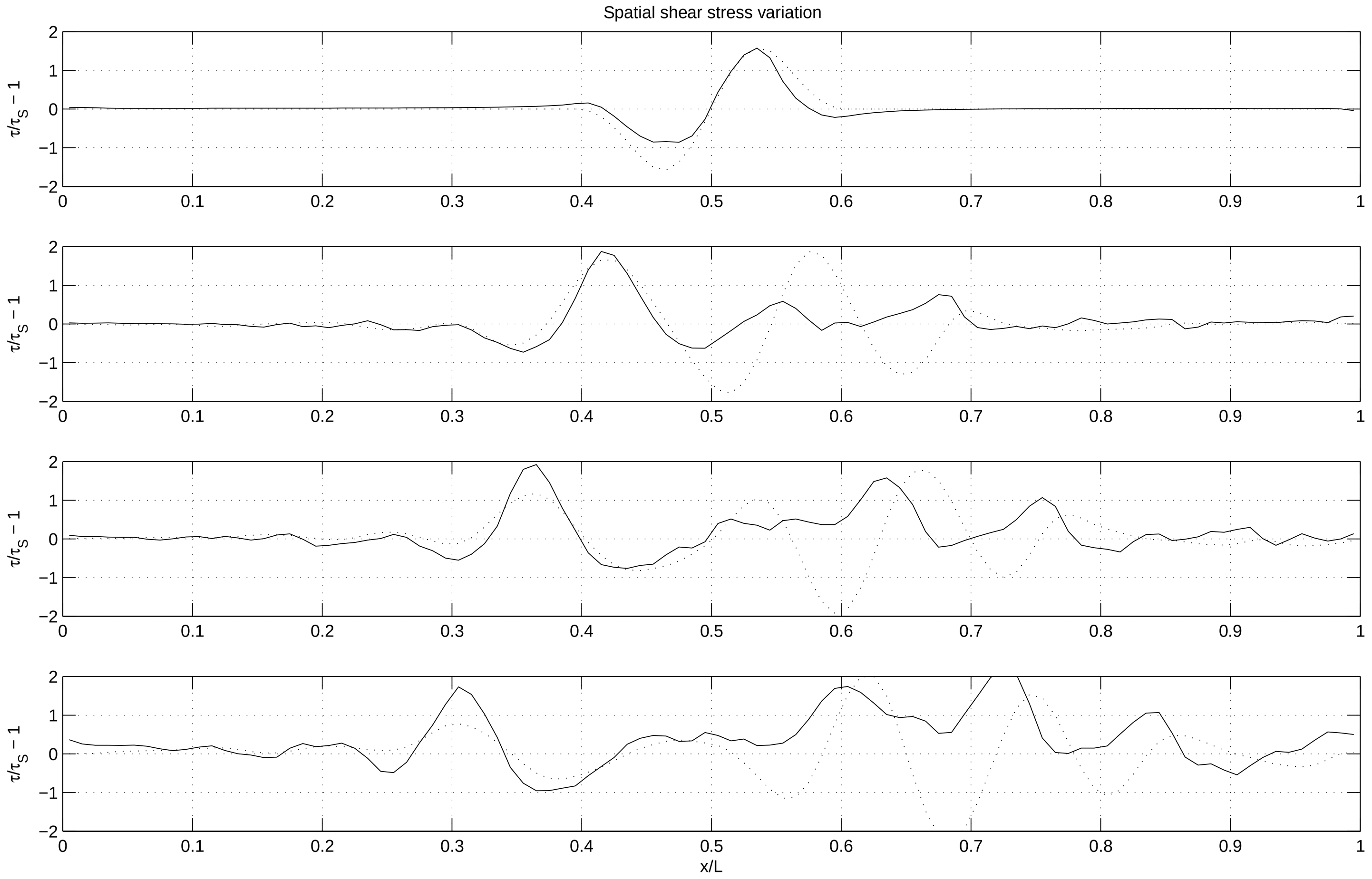

Figure 6.13: Fluid shear stress at the wall, plotted with scaled wall position at time steps 23, 163, 230 and 298, respectively from top to bottom, where $dt = 1 \times 10^{-5}s$. For a spring-backed damped wall, *no structural damping*. The wall is released from its initial position at time $23dt$. The dashed line shows the corresponding scaled wall position for comparison.

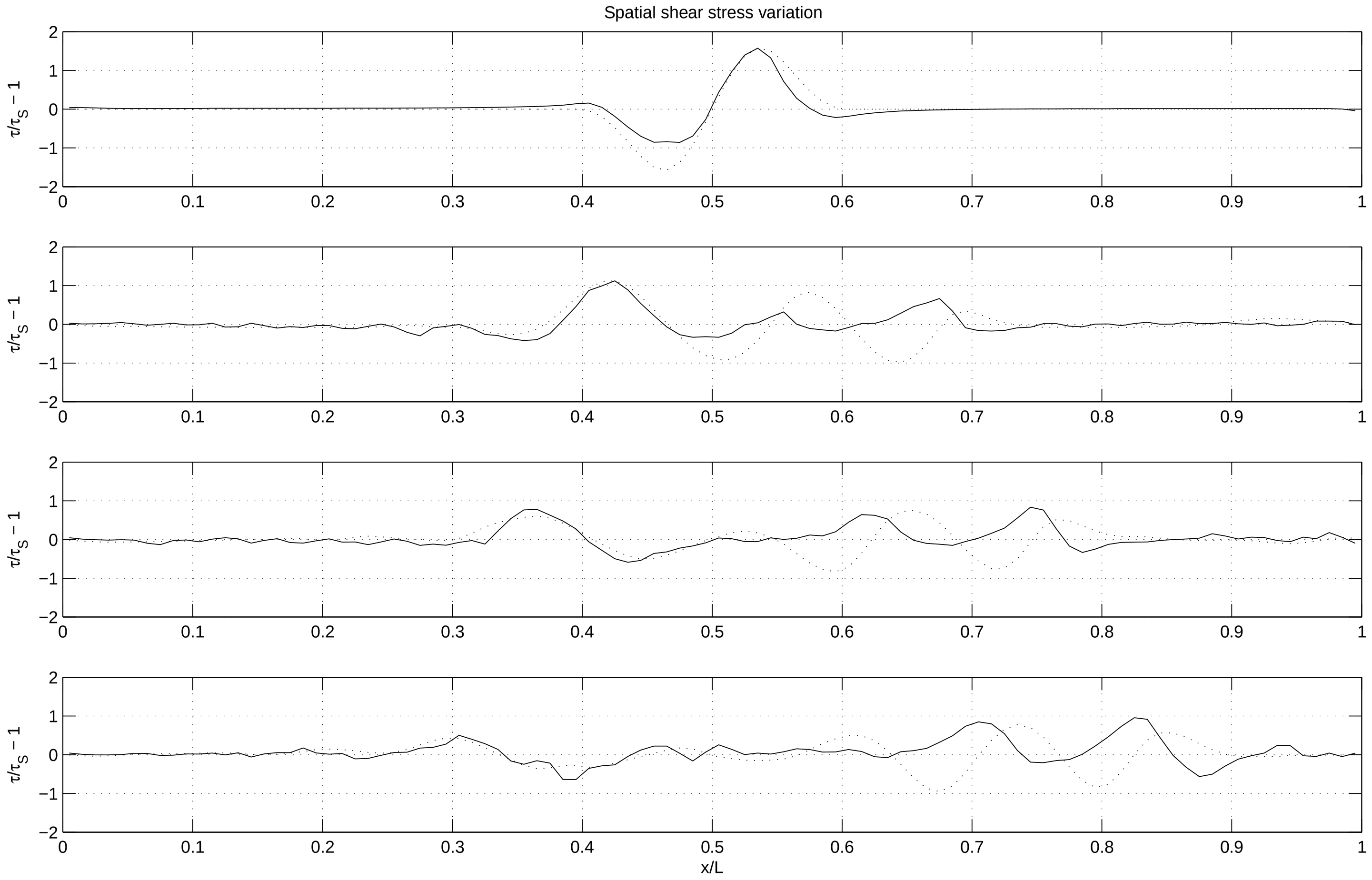

Figure 6.14: Fluid shear stress at the wall, plotted with scaled wall position at time steps $23, 163, 230$ and 298, respectively from top to bottom, where $dt = 1 \times 10^{-5}s$. For a spring-backed damped wall, structural damping $= 5000Ns/m^2$. The wall is released from its initial position at time $23dt$. The dashed line shows the corresponding scaled wall position for comparison.

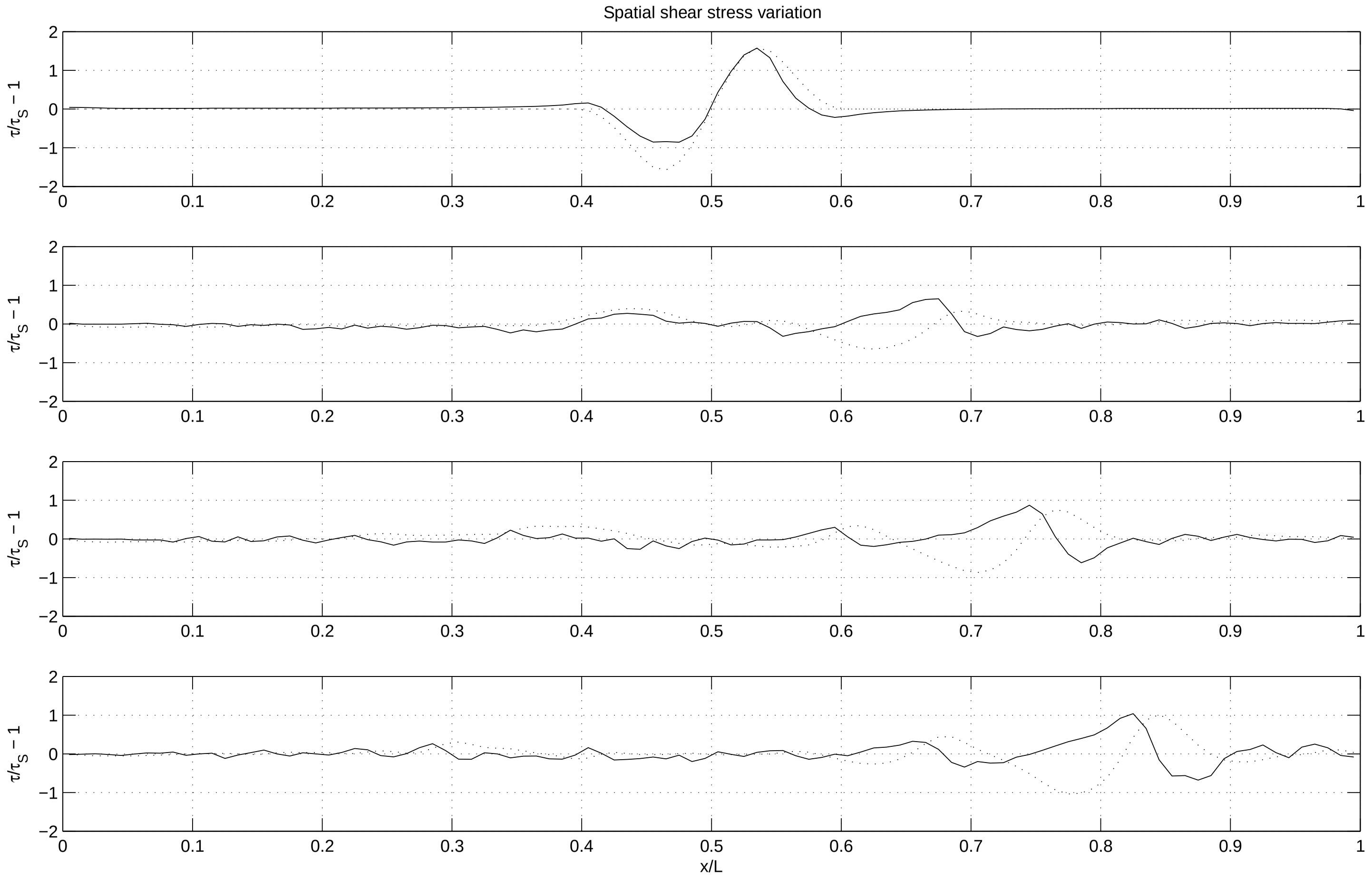

Figure 6.15: Fluid shear stress at the wall, plotted with scaled wall position at time steps $23, 163, 230$ and 298, respectively from top to bottom, where $dt = 1 \times 10^{-5}s$. For a spring-backed damped wall, structural damping $= 20000Ns/m^2$. The wall is released from its initial position at time $23dt$. The dashed line shows the corresponding scaled wall position for comparison.

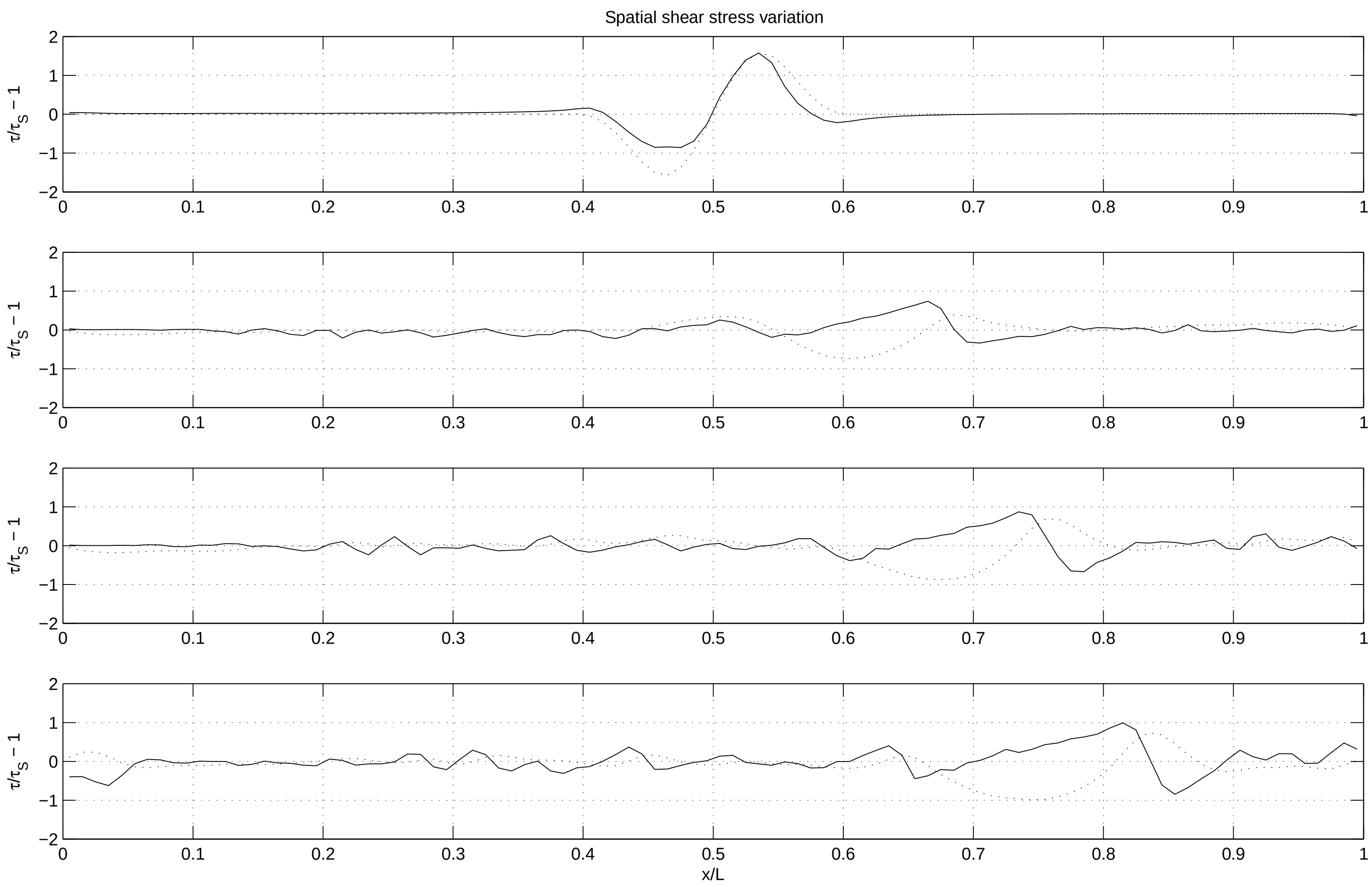

Figure 6.16: Fluid shear stress at the wall, plotted with scaled wall position at time steps 23, 163, 230 and 298, respectively from top to bottom, where $dt = 1 \times 10^{-5} s$. For a spring-backed damped wall, structural damping $= 50000 Ns/m^2$. The wall is released from its initial position at time $23dt$. The dashed line shows the corresponding scaled wall position for comparison.

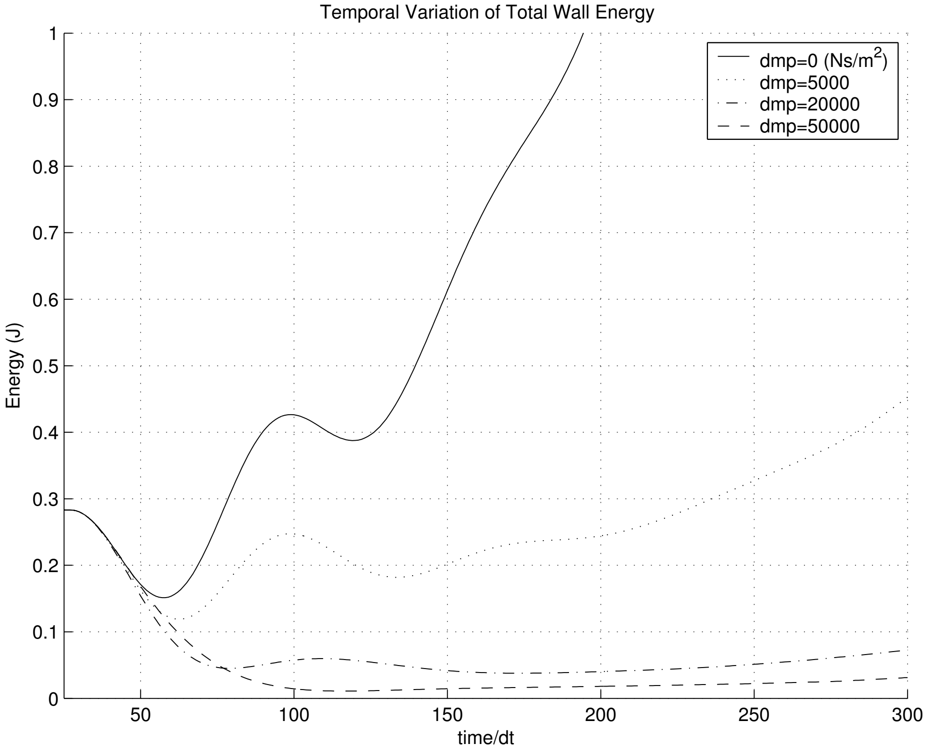

Figure 6.17: Total wall energy variation with time. The wall is released from its initial position at time $23dt$

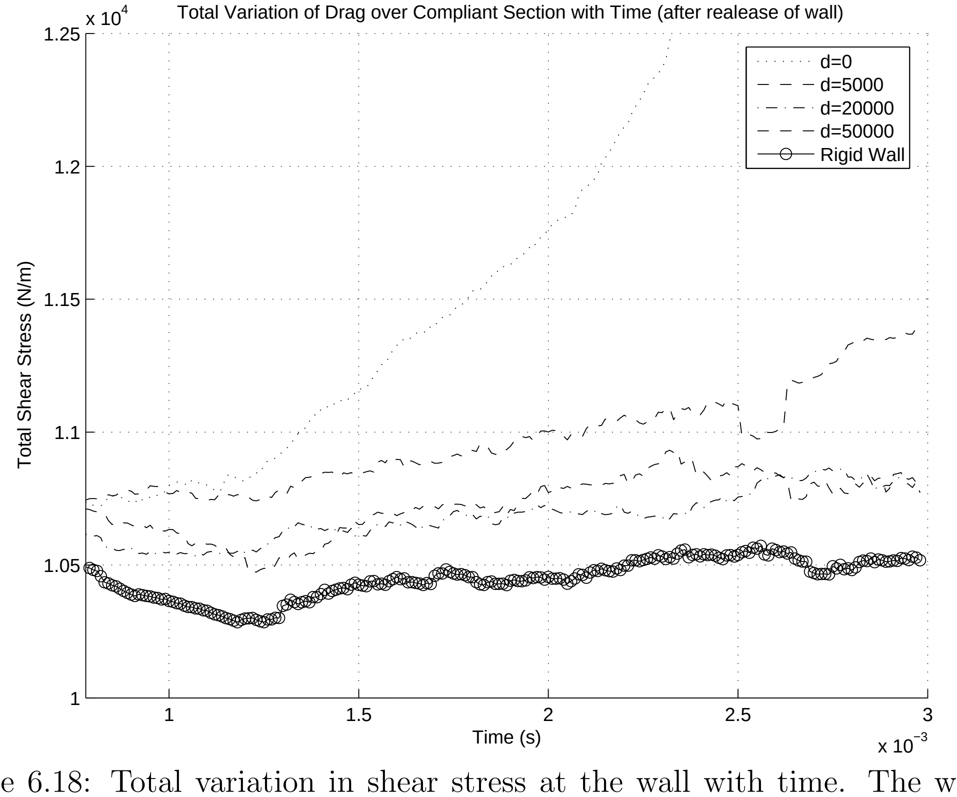

Figure 6.18: Total variation in shear stress at the wall with time. The wall is released from its initial position at time $23dt$

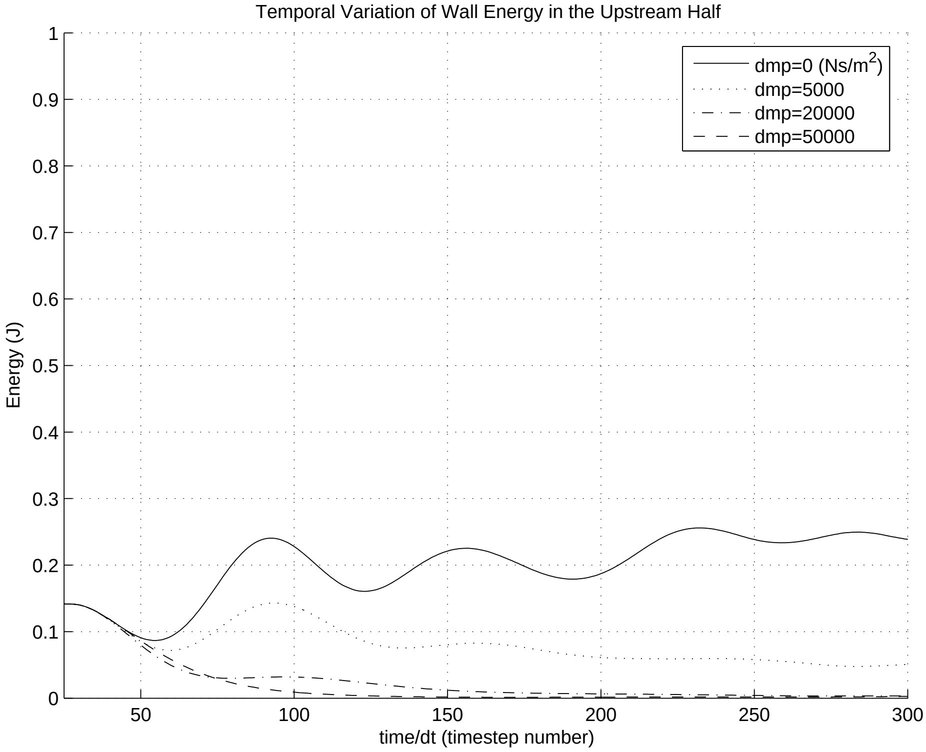

Figure 6.19: Wall energy variation with time for the upstream half of the compliant surface, where $dt = 1 \times 10^{-5}s$. The wall is released from its initial position at time $23dt$

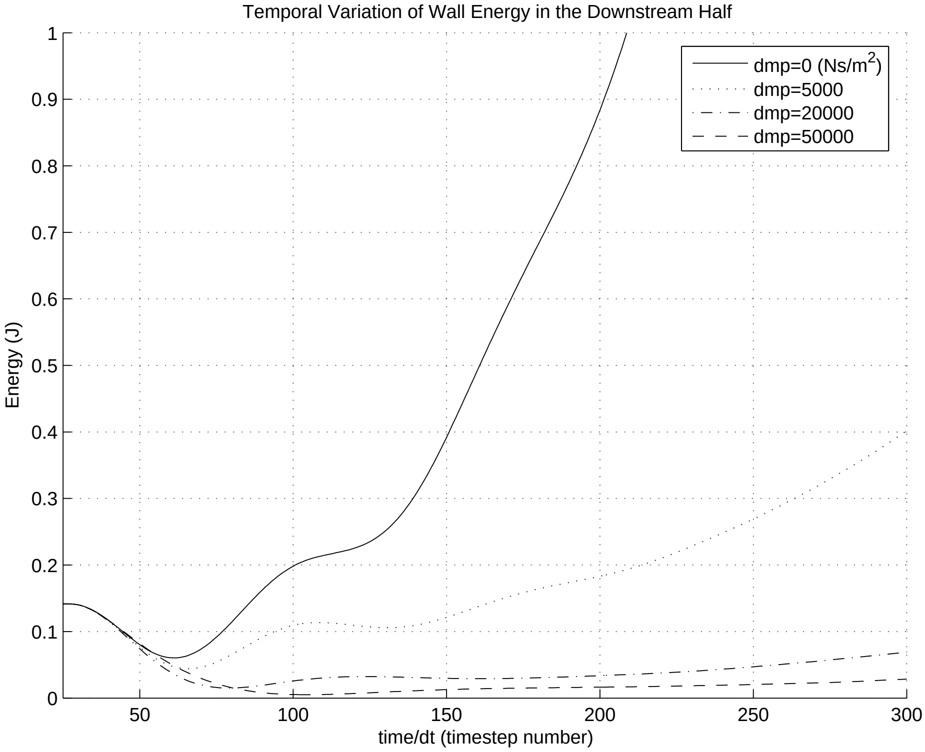

Figure 6.20: Wall energy variation with time for the downstream half of the compliant surface, where $dt = 1 \times 10^{-5}s$. The wall is released from its initial position at time $23dt$

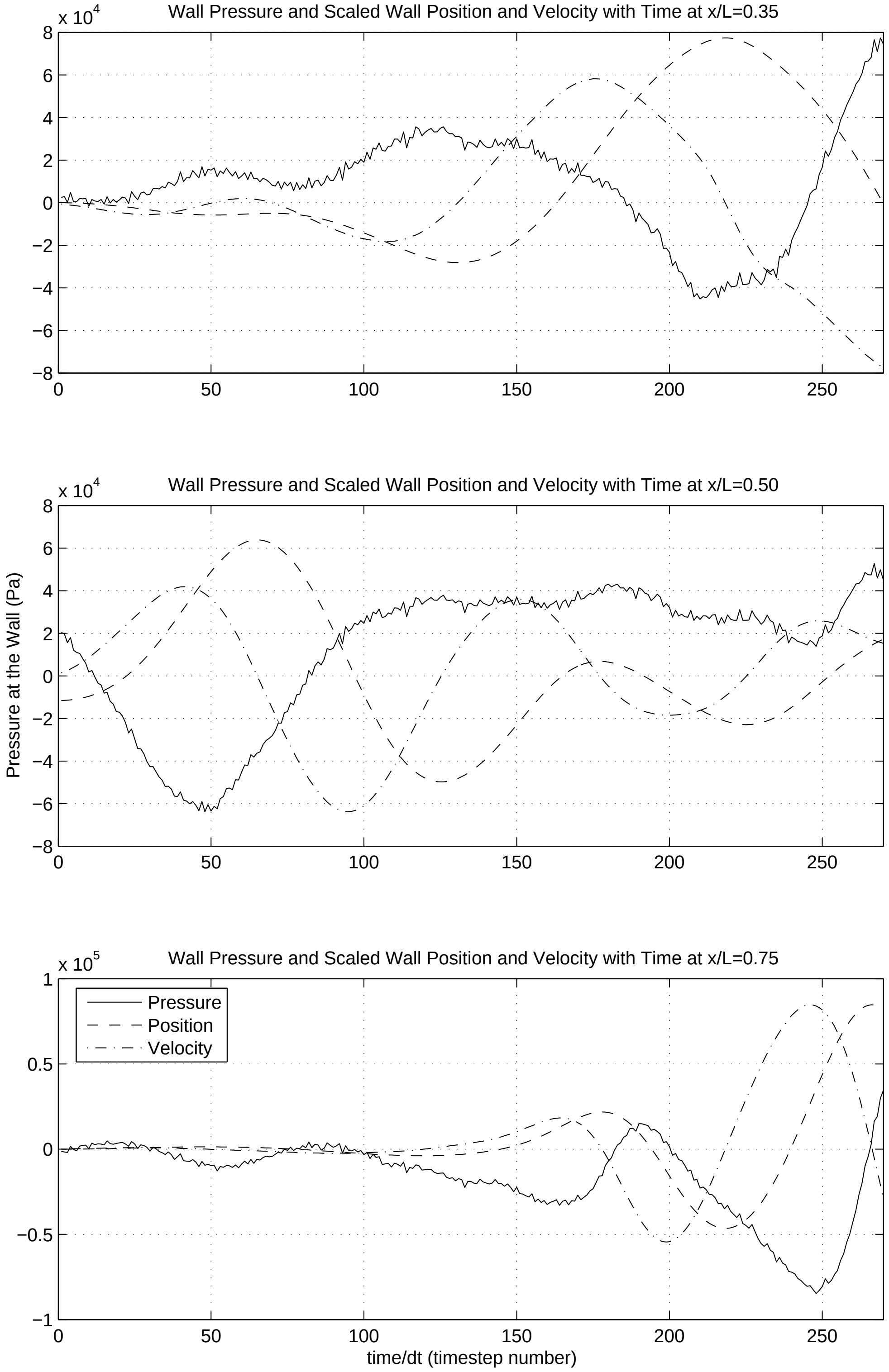

Figure 6.21: Wall pressure and wall position and velocity variation with time at three points along the compliant surface, for a compliant surface with *no structural damping.*

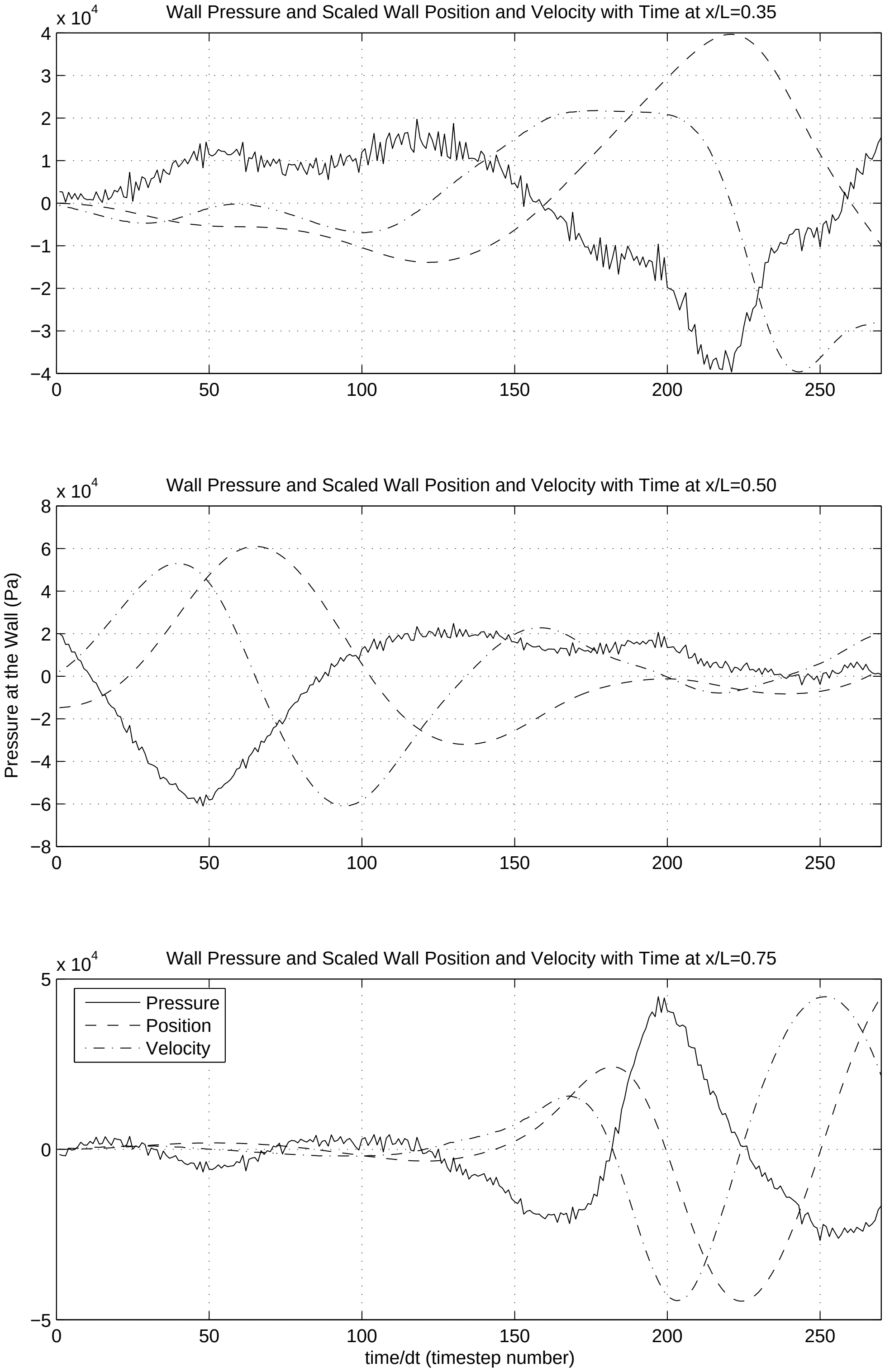

Figure 6.22: Wall pressure and wall position and velocity variation with time at three points along the compliant surface, for a compliant surface with structural damping $d = 5000 Ns/m^2$.

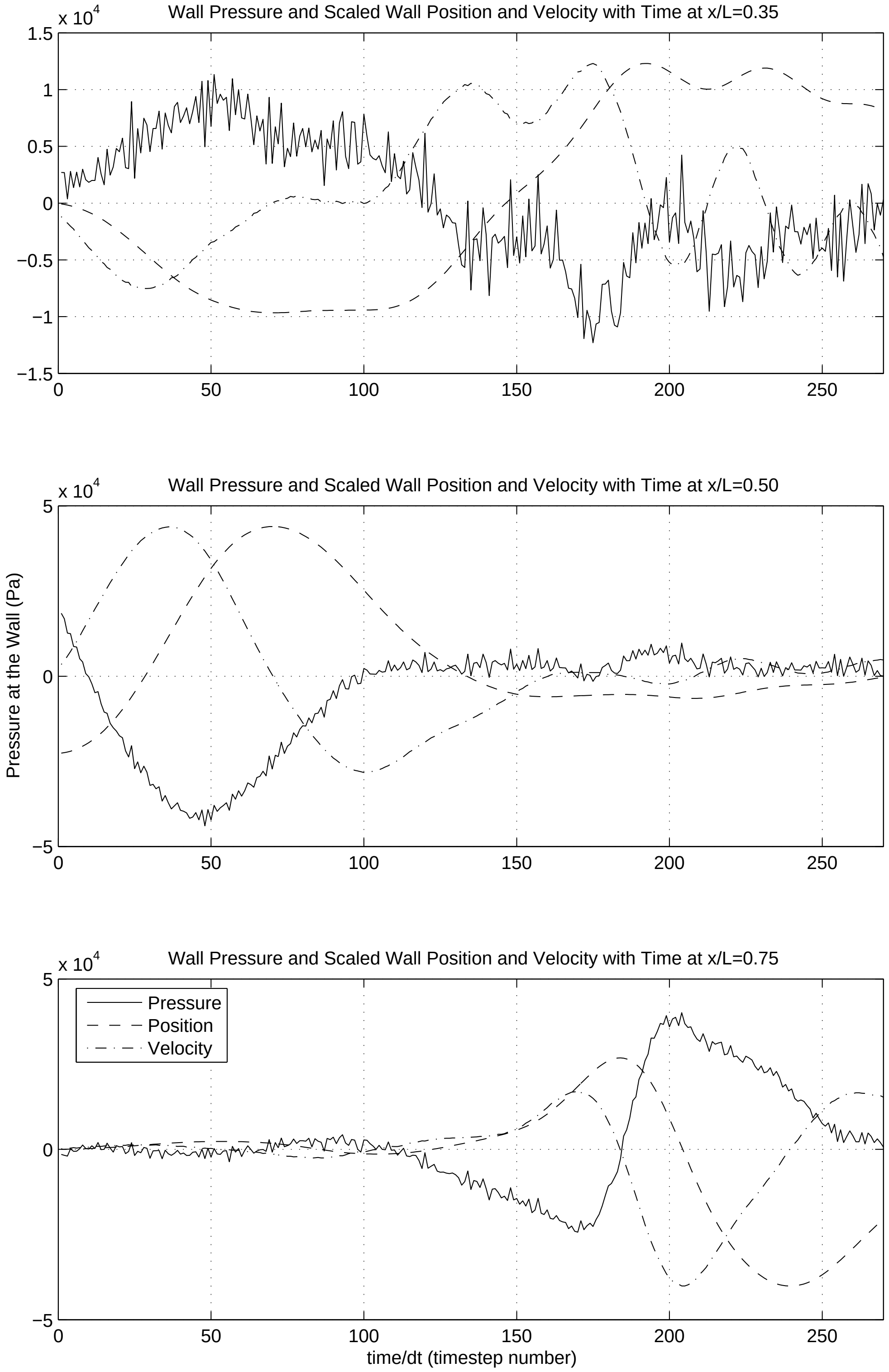

Figure 6.23: Wall pressure and wall position and velocity variation with time at three points along the compliant surface, for a compliant surface with structural damping $d = 20000 Ns/m^2$.

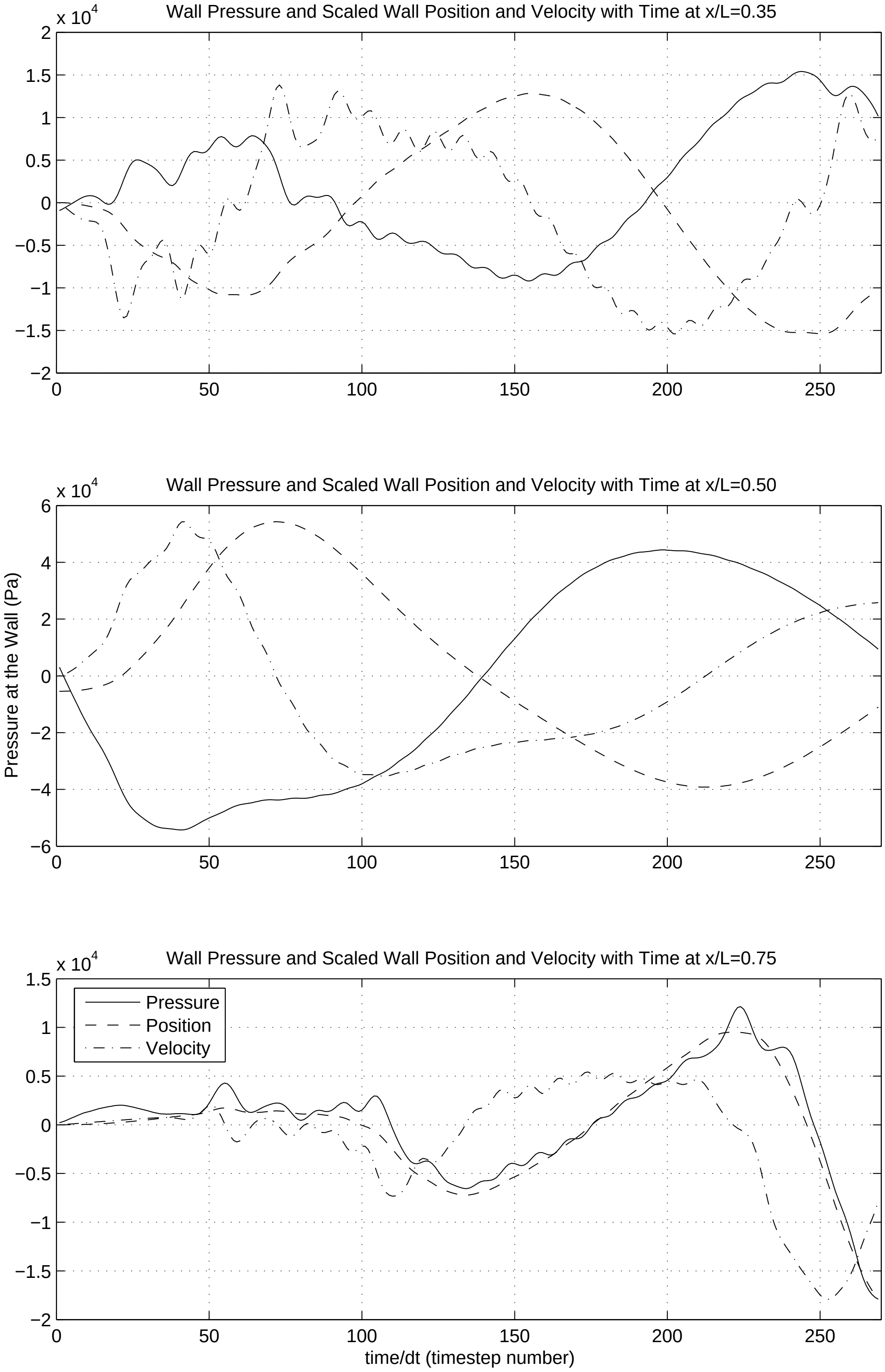

Wall Pressure and Scaled Wall Position and Velocity with Time at x/L=0.35

Wall Pressure and Scaled Wall Position and Velocity with Time at x/L=0.50

Wall Pressure and Scaled Wall Position and Velocity with Time at x/L=0.75

Figure 6.24: Wall pressure and wall position and velocity variation with time at three points along the compliant surface, for a compliant surface with *no structural damping* using the inviscid fluid model of Chapter 3.

Part IV

Conclusion

Chapter 7

Conclusions and recommendations for further work

7.1 Conclusions

Various computational techniques, involving boundary-element, finite-difference and discrete vortex modelling techniques have been adopted to perform a thorough investigation of finite compliant panels in a mean-flow.

7.1.1 The ideal flow model

For investigation of the wall-based instabilities at high Reynolds numbers a finite-difference wall solution was coupled to a potential flow solution of the flow through a boundary-element method technique similar to Lucey et al. [56]. Re-investigation of this method found that, in the linear regime of wall disturbances, eigenalaysis techniques could be applied directly to the numerical equations. This resulted in a new semi-numerical method for determining the eigenmodes and eigenvalues of the linear, finite flow-structure system.

Further investigation of the wall-based instabilities involved studying the development of transients from a linear disturbance through to long-term non-linear behaviour. This study revealed that the final steady-state non-linear response was independent of the starting conditions. A critical divergence wavelength would emerge from the starting disturbance and would quickly grow to involve the entire compliant panel and dictate the future development into a steady-state. Meanwhile, the non-critical wavelengths decayed. The final steady-state response consisted of sharp-peaked bumps along the length of the compliant panel. However, the streamwise spacing between these sharp-peaked bumps seemed to be somewhat random as the non-linear dynamics created complex wave-interactions when the peaks interfered with each other. Also, the existence of these sharp-peaked waves would likely not exist beyond some limit as viscous non-linear fluid mechanisms (such as separation over the bumps) would come into play.

The response of an unsupported flexible plate shows an interesting behaviour where a cross-over point exists between linear and non-linear wall responses. The results obtained through the linear eigenalysis of such a plate showed a strong agreement with the shapes that were observed through non-linear wall results of Lucey et al. [56]. This correlation was brought about by the fact that the linear fluid assumption still holds and the induced tension in the wall merely serves as a means to force the wall motion in a particular manner. These results indicate that even with a linear wall code, useful information regarding the shape of the wall motion and the rate of growth may be obtained, provided that the wavelength is sufficiently large to ensure that the linear fluid assumption still holds.

7.1.2 The DVM boundary layer model

The DVM boundary layer modelling technique presented in Chapter 5 is a novel application of the DVM to model FSI problems. It is the first method that links the DVM model to a compliant wall for efficient solution of the coupled system simultaneously. This coupling is made possible through the development of a novel BEM as well as a method for deriving the pressure and coupling that pressure to the wall equations. The BEM efficiently enforces the no-slip and no-flux conditions simultaneously while also handling the near-wall flow field solution. The pressure derivation calculates the forces on the moving surface with unsteady fluid loads and allows this forcing to be coupled to the structural equations for efficient simultaneous solution of the fluid-structure system.

The results from the novel DVM model presented in Chapter 6 show a qualitative agreement with the results of the inviscid model of Chapter 4. The DVM boundary layer model managed to resolve certain instabilities such as the TWF instability and also resolved a phase-change in between the pressure and wall displacement signals that could be expected for the system parameters that were modelled. These results provide validation that the DVM model is capable of achieving results for FSI systems and that these results are qualitatively accurate, resolving some expected system characteristics.

The results obtained using the boundary layer DVM were not intended to be an exhaustive investigation. The results did show that the DVM boundary layer model could be used to investigate DNS-type studies of FSI systems. The model yielded qualitatively accurate results in many aspects of the FSI system, including capturing TWF-type instabilities and enforcing boundary conditions. A mostly comparative analysis of the results from the preliminary modelling with the DVM yield some useful insights into the nature of the FSI system and potential considerations for the design of practical panels. However, a further exhaustive study of the validity and application of the model is required before firm conclusions can be drawn.

The results from the DVM indicated that both upstream and downstream travelling waves exist on the compliant surface when interacting with a boundary layer flow. The downstream waves are convectively unstable except in cases of heavy structural damping while the upstream waves are neutrally stable for the case of zero structural damping. The results also indicated that the shear stress decays gradually in the wake of the downstream-travelling wave. This creates an asymmetrical shear stress profile about a downstream-travelling wave front that tends to increase the drag on the compliant panel overall. These results have implications in the design of practical compliant panels for drag reduction.

It indicates that there is a trade-off between the benefits of adopting compliant panels for drag reduction through transition delay, and the increased drag due to the actual panels themselves. Due to the nature of the downstream-travelling instability, shorter finite-length panels would prevent the downstream-travelling TWF-type instability from amplifying excessively. These results indicate that for practical compliant coatings many short finite-length compliant panels spaced intermittently amongst a rigid body surface would be more beneficial than coating the entire body in a compliant coating. Also, the trade-off between the benefits of transition delay and the increased drag through the use of a compliant surface indicate that there is an optimal spacing between the finite panels which must be sought.

7.2 Recommendations for further work

Based on the work of this thesis, many possibilities for further studies into FSI system stability were identified. Most of these studies are based upon the possibilities open by the novel computational methods, and application of these methods, that are presented in this thesis.

7.2.1 Improving the DVM modelling

The DVM boundary-layer model that was developed in Chapter 5 requires further work to perform a thorough validation and application of the model to the study of FSI systems. There also exists great potential for the model to be further improved in the future. Specifically, the boundary element method that handles the near-wall flow solution as well as enforcement of the no-slip and no-flux condition could be improved in the future.

7.2.2 Boundary-layer eigenanalysis

Using the same techniques as those used to study the linear eigenmodes of the FSI system in this thesis one could study the linear eigenmodes of a fully viscous boundary layer coupled with a wall model. The work of Ehrenstein and Gallaire [26] has performed such analysis for boundary layer flows over statically deformed surfaces. The results from this thesis indicate the first instance where such an analysis technique has been used to extract the eigenvalues and eigenmodes from a finite-length compliant wall FSI system. Based on the success of these results there is no reason why this analysis could not be extended to include a deforming finite-length compliant boundary.

7.2.3 Three-dimensional effects

The work in this thesis focused exclusively on two-dimensional systems. However, throughout the development of the method, the possibility to expand the numerical method into three-dimensions was always kept in mind. As a result, future expansion of this method to study three-dimensional FSI systems should be relatively straightforward. The work of Khatir [43] has revealed the possibility for three-dimensional vortex blob methods in the study of boundary-layer instability. Meanwhile the investigation of wall-based instabilities using three-dimensional panel methods in potential flow is well established and has been visited by many researches such as Lucey and Carpenter [55], Pellicano et al. [62] and Paidoussis and Guo [60].

The possibility of extending the eigenalaysis into three-dimensions for potential flows remains a straightward possibility also. Galerkin techniques based upon these methods have already been investigated for a variety of FSI systems from cylindrical shells to flat-plates. However, the incorporation of the boundary-layer effects into these analysis (as discussed in the preceding section) remains a greater challenge. Currently, extraction of the eigenvalues for two-dimensional boundary layer models is done through specifying the governing fluid equations in streamfunction form as in the Orr-Sommerfeld equation. This makes specification, enforcement and satisfaction of the boundary conditions much simpler. However, in three-dimensions the streamfunction no longer becomes valid and alternate means must be found. This is not impossible as researchers such as Casalis [20] have achieved general solutions to the Orr-Sommerfeld type equations in three-dimensions. However, enforcement of the boundary conditions becomes more difficult.

References

[1] *Xfoil - Open Source Subsonic Airfoil Development System.* URL `http://web.mit.edu/drela/Public/web/xfoil/`.

[2] I H Abbott and A E Von Doenhoff. *Theory of Wing Sections.* Dover Publications Inc., New York, 1959.

[3] V V Aleksyev. The form of the loss of stability of a boundary layer on a flexible surface at high reynolds numbers. *J. Appl. Maths Mechs*, 66(5): 775–786, 2002.

[4] Yu. G. Aleyev. *Nekton.* The Hague: Junk, 1977.

[5] W T Ashurst. Numerical simulation of turbulent mixing layers via vortex dynamics. In *Symposium on Turbulent Shear Flows*, pages 403–413, 1977.

[6] V V Babenko. Experimental investigation of the boundary layer over rigid and elastic plates. *AGARD-R*, 1998.

[7] J Baglama, D Calvetti, and L Reichel. Iterative methods for the computation of a few eigenvalues of a large symmetric matrix. *BIT*, 36(3):400–440, 1996.

[8] A J Basu, R Narasimha, and A Prabhu. Modelling plane mixing layers using vortex points and sheets. *Appl. Math. Modelling*, 19:66–75, 1995.

[9] A J Basu, A Prabhu, and R Narasimha. Vortex sheet simulation of a plane “canonical” mixing layer. *Computers Fluids*, 21(1):1–30, 1992.

[10] R Beatson and L Greengard. A short course on fast multipole methods. $http : //math.nyu.edu/faculty/greengar/shortcourse_fmm.pdf$, Online, New York University.

[11] T B Benjamin. The threefold classification of unstable disturbances in flexible surfaces bounding inviscid flow. *Journal of Fluid Mechanics*, 16:436–450, 1963.

[12] G J Cafolla. *Hydroelastic Instabilities of Compliant Panels.* PhD thesis, Fluid Dynamics Research Group, 1997.

[13] P W Carpenter. Status of transition delay using compliant walls. *Progress in Astronautics and Aeronautics*, 123:79–113, 1990.

[14] P W Carpenter. Current status on the use of wall compliance for laminar-flow control. *Experimental Thermal and Fluid Science*, 16:133–140, 1998.

[15] P W Carpenter and C Davies. Numerical simulation of the evolution of tollmien-schlichting waves over finite compliant surfaces. *Journal of Fluid Mechanics*, 335:361–392, 1997.

[16] P W Carpenter, C Davies, and A D Lucey. Hydrodynamics and compliant walls: Does the dolphin have a secret? *Current Science*, 79(6):758–765, September 2000.

[17] P W Carpenter and A D Garrad. The hydrodynamic stability of flows over kramer-type compliant coatings. part 1. tollmien-schlichting instabilities. *Journal of Fluid Mechanics*, 155:465–510, 1985.

[18] P W Carpenter and A D Garrad. The hydrodynamic stability of flows over kramer-type compliant surfaces. part 2. flow-induced surface instabilities. *Journal of Fluid Mechanics*, 170:199–232, 1986.

[19] J Carrier, L Greengard, and V Rokhlin. A fast adaptive multipole algorithm for particle simulations. *SIAM J. Sci. and Stat. Comput.*, 9:669–686, 1988.

[20] G Casalis. Solution of the orr-sommerfeld equation for three dimensional incompressible flow using galerkin method and chebichev polynomials: The cocip code. *NASA STI/Recon Technical Report N*, 90:28021–+, nov 1989.

[21] A J Chorin. Numerical study of slightly viscous flow. *J. Fluid. Mech.*, 57 (4):785–796, 1973.

[22] H L Chung and D J Doorly. Velocity-vorticity formulation with vortex particle-in-cell method for incompressible viscous flow simulation, part ii : Application to vortex/wall interactions. *Numerical Heat Transfer*, 35(3): 277–294, 1999.

[23] A J Colley, P J Thomas, P W Carpenter, and A J Cooper. An experimental study of boundary-layer transition over a rotating, compliant disk. *Physics of Fluids*, 10:3340–3352, 1999.

[24] C I Draghicescu and M Draghicescu. A fast algorithm for vortex blob interactions. *Journal of Computational Physics*, 116:69–78, 1995.

[25] J Dugundji, E Dowell, and B Perkin. Subsonic flutter of panels on a continuous elastic foundation. *AIAA*, 1:1146–1154, 1963.

[26] U Ehrenstein and F Gallaire. On two-dimensional temporal modes in spatially evolving open flows: the flat-plate boundary layer. *J. Fluid Mech.*, Under Consideration, 2005.

[27] F E Fish and A H Clifford. Dolphin swimming - a review. *Mammal Rev.*, 21(4):181–195, 1991.

[28] M C Fisher, L M Weinstein, D M Bushnell, and R L Ash. Compliant-wall turbulent skin-friction-reduction research. *AIAA*, pages 75–833, 1975.

[29] M Gad-el Hak. Compliant coatings research: A guid to the experimentalist. *Journal of Fluids and Structures*, 1:55–70, 1987.

[30] M Gad-el Hak. Compliant coatings: A decade of progress. *Applied Mechanics Reviews*, 49(10):147–157, 1996.

[31] M Gad-el Hak. Compliant coatings: the simpler alternative. In *Proceedings EFTS*, 1998.

[32] M Gad-el Hak. Compliant coatings for drag reduction. *Progress in Aerospace Sciences*, 38:77–99, 2002.

[33] M Gaster. Is the dolphin a red herring? In *Proc. IUTAM Symp. on Turbulent Management and Relaminarization (Bangalore)*, pages 285–304. Springer, 1987.

[34] M Gharib, D Kremers, M M Koochesfahani, and Kemp M. Leonardo's vision of flow visualization. *Experiments in Fluids*, 33:219–223, 2002.

[35] J Gray. Studies in animal locomotion. vi. the propulsive powers of the dolphin. *J. Exo. Biol.*, 13:192–199, 1936.

[36] G Greengard. The core-spreading method approximates the wrong equation. *J. Comp. Phy.*, 61:345–348, 1985.

[37] L Greengard and V Rokhlin. A fast algorithm for particle simulations. *J. Comput. Phys.*, 73:325–348, 1987.

[38] L Greengard and J Strain. The fast gauss transform. *SIAM J. Sci. Stat. Comput.*, 12:79–94, 1991.

[39] P Huerre and P A Monkewitz. Local and global instabilities in spatially developing flows. *Annual Rev. Fluid Mech.*, 22:473–537, 1990.

[40] B L Hulme. Discrete galerkin and related one-step methods for ordinary differential equations. *Mathematics of Computation*, 26(120):881–891, 1972.

[41] O Inoue. Vortex simulation of a turbulent mixing layer. *AIAA Journal*, 23 (3):367–373, 1985.

[42] J Katz and A Plotkin. *Low Speed Aerodynamics: From Wing Theory to Panel Methods.* Number 0-07-050446-6. McGraw-Hill, 1991.

[43] Z Khatir. A boundary element method for the numerical investigation of near-wall fluid flow with vortex method simulation. *Engineering Analysis with Boundary Elements*, page In Press, 2004.

[44] Q Klinge, A D Lucey, and P W Carpenter. Compliant-wall technology: A review with emphasis on experimental work. Technical report, Warwick University FDRG, 1999.

[45] M O Kramer. Boundary-layer stabilization by distributed damping. *Journal of the Aeronautical Sciences*, 24:459, 1957.

[46] C Lanczos. An iteration method for the solution of the eigenvalue problem of linear differential and integral operators. *J. Research of the National Bureau of Standards*, 45(4):255–282, 1950.

[47] M T Landahl. On the stability of a laminar incompressible boundary layer over a flexible surface. *Journal of Fluid Mechanics*, 13:609–632, 1962.

[48] W J Layton. Galerkin methods for two-point boundary value problems for first order systems. *SIAM Journal on Numerical Analysis*, 20(1):161–171, 1983.

[49] R B Lehoucq and J A Scott. An evaluation of software for computing eigenvalues of sparse nonsymmetric matrices. *Preprint MCS-P547-1195, Argonne National Laboratory*, I11, 1996.

[50] R B Lehoucq, D C Sorensen, and C Yang. *ARPACK Users' Cuide: Solution of Large-Scale Eigenvalue Problems with Implicitly Restarted Arnoldi Methods*. SIAM, 1998.

[51] A Leonard. Vortex methods for flow simulation. *Journal of Comutational Physics*, 37(3):289–335, 1980.

[52] L Liu, F JI, J Fan, and K Cen. Recent development of vortex method in incompressible viscous bluff body flows. *J Zhejiang Univ SCI*, 6A(4):283–288, 2005.

[53] A D Lucey. *Hydroelastic Instability of Flexible Surfaces.* PhD thesis, Warwick University, 1989.

[54] A D Lucey. The excitation of waves on a flexible panel in a uniform flow. *Philosophical Transactions of the Royal Society of London (Series A)*, 356: 2999–3039, 1998.

[55] A D Lucey and P W Carpenter. A numerical simulation of the interaction of a compliant wall and inviscid flow. *Journal of Fluid Mechanics*, 234:121–146, 1992.

[56] A D Lucey, P W Carpenter, G J Cafolla, and M Yang. The nonlinear hydroelastic behaviour of flexible walls. *Journal of Fluids and Structures*, 11:717–744, 1997.

[57] A D Lucey and M W Pitman. 2006. a new method for determining the eigenmodes of finite flow-structure systems. paper no. pvp2006-icpvt11-93938. In *Proceedings of ASME-PVP 2006: 2006 ASME Pressure Vessels and Piping Division Conference*, July 23-27, 2006. CD-ROM (4 pages).

[58] M Marquillie and U Ehrenstein. On the onset of nonlinear oscillations in a separating boundary-layer flow. *Journal of Fluid Mechanics*, 490:169–188, 2003.

[59] I Newton. Philosophiae naturalis principia mathematica. Original, 1687.

[60] M P Paidoussis and C Q Guo. Analysis of hydroelastic instabilities of rectangular parallel-plate assemblies. *Journl of Pressure Vessel Technology*, 122: 502–508, 2000.

[61] C C Paige. *The computation of eigenvalues and eigenvectors of very large sparse matrices.* PhD thesis, University of London, London, England, 1971.

[62] F Pellicano, M Amabili, and M P Paidoussis. Nonlinear stability of circular cylindrical shells in annular and unbounded axial flow. *Journal of Applied Mechanics*, 68:827–834, 2001.

[63] M W Pitman and A D Lucey. 2006. a deterministic viscous vortex method with moving boundary conditions for fluid-structure interaction. In *Proc. International Conference on Computational Methods (ICCM)*, 15th-19th December, 2004. CD-ROM (4 pages).

[64] M W Pitman and A D Lucey. A deterministic viscous vortex method for grid-free cfd with moving boundary conditions. *IASME Transactions*, 1(4): 591–596, 2004.

[65] M W Pitman and A D Lucey. 2004. a deterministic viscous vortex method for grid-free cfd with moving boundary conditions. In *Proc. (CD) WAEAS/ IASME International Conference on Fluid Mechanics*, 17th-19th August, 2004, (Eds. M. Poulos, N. Mastorakis, V. Mladenov & R. Gorla). ISBN 968-8457-01-7. (6 pages).

[66] M W Pitman and A D Lucey. 2006. optimal swimming modes of a homosapien performing butterfly-stroke kicks. paper no. pvp2006-icpvt11-93939. In *Proceedings of ASME-PVP 2006: 2006 ASME Pressure Vessels and Piping Division Conference*, July 23-27, 2006. CD-ROM (4 pages).

[67] M W Pitman, A D Lucey, and P W Carpenter. 2004. computational modelling of the interaction of a flexible wall with boundary-layer flow. In *Proc. 8th International Conference on Flow-induced Vibration*, 6th-9th July, 2004, (Eds. E. De Langre & F. Axisa), Vol I, pp. 101-106.

[68] F W Puryear. Boundary-layer control drag reduction by compliant surfaces. Technical report, David W. Taylor Model Basin, 1962.

[69] H Ritter and J S Porteous. Water tunnel measurements of turbulent skin friction on a compliant coating. Technical report, Br. admir. Res. Lab, 1965.

[70] V Rokhlin. Rapid solution of integral equations of scattering theory in two dimensions. *J. Comput. Phys.*, 86:414–439, 1990.

[71] L Rosenhead. The formation of vorticies from a surface of discontinuity. *Proc. Royal Society*, 134:170–192, 1931.

[72] L F Rossi. Vortex computations of wall jet flows. In *Forum on Vortex Methods for Engineering Applications*, pages 127–145, 1995.

[73] L F Rossi. Resurrecting core spreading vortex methods: A new scheme that is both deterministic and convergent. *SIAM Journal on Scientific Computing*, 17:370–397, 1996.

[74] Y Saad. *Numerical Methods for Large Eigenvalue Problems.* Halsted Press, 1992.

[75] R L Smith and E F Blick. Skin friction of compliant surfaces with foamed material substrate. *Journal of Hydronautics*, 3:100–103, 1969.

[76] J Strain. Fast adaptive 2d vortex methods. *Journal of Computational Physics*, 132:108–122, 1997.

[77] F Sullivan and J Dongarra. Top ten algorithms of the century. *Computing in Science and Engineering*, 2(1):22–23, 2000.

[78] K Takeda, O R Tutty, and A D Fitt. A comparison of four viscous models for the discrete vortex method. *AIAA*, 1997.

[79] T Tsao, F Jiang, R Miller, T Yu-Chong, B Gupta, R Goodman, S Tung, and H Chih-Ming. An integrated mems system for turbulent boundary layer control. In *Proc. Int. Conf. on Solid-State Sensors and Actuators*, 1997.

[80] M R Visbal and R E Gordnier. Numerical simulation of the interaction of a transitional boundary layer with a 2-d flexible panel in the subsonic regime. *Journal of Fluids and Structures*, 19:881–903, 2004.

[81] Z Wang, K S Yeo, and B C Khoo. On two-dimensional linear waves in a blasius boundary layer over viscoelastic layers. *Eur. J. Mech. B-Fluids*, page Article in Press, 2005.

[82] Z Wang, K S Yeo, and B C Khoo. Spatial direct numerical simulation of transitional boundary layer over compliant surfaces. *Computers and Fluids*, 34:1062–1095, 2005.

[83] D S Weaver and T S Unny. The hydrodynamic stability of a flat plate. *Journal of Applied Mechanics*, 37:823–827, 1971.

[84] O Wiplier and U Ehrenstein. Numerical simulation of linear and nonlinear disturbance evolution in a boundary layer with compliant walls. *Journal of Fluids and Structures*, 14:157–182, 2000.

[85] O Wiplier and U Ehrenstein. On the absolute instability in a boundary-layer flow with compliant coatings. *Eur. J. Mech. B-Fluids*, 20:127–144, 2001.

Part V

Appendices

Appendix A

Description of Genetic Algorithm for Vortex Positioning

Genetic Algorithms are a stochastic, robust, multi-variable, non-linear optimisation techique. The method uses the concept of animal evolution and survival of the fittest to 'breed' solutions. Subsequent 'generations' of solutions are 'fitter' or more optimal solutions to the problem.

The general procedure used in the GA solution methodology is shown in Figure A.1. The optimisation methology consists of four main steps, these are: Initial Population Development, Scoring, Breeding and Mutation. These are explained in detail below.

As can be seen from Figure A.1, after the inital population development, the solution procdure enters a loop that is only broken when the convergence criteria is met. The core of this loop is the scoring, breeding and mutating of solution sets. Each loop is analogous to a *generation* of the population.

Initial Population Development

Figure A.1 shows that the first step in the optimisation by a genetic algorithm is the development of an initial population. The development of an initial population, using a two-variable optimisation problem as an example, is shown in Figure A.2.

It is important to note that GA's (or at least the simple GA used in this thesis) do not search for optimal solutions within an infinite domain. A 'search space' must be defined for each variable. This search space is then discretised into 'N' grid points.

Initially, possible solutions or *individuals* are distributed randomly throughout the 'search grid' by defining the position of an individual along a variables search grid as a binary string. The binary string defines which of the nodes along a variables 'search grid' the individual belongs to. Knowing the upper and lower limits of the search space and the number of nodes, this can directly relate to a varirable value. Therefore, the accuracy of the GA may be increased by increasing the number of bits in the binary string because the number of bits in the binary string is directly proportional to the number of nodes. The problem of randomly distributing the inital individuals becomes a simple matter of randomly placing 1 or 0 bits within the binary strings.

To generate an individual 'chromosome', the binary strings for each variable of an individual solution are combined into a single binary string. This binary 'chromosome' contains all of the information relating to one possible solution. The length and position of the binary string that relates to each variable must be recorded for later extraction of the variable strings, and hence the optimal variable values.

This process is repeated to create an initial random population of 'M' individual chromosomes. After the creation of the initial population, the individuals are ready for the next step which involves assigning a score to each individual.

Scoring

After generation of an initial population, or any new population 'generation', the individuals must be 'scored'. Scoring involves using a scoring function to assign a result to each individual. Generally, the scoring function is attempting to be minimised. Therefore, if there are multiple optimisation objectives, the score assigned to each objective must be weighted and made directly (or inversely) proportional to the final score value depending upon the objective definition.

A diagrammatic representation of the scoring of the individuals of a population is shown in Figure A.3 and relates to the two-variable problem presented in Figure A.2. In this problem, where one is trying to locate the global maximum, the value obtained from the funtion (graph) must be *inversely* proportional to the final score, so that the global maximum has the minimum score value.

Breeding

The 'breeding' of individual solutions to create a new 'generation' of solution is the stage that mostly influences the accuracy and efficiency of the GA. There are many different ways to select individuals for breeding and also many ways to perform the binary crossover that mixes the bits of the parent chomosomes to create new offspring. In this thesis, a weighted 'roulette wheel' method was used for selecting the parents. While simple bit-swapping was used for the binary crossover.

Mutation

The final step within a generation of the GA is to perform a random mutation on the newly-created children. Mutation ensures that a particular individual does not dominate the gene-pool and cause a convergence toward a local solution. Mutation is performed by assigning a probability (known as the mutation rate) that each individual binary bit in the whole gene pool will be swapped from a '1' to a '0', or vice versa. Typically this probability is low. Higher mutation rates will mean improved searching of the solution space for the optimal solution, however slower convergence rates. Lower mutation rates give faster convergence but less thorough searching of the solution space for global optimals.

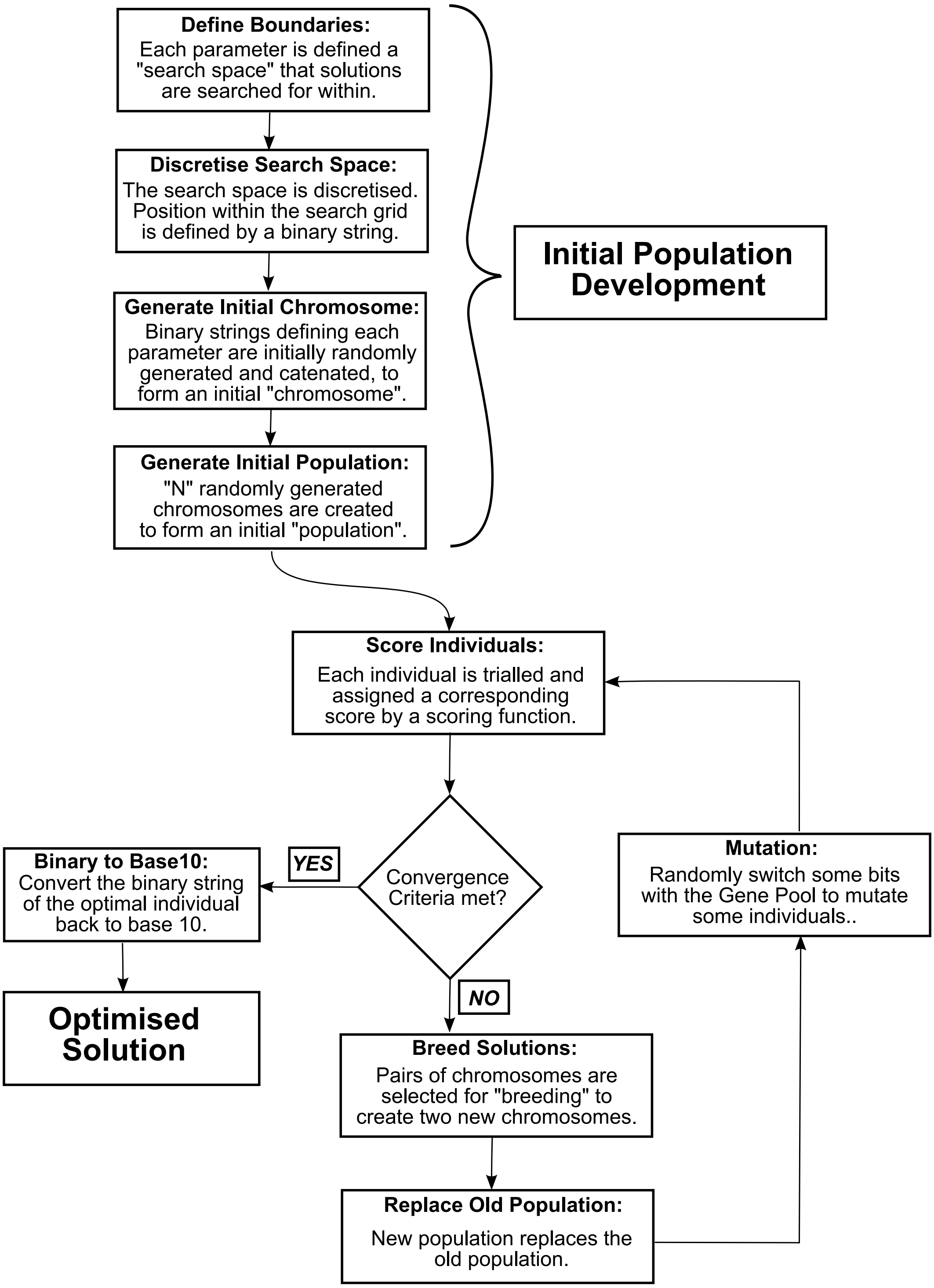

Figure A.1: Genetic Algorithm Solution Methodology

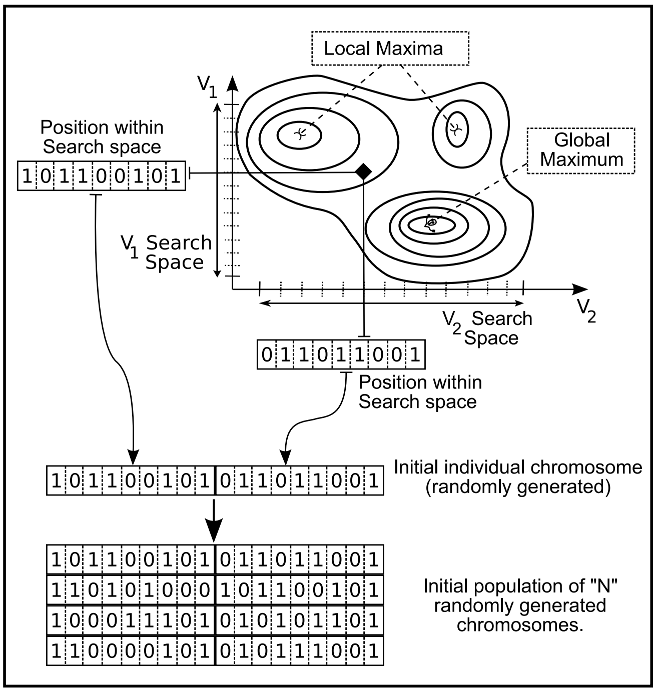

Figure A.2: Diagramatic representation of Initial Population Development using a two-variable optimisation problem as an example

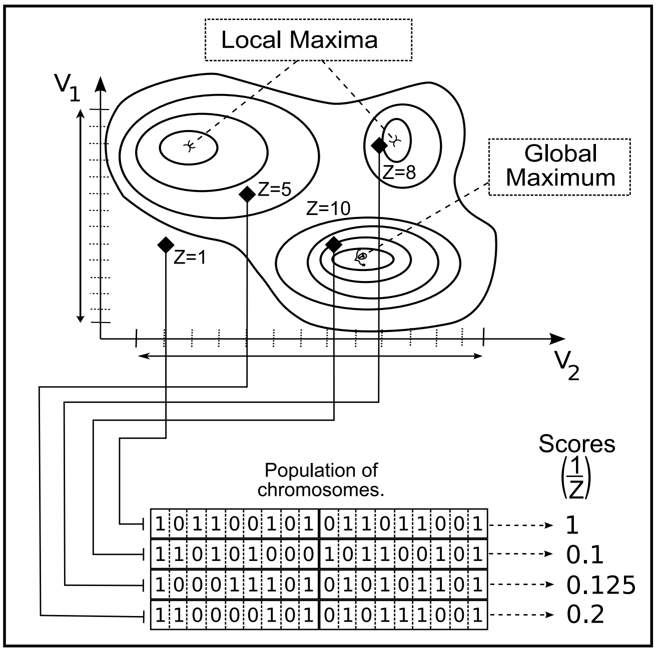

Figure A.3: Diagramatic representation scoring of individuals in a population. Using a two-variable optimisation problem as an example.

Appendix B

Reduction of Second Order Linear Systems

In this thesis, the ideal flow model based on the model of Lucey et al. [56], results in a system of coupled second order linear equations. In order for these equations to be efficiently solved by a compuational eigenvalue solver (specifically the MATLAB "eigs" function based on the ARPACK FORTRAN routines) these second order equations must be reduced to a system of first order equations.

The second order system can be considered to take the general form

$$M\ddot{z}(t) + D\dot{z}(t) + Kz(t) = 0 \tag{B.1}$$

then the system may be reduced to the first order system as

$$\begin{bmatrix} I & 0 \\ 0 & M \end{bmatrix} \begin{Bmatrix} \dot{z}(t) \\ \ddot{z}(t) \end{Bmatrix} = \begin{bmatrix} 0 & I \\ -K & -D \end{bmatrix} \begin{Bmatrix} z(t) \\ \dot{z}(t) \end{Bmatrix} \tag{B.2}$$

which takes the form

$$[E]\,\dot{x} = [A]\,x \tag{B.3}$$

A useful note is that if the matrix $[M]$ is the identity matrix then the equation simply becomes

$$\dot{x} = [A]\,x \tag{B.4}$$

Appendix C

An Overview of Galerkin Methods

The Galerkin Method is a special form of the weighted residuals method, where the weighting function is selected from the basis functions. A review of the Galerkin method and its application to solving linear differential equations is given in Layton [48], Hulme [40]. This section gives a brief review of the weighted residuals method. Then the special weighted residual method known as Galerkin's method is discussed. Finally, the application of Galerkin's method to a homogeneous, linear second order differental equation is considered.

The Weighted Residuals Method

We start with the differential equation

$$L[y(x)] + f(x) = 0 \qquad a \leq x \leq b \tag{C.1}$$

where $L[y(x)]$ is a linear differential operator. It is proposed that if

$$\int_a^b w(x) f(x)\, dx = 0 \tag{C.2}$$

for any arbitrary function $w(x)$, then $f(x) \equiv 0$. The residual of Equation C.1 is defined as

$$r(x) = L[u(x)] + f(x) \tag{C.3}$$

and a trial solution for $y(x)$ is introduced that takes the form

$$u(x) = \varphi_0(x) + \sum_{j=1}^{n} C_j \varphi_j(x) \tag{C.4}$$

The goal is to construct the solution $u(x)$ so that the integral of the residual will be zero for some choices of weighting function. Therefore,

$$\int_a^b w(x) r(x)\, dx = 0 \tag{C.5}$$

The Galerkin Method

The Galerkin method is one of the most important weighted residual methods. It was invented by the Russian mathematician Boris Grigoryevich Galerkin. Galerkin's method selects the weighting functions $w(x)$ from the basis functions. Therefore, by Galerkin's method, it is required that the following N eqations hold true

$$\int_a^b \varphi_i(x) \left(L[\sum_{j=1}^{n} C_j \varphi_j(x)] + L[\varphi_0(x)] + f(x) \right) dx = 0 \qquad for\, i = 1, 2, 3 ... n \tag{C.6}$$

Application of Galerkins Method

Here we consider the application of the Galerkin's method of weighted residuals to solve the homogeneous, linear second order differential equation. This type of equation characterises many systems, particularly the flow of an inviscid fluid over a compliant coating as investigated in this thesis. The equations to be solved are a system of n coupled differential equations given as

$$[A]\{\ddot{z}\} + [B]\{\dot{z}\} + [C]\{z\} = 0 \tag{C.7}$$

where $[A]$,$[B]$ and $[C]$ are $n \times n$ coefficient matrices and $z = f(x,t)$. For this problem, a trial solution will be constructed of the form

$$u(x,t) = \left[\sum_{j=1}^{n} C_j \varphi_j(x) \right] e^{st} \tag{C.8}$$

where φ_i can be selected from any orthogonal set of basis functions. The actual form of the besis function is irrelevant, however typically for the fluid-structure interaction problems like those encountered in this thesis, φ_i is chosen as the set of *in-vacuo* eigenmodes (solutions to the beam equation). In this specific case

$$\varphi_i = sin\left(\frac{i\pi}{L_w} x \right) \qquad for\, i = 1, 2, 3 ... n \tag{C.9}$$

where L_w is the length of the finite compliant wall section and n is the maximum number of in-vacuo modes to construct the solution with. The selection of n is arbitrary and will define the accuracy of the solution in a similar way to the number of terms selected in a Taylor series expansion. For substitution into Equation C.7, Equation C.8 can be written in matrix form as

$$u(x,t) = \left[[\varphi_j]\{C_j\} \right] e^{st} \tag{C.10}$$

substitution of this discretised trial solution into Equation C.7 gives the residual function

$$r(x,t) = s^2[A][\varphi_j]\{C_j\}e^{st} + s[B][\varphi_j]\{C_j\}e^{st} + [C][\varphi_j]\{C_j\}e^{st} \tag{C.11}$$

Therefore, in matrix form, the inner product of the residual with the trial function will result in n equations which can be written in matrix form as

$$\int_0^{L_w} \varphi_i(x) r(x)\, dx = s^2[D_{i,j}]C_j e^{st} + s[E_{i,j}]C_j e^{st} + [F_{i,j}]C_j e^{st} = 0 \tag{C.12}$$

where the elements in the rows (i) and columns (j) of matrices $[D]$,$[E]$ and $[F]$ are

$$D_{i,j} = \sum \left(\{\varphi_i\} \cdot \{[A]\{\varphi_j\}\} \right) \, dx \tag{C.13}$$

$$E_{i,j} = \sum \left(\{\varphi_i\} \cdot \{[B]\{\varphi_j\}\} \right) \, dx \tag{C.14}$$

$$F_{i,j} = \sum \left(\{\varphi_i\} \cdot \{[C]\{\varphi_j\}\} \right) \, dx \tag{C.15}$$

where $i = j = 1, 2, 3...n$.

Equation C.12 may be solved by reduction to a first order linear DE using the method presented in Appendix B and solution of the resulting eigenvalue problem for the eigenvalues s and the corresponding eigenvectors $\{C_j\}$.